

**Titre:** Validation of an Isotope Evolution Model for Apollo3 Calculations in  
Title: SFR Core

**Auteur:** Aaron Greganti  
Author:

**Date:** 2017

**Type:** Mémoire ou thèse / Dissertation or Thesis

**Référence:** Greganti, A. (2017). Validation of an Isotope Evolution Model for Apollo3  
Calculations in SFR Core [Mémoire de maîtrise, École Polytechnique de Montréal].  
Citation: PolyPublie. <https://publications.polymtl.ca/2484/>

 **Document en libre accès dans PolyPublie**  
Open Access document in PolyPublie

**URL de PolyPublie:** <https://publications.polymtl.ca/2484/>  
PolyPublie URL:

**Directeurs de  
recherche:** Alain Hébert, & Jean-François Vidal  
Advisors:

**Programme:** Génie mécanique  
Program:

UNIVERSITÉ DE MONTRÉAL

VALIDATION OF AN ISOTOPE EVOLUTION MODEL FOR APOLLO3  
CALCULATIONS IN SFR CORE

AARON GREGANTI  
DÉPARTEMENT DE GÉNIE MÉCANIQUE  
ÉCOLE POLYTECHNIQUE DE MONTRÉAL

MÉMOIRE PRÉSENTÉ EN VUE DE L'OBTENTION  
DU DIPLÔME DE MAÎTRISE ÈS SCIENCES APPLIQUÉES  
(GÉNIE MÉCANIQUE)  
MARS 2017

UNIVERSITÉ DE MONTRÉAL

ÉCOLE POLYTECHNIQUE DE MONTRÉAL

Ce mémoire intitulé :

VALIDATION OF AN ISOTOPE EVOLUTION MODEL FOR APOLLO3  
CALCULATIONS IN SFR CORE

présenté par : GREGANTI Aaron

en vue de l'obtention du diplôme de: Maîtrise ès sciences appliquées

a été dûment accepté par le jury d'examen constitué de:

M. MARLEAU Guy, Ph. D., président

M. HÉBERT Alain, Doctorat, membre et directeur de recherche

M. VIDAL Jean-François, Ph. D., membre et codirecteur de recherche

M. CHAMBON Richard, Ph. D., membre

**DEDICATION**

*To my family and to my friends*

## ACKNOWLEDGEMENTS

First of all, I would like to thank my professor and research director Alain Hébert for accepting me among his students. He has relentlessly listened to all the questions I posed to him and patiently answered them. Thanks to him, I had the opportunity to do an internship at the “Commissariat à l’énergie atomique et aux énergies alternatives” (CEA) in Cadarache. In the “Laboratoire d’Études Physiques” (LEPh), now under the direction of Cyrille de Saint-Jean, I spent six months in a friendly and stimulating atmosphere.

I am particularly grateful to my tutor Jean-François Vidal. He greatly supported and helped me, demonstrating patience and dedication. And he was not the only one: my heartfelt thanks to Gérard Rimpault, Pascal Archier, Vincent Pascal, Jean-Marc Palau, Jean Tommasi et Yiannick Penelieu. I would like to thank also the developers of the “Service d’Études des Réacteurs et de Mathématiques Appliquées” (SERMA) and especially Didier Schneider, Fabien Auffret, Pierre Bellier et Simone Santandrea for their aid.

Within the center, I would also like to thank all the PhD students and interns whom I spent unforgettable moments with, together with the “Italians” I spent the lunch with every Tuesday.

Concerning Politecnico di Milano, I can’t help thanking Marco Beghi and Enrico Padovani, the professors who mostly helped me with this French-Canadian experience.

An experience I had the chance to share with Pietro, and where I met remarkable people: “les deux Clément“, Atyab et Camilla are the ones I want to thank the most.

But I don’t have to ignore all those voices, the most solid ones, which led me during these two years: the voices of those who have always believed in me, yesterday and today. I heartily thank all my family for the endless support, my high school friends, my colleagues in Milan, Impry, Monica, Balbe e Marco. C’est grâce à tous!

## RÉSUMÉ

Dans le cadre du développement du code déterministe multi-filières APOLLO3, il est nécessaire de mettre au point et valider les nouveaux schémas de calcul permettant d'améliorer la prédiction des grandeurs neutroniques d'intérêt. Les études neutroniques du cœur CFV du futur prototype ASTRID (RNR refroidi au sodium) demandent notamment un calcul précis des concentrations isotopiques tout au long de son évolution sous irradiation.

Le schéma ECCO/ERANOS utilisé actuellement pour les calculs des cœurs de RNR est constitué des deux étapes classiques réseau et cœur. Les sections efficaces microscopiques autoprotégées et condensées à 33 groupes sont déterminées une seule fois en début de vie à partir de calculs 2D ECCO de cellules ou assemblages en réseau infini (avec une concentration infinitésimale pour les noyaux lourds et les produits de fission non présents en début de vie). Elles sont ensuite utilisées dans une modélisation 3D ERANOS pour réaliser les calculs du cœur complet en évolution microscopique. Ce schéma fait l'hypothèse que les sections efficaces microscopiques n'évoluent pas avec l'irradiation et la modification de composition des différents milieux fissiles.

La mise en place de nouveaux schémas de calcul avec le code multi-filières APOLLO3 est l'occasion de revenir sur cette hypothèse puisque d'autres possibilités utilisées jusqu'à présent dans les schémas APOLLO2/CRONOS2 des REL sont dorénavant disponibles. Elles reposent sur un paramétrage des sections efficaces autoprotégées, macroscopiques comme microscopiques, en fonction du taux de combustion, obtenues en faisant évoluer les motifs 2D élémentaires cellules ou assemblages. Ces sections sont stockées dans des bibliothèques dites "évoluantes" permettant une interpolation à l'étape cœur. L'évolution cœur peut alors être menée de 2 façons :

- macroscopique : le code cœur extrapole les taux de combustion locaux pour chaque pas d'évolution et récupère, via une interpolation linéaire, les sections efficaces macroscopiques de la bibliothèque évolutive pour calculer le pas suivant.
- microscopique : le code cœur résout les équations d'évolution isotopiques en temps (équations de Bateman) suivant des stratégies plus ou moins précises (simple extrapolation ou méthodes de type prédicteur-correcteur) en interpolant les sections efficaces microscopiques en fonction du taux de combustion local. Cette méthode est a priori plus précise que la méthode ECCO/ERANOS puisqu'elle prend en compte les modifications

de l'autoprotection et du spectre avec l'évolution.

L'objectif de ce travail est de valider l'hypothèse "temps 0", c'est à dire que les sections efficaces ne changent pas sous irradiation. Pour faire ça, trois géométries 2D seront étudiées: une cellule, un cluster fissile-fertile et une tranche de coeur. Pour ces géométries, il sera montré que l'hypothèse "temps 0" introduit une différence de réactivité liée au changement du spectre du flux avec lequel les sections efficaces microscopiques sont condensées. Cette différence, par contre, est faible et elle peut être éliminée en utilisant un modèle microscopique avec bibliothèques "évoluant" dont le paramétrage est composé par seulement deux points de tabulation en burn-up: le point initial et le point final. Ce modèle permettra d'avoir la précision envisagée en doublant seulement le temps de calculs côté réseau et la mémoire requise pour le stockage des sections efficaces. Pour le cas cellule, les calculs d'évolution côté réseau seront validés par rapport à des calculs Monte Carlo faits avec TRIPOLI4 évoluant et à des calculs ECCO/ERANOS.

## ABSTRACT

In the frame of the development of the new multi-purpose deterministic code APOLLO3, it is necessary to develop and validate the new calculation schemes capable of improving the prediction of the neutronic quantities of interest. The neutronic studies on the CFV core of the new prototype ASTRID (sodium cooled FNR) notably demand an accurate calculation of the isotopic concentrations during its evolution under irradiation.

The ECCO/ERANOS scheme, currently used for FNR core calculations, is constituted by the two classic steps: lattice and core. Microscopic cross sections, self-shielded and condensed into 33 energy groups, are determined only one time at the beginning of life from 2D ECCO cell or assembly calculations in infinite lattice (with an infinitesimal concentration of heavy nuclei and fission products not initially present). They are, then, used for 3D ERANOS modelization of the whole core in micro-depletion. This scheme makes the hypothesis that microscopic cross sections do not evolve during the irradiation and the composition change of the different fissile materials.

The development of the new APOLLO3 calculation schemes is an opportunity to re-discuss this hypothesis, because other possibilities, currently used in PWR APOLLO2/CRONOS2 calculation schemes, are available. They lie on the parametrization of self-shielded cross sections, both macroscopic and microscopic, as a function of the burn-up. These cross sections are obtained performing 2D cell or assembly depletion calculations. They are, then, stored in “evolving” libraries which allow their interpolation at core step. Core depletion can be performed in two ways:

- macroscopic: the core code extrapolates the local burn-up for each evolution step and interpolate the macroscopic cross sections from the “evolving” library in order to evaluate the following time step.
- microscopic: the core code solves the Bateman equations with a more or less accurate strategy (simple extrapolation or predictor-corrector methods), interpolating the microscopic cross sections as a function of the local burnup. This model is, a priori, more accurate than the ECCO/ERANOS one, because it takes into account self-shielding and spectrum changes during the evolution.



The aim of this work is the validation of the “time 0” hypothesis, i.e. that cross sections do not change under irradiation. To do so, 3 different 2D geometries will be studied: a cell, a fissile-fertile cluster and a core plane. For these geometries, it will be shown that the “time 0” hypothesis introduces a reactivity difference due to a change in the flux spectrum the microscopic cross sections are condensed with. This difference, nevertheless, is small and it can be eliminated using a microscopic model with “evolving” libraries whose parametrization is composed by only two burn-up tabulation points: the initial point and the final one. This model reaches the required accuracy only by doubling the calculation time at lattice step and the memory storage for the libraries. For the cell case, lattice depletion calculations will be validated with respect to Monte Carlo evolving TRIPOLI4 calculations and ECCO/ERANOS ones.

## TABLE OF CONTENTS

DEDICATION . . . . .	III
ACKNOWLEDGEMENTS . . . . .	IV
RÉSUMÉ . . . . .	V
ABSTRACT . . . . .	VII
TABLE OF CONTENTS . . . . .	IX
LIST OF TABLES . . . . .	XII
LIST OF FIGURES . . . . .	XIII
LIST OF SYMBOLS AND ABBREVIATIONS . . . . .	XVII
LIST OF APPENDICES . . . . .	XVIII
CHAPTER 1 INTRODUCTION . . . . .	1
1.1 Generation IV: Challenges and Solutions of the Nuclear Industry . . . . .	1
1.2 FNR: Fast Nuclear Reactor . . . . .	2
1.3 SFR: Sodium-cooled Fast Reactor . . . . .	4
1.4 ASTRID: Advanced Sodium Technological Reactor for Industrial Demonstration . . . . .	6
1.5 CFV: Coeur à Faible Vidange . . . . .	7
1.6 APOLLO3: A new code for new challenges . . . . .	8
1.6.1 Nuclear Code Scenario . . . . .	8
1.6.2 APOLLO3: General Objectives . . . . .	10
1.6.3 APOLLO3: A Core Physics Simulation Tool for ASTRID CFV . . . . .	11
1.7 Objective of the Thesis . . . . .	12
1.8 Contents of the Thesis . . . . .	13
CHAPTER 2 LITERATURE REVIEW . . . . .	14
2.1 The Transport Equation . . . . .	14
2.2 Cross Sections . . . . .	16
2.3 Depletion Calculation . . . . .	20
2.4 Solution of the Boltzmann Equation . . . . .	22

2.4.1	Different Forms of the Transport Equation . . . . .	22
2.4.2	Source Density . . . . .	23
2.4.3	Multigroup Approach . . . . .	26
2.4.4	Self-Shielding . . . . .	28
2.4.5	General Resolution Algorithm . . . . .	32
2.4.6	TDT Solver . . . . .	34
2.4.7	MINARET Solver . . . . .	38
2.4.8	Homogenization and Condensation . . . . .	40
2.4.9	Leakage Model . . . . .	41
2.4.10	Stochastic approach and Monte Carlo method . . . . .	41
2.5	Solution of the Bateman Equations . . . . .	43
2.5.1	Flux Normalization . . . . .	44
2.5.2	Depletion Chain . . . . .	45
2.5.3	ERANOS depletion solver . . . . .	47
2.5.4	MENDEL depletion solver . . . . .	47
2.5.5	Treatment of statistical uncertainties in Monte Carlo burn-up codes .	50
CHAPTER 3	EVOLUTION OF A CFV CELL GEOMETRY . . . . .	52
3.1	Lattice Depletion . . . . .	52
3.1.1	Preliminary Studies . . . . .	53
3.1.2	Inter-Code Validation . . . . .	58
3.1.3	Reactivity Analysis . . . . .	67
3.2	Core Depletion . . . . .	73
3.2.1	Preliminary Studies . . . . .	74
3.2.2	Validation: No Leakage Model . . . . .	79
3.2.3	Validation: Leakage Model . . . . .	87
3.3	Burn-up parametrization of the cross section libraries . . . . .	92
3.4	Conclusions . . . . .	93
CHAPTER 4	EVOLUTION OF A FISSILE-FERTILE CLUSTER GEOMETRY . .	95
4.1	Lattice Depletion . . . . .	96
4.1.1	Reference Evolution Geometry . . . . .	96
4.1.2	Reactivity Decomposition . . . . .	101
4.1.3	Simplified Evolution Geometry . . . . .	103
4.2	Core Depletion . . . . .	103
4.2.1	Comparison of the Depletion Models . . . . .	105
4.2.2	Burn-up parametrization of the cross section libraries . . . . .	113

4.3	Conclusions . . . . .	114
CHAPTER 5 EVOLUTION OF A 2D CORE PLANE GEOMETRY . . . . .		115
5.1	Geometry . . . . .	115
5.2	Cross Sections . . . . .	117
5.3	Results: 6 Materials . . . . .	118
5.3.1	Burn-up parametrization of the cross section libraries . . . . .	122
5.4	Results: 4 Materials . . . . .	123
5.5	Conclusions . . . . .	125
CHAPTER 6 CONCLUSION . . . . .		126
REFERENCES . . . . .		128
APPENDICES . . . . .		133

# LIST OF TABLES

Table 1.1	Characteristics of the six Generation IV nuclear reactor systems . . .	2
Table 2.1	Energy Boundaries of fission spectrum macro-groups . . . . .	27
Table 3.1	Inter-code validation: Time 0 . . . . .	62
Table 3.2	Inter-code validation: Time 0 (in pcm, reaction rates normalized to $10^5$ neutron production) . . . . .	64
Table 3.3	Inter-code validation: Time 1440 (in pcm, reaction rates normalized to $10^5$ neutron production) . . . . .	65
Table 3.4	Inter-code validation: Time 1440 . . . . .	66
Table 3.5	List of all Fission Products by order of contribution to anti-reactivity $\Delta\rho_{FP}$ . . . . .	72
Table 3.6	Fission Proportions: Time 0 . . . . .	76
Table 3.7	Fission Proportions: Time 1440 . . . . .	78
Table 3.8	Heterogeneous case: Absorption rate comparison at 1440 days . . . .	85
Table 3.9	Homogeneous case: Absorption rate comparison at 1440 days . . . .	86
Table 3.10	Leakage case: Absorption rate comparison at 1440 days . . . . .	91
Table 4.1	Reactivity loss decomposition at 1440 days . . . . .	101
Table 4.2	Fissile-Fertile Cluster: Time 0 Absorption Comparison: homogeneous MINARET at 33 groups/ heterogeneous reference TDT-MOC (in pcm)	105
Table 4.3	Fissile-Fertile Cluster: Time 1440 Absorption Comparison: homogeneous MINARET at 33 groups/ heterogeneous reference TDT-MOC (in pcm) . . . . .	106
Table 4.4	Fissile-Fertile Cluster: Absorption rate comparison at 1440 days . . .	112
Table 5.1	6 Materials: Comparisons of isotope concentrations and flux at 1440 days . . . . .	121
Table 5.2	4 Materials: Comparisons of isotope concentrations and flux at 1440 days . . . . .	124
Table A.1	Relative differences in integrated flux distribution at time zero . . . .	133
Table A.2	Relative differences in flux distribution in the energy group 1.2-2 keV at time zero . . . . .	134

# LIST OF FIGURES

Figure 1.1	SFR scheme . . . . .	5
Figure 1.2	Overall schedule of the ASTRID project . . . . .	7
Figure 1.3	CFV core layout . . . . .	9
Figure 1.4	CFV core geometry . . . . .	9
Figure 2.1	Capture (n, $\gamma$ ) and Fission (n,fission) U238 cross sections . . . . .	18
Figure 2.2	Input Cross section library creation scheme . . . . .	18
Figure 2.3	Doppler-Broadening Effect . . . . .	19
Figure 2.4	Depletion calculation scheme . . . . .	21
Figure 2.5	MOC integration formalism . . . . .	37
Figure 2.6	Depletion chain of the uranium cycle . . . . .	46
Figure 2.7	Fission product yields for U235 @0.0253 eV . . . . .	46
Figure 2.8	Fourth order Runge-Kutta integration method . . . . .	48
Figure 2.9	Independent transport-depletion simulations . . . . .	50
Figure 3.1	CFV cell geometry . . . . .	53
Figure 3.2	Convergence of CFV cell $k_{inf}$ in the different evolution temporal scheme of “lattice” APOLLO3 (reference: parabolic scheme) . . . . .	54
Figure 3.3	Impact of the evolution self-shielding of heavy nuclei and fission products on CFV cell $k_{inf}$ . . . . .	56
Figure 3.4	CFV cell $k_{inf}$ comparison during the evolution: Tone Method - Sub-group Method . . . . .	57
Figure 3.5	Relative flux difference with respect to TRIPOLI4 at time 0 . . . . .	60
Figure 3.6	Relative flux difference between APOLLO3 1 spectrum and 4 spectra calculations at time 0 . . . . .	60
Figure 3.7	Relative difference between the Pu239 4 macro group fission spectra and 1 macro group one in the APOLLO3 library. . . . .	61
Figure 3.8	CFV cell $k_{inf}$ comparison during the evolution - APOLLO3 and ECCO with TRIPOLI4 . . . . .	61
Figure 3.9	Reactivity loss due to fission products . . . . .	70
Figure 3.10	$\tau_{abs}^{Fe56}/PROD_{tot}$ comparison between the beginning and the end of the calculation . . . . .	71
Figure 3.11	Impact of the use of 1 energy independent fission spectrum on the CFV cell $k_{inf}$ (ref: 4 macro groups of fission spectra) . . . . .	75

Figure 3.12	MINARET 1968 group “core” calculations compared with reference “lattice” TDT-MOC . . . . .	75
Figure 3.13	Heterogeneous case: CFV cell $k_{inf}$ comparison between MOC reference and core depletion models . . . . .	80
Figure 3.14	Homogeneous case: CFV cell $k_{inf}$ comparison between MOC reference and core evolution models . . . . .	80
Figure 3.15	Heterogeneous case: Relative difference of the fission product concentrations during the evolution . . . . .	81
Figure 3.16	Homogeneous case: Relative difference of the fission product concentrations during the evolution . . . . .	82
Figure 3.17	Heterogeneous case: CFV cell flux comparison in the fuel region between MOC reference and core depletion models at 1440 days . . . . .	84
Figure 3.18	Homogeneous case: CFV cell flux comparison between MOC reference and core depletion models at 1440 days . . . . .	84
Figure 3.19	Heterogeneous case: comparison of U238 absorption reaction rate in fuel region between MOC reference and core depletion models . . . . .	85
Figure 3.20	Relative spectrum variation of the fuel flux within 0 and 1440 days for CFV cells with or without leakage. . . . .	89
Figure 3.21	Leakage case: CFV cell $k_{eff}$ comparison between MOC reference and core evolution models . . . . .	89
Figure 3.22	Leakage case: CFV cell $k_{inf}$ comparison between MOC reference and core evolution models . . . . .	90
Figure 3.23	Leakage case: CFV cell flux comparison between MOC reference and core depletion models at 1440 days . . . . .	90
Figure 3.24	Leakage case: Relative difference of the fission product concentrations during the evolution . . . . .	91
Figure 3.25	Homogeneous case without leakage: CFV cell $k_{inf}$ comparison between 34 point MICRO SIGMA EVOLVING calculation and core evolution models with 17, 9, 5, 3, 2 burn-up tabulation points in the cross section libraries or only 1 (SIGMA ZERO). . . . .	93
Figure 4.1	1/12 cluster fissile-fertile geometry . . . . .	95
Figure 4.2	Reference Evolution Geometry - Flux distribution at $t = 0$ days (normalized to $10^5$ neutron production) . . . . .	97
Figure 4.3	Reference Evolution Geometry - Flux distribution at $t = 1440$ days (normalized to $10^5$ neutron production) . . . . .	98
Figure 4.4	Reference Evolution Geometry - Pu239 distribution at $t = 1440$ days . . . . .	99

Figure 4.5	Reference Evolution Geometry - Pd105 distribution at $t = 1440$ days	100
Figure 4.6	Reference Evolution Geometry - Relative flux difference between BOC and EOC . . . . .	100
Figure 4.7	Reference Evolution Geometry - Reactivity loss due to fission products in fissile region . . . . .	102
Figure 4.8	Reference Evolution Geometry - Reactivity loss due to fission products in fertile region . . . . .	102
Figure 4.9	Fissile-Fertile Cluster $k_{inf}$ comparison between the reference evolution geometry and the simplified one . . . . .	104
Figure 4.10	Homogenized core geometry representing 1/12 fissile-fertile cluster .	104
Figure 4.11	Fissile-Fertile Cluster $k_{inf}$ comparison between MOC reference and core evolution models . . . . .	105
Figure 4.12	Fissile-Fertile Cluster: Relative difference of the fission product concentrations during the evolution in the fissile region . . . . .	107
Figure 4.13	Fissile-Fertile Cluster: Relative difference of the fission product concentrations during the evolution in the fertile region . . . . .	108
Figure 4.14	Fissile-Fertile Cluster: Relative difference of Pu239 concentration during the evolution . . . . .	109
Figure 4.15	Fissile-Fertile Cluster: Relative difference of U238 concentration during the evolution . . . . .	110
Figure 4.16	Fissile-Fertile Cluster: homogenized fissile flux comparison between MOC reference and core depletion models at 1440 days . . . . .	111
Figure 4.17	Fissile-Fertile Cluster: homogenized fertile flux comparison between MOC reference and core depletion models at 1440 days . . . . .	111
Figure 4.18	Fissile-Fertile Cluster: $k_{inf}$ comparison between 34 point MICRO SIGMA EVOLVING and core evolution models with 2 burn-up tabulation points in the cross section libraries or only 1 (SIGMA ZERO) . . . . .	113
Figure 5.1	Core Plane Geometry . . . . .	116
Figure 5.2	Spatial Mesh and Depletion geometry . . . . .	117
Figure 5.3	Initial time flux distribution . . . . .	119
Figure 5.4	Flux distribution at 1440 days . . . . .	119
Figure 5.5	Tc99 concentration map at 1440 days . . . . .	120
Figure 5.6	Pd105 concentration map at 1440 days . . . . .	120
Figure 5.7	Comparison of the MACRO and MICRO SIGMA ZERO evolution calculation with respect to the MICRO SIGMA EVOLVING one. . . .	122



Figure 5.8	2D core plane $k_{inf}$ comparison between 34 point MICRO SIGMA EVOLV- ING calculation and core evolution models with 2 burn-up tabulation points in the cross section libraries or only 1 (SIGMA ZERO) . . . .	123
Figure 5.9	Comparison of the MICRO SIGMA ZERO and MICRO SIGMA EVOLV- ING calculation performed with 4 materials with respect to the MICRO SIGMA EVOLVING one performed with 6 materials. . . . .	124
Figure E.1	Homogenised lattice flux spectrum comparison between BOC and EOC	143
Figure E.2	Fuel lattice flux spectrum comparison between BOC and EOC . . .	143
Figure E.3	Relative flux difference between BOC and EOC . . . . .	144

**LIST OF SYMBOLS AND ABBREVIATIONS**

ASTRID	Advanced Sodium Technological Reactor for Industrial Demonstration
CFV	Coeur Faible Vidange (en: Low Drain Core, LDC)
CEA	Commissariat à l’Energie Atomique et aux énergies alternatives
EDF	Electricité De France
IGN	Institut de Génie Nucléaire de Polytechnique Montréal
LEPh	Laboratoire d’Etudes Physiques
MOC	Method of Characteristics
PWR	Pressurized Water Reactor
SFR	Sodium Fast Reactor

## LIST OF APPENDICES

Appendix A	Rim Effect . . . . .	133
Appendix B	Homogeneous $B_1$ Leakage Model . . . . .	135
Appendix C	CFV Cell Infinite Multiplication Factor . . . . .	139
Appendix D	CFV Cell Isotope Concentrations . . . . .	140
Appendix E	Flux Spectrum Shifting . . . . .	143
Appendix F	33 group energy mesh . . . . .	145

## CHAPTER 1 INTRODUCTION

### 1.1 Generation IV: Challenges and Solutions of the Nuclear Industry

Nuclear technologies for electricity generation were considered mature at the beginning of the 21<sup>th</sup> century. Nevertheless, the objectives to be reached and the challenges to be accepted were still uncountable, because of the growth of energy demand and of the collective consciousness focused on sustainability and environmental issues [1]. If, in fact, nuclear energy has many advantages, it has also disadvantages, as every technology in the delicate world of energy production. Criticisms, fueled by major accidents, have always been casted on this way to produce electricity, demanding higher and higher standards and quality assurances to the nuclear industry. An industry of high level and of strategic importance, capable of enriching a country both with its assets and high level formation. An industry capable of exploiting a carbon free and high density energy source as the fission one; but also misunderstood by the major public, because perceived as the awkward tamer of sinister and destructive forces (the “original sin” of the nuclear bomb) and as the producer of long term highly radioactive waste. Contrasting opinions on nuclear safety and sustainability, and the constant threatening of the proliferation, existed at that time and they were incapable to attract the sympathies of the local political legislation of several countries. As a consequence, moved by the necessity of giving an answer to the major questions of the future energy policies, and conscious that a “bold new idea” [1] was necessary for a change in mentality, 9 countries (Argentina, Brazil, Canada, France, Japan, Republic of Korea, Republic of South Africa, United Kingdom and United States) signed the Generation IV International Forum Charter in July 2001. Switzerland, Euratom, Russian Federation and People’s Republic of China joined in between 2002 and 2006.

The aim of this international organization is to coordinate an international cooperation for the Research and Development (R & D) for advanced nuclear energy systems. Four goals to be achieved in such systems have been established:

- **Sustainability:** Generation IV energy systems must decrease CO<sub>2</sub> production and reduce polluting emissions. They must exploit better the natural resources in order to minimize nuclear waste production.
- **Economics:** Generation IV energy systems must be competitive with respect to those exploiting other energy sources.
- **Safety and Reliability:** Generation IV energy systems must be more safe and reliable.

Severe accidents less probable and no offsite emergency response are key features of these systems.

- **Proliferation Resistance and Physical Protection:** Generation IV energy systems must be an unattractive way to produce weapon usable materials, and they must provide enhanced physical protection against act of terrorism.

As a result of group discussions and collective deliberations, 6 nuclear reactor systems have been chosen satisfying the desired criteria. These reactors are shown in table 1.1. It is important to note that 4 out of 6 of these design concepts exploit fast neutron spectrum. The reason for such a choice, and its importance for the future, is the subject of the next section.

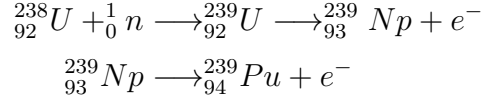
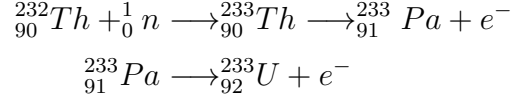
## 1.2 FNR: Fast Nuclear Reactor

A nuclear reactor is a device where the energy released by fission is exploited in a controlled way in order to produce electricity. Indeed, a chain reaction is sustained. A delicate equilibrium in the neutron population of the core is assumed: each fission event produces several neutrons, but, amongst them, one and one only undergoes another fission reaction (*criticality condition*). The average number of secondary neutrons produced by fissile isotope is currently defined with  $\nu$ . This number is not constant and it increases, more or less linearly, with the incident neutron energy. At the same time, the neutrons which do not lead to a fission event, they undergo other nuclear reactions, such as radiative capture, both in the fuel and in the surrounding materials, or they escape the reactor. The isotopes which undergo fission events are called *fissile* and they are the “fuel” of our reactor. Differently from other technologies, however, these isotopes can not only be consumed by fission events or other reactions, but also be produced. An isotope which can transmute into a fissile one after a nuclear reaction is called *fertile*. The most important fertile isotopes are Th232 and U238.

Table 1.1 Characteristics of the six Generation IV nuclear reactor systems

System	Neutron spectrum	Coolant	Size (MWe)
VHTR (very high temperature reactor)	Thermal	Helium	100-300
SFR (sodium-cooled fast reactor)	Fast	Sodium	50-1500
SCWR (super-critical water cooled reactor)	Thermal/Fast	Water	1000-1600
GFR (gas-cooled fast reactor)	Fast	Helium	1000
LFR (lead-cooled fast reactor)	Fast	Lead, Pb/Bi	20-1200
MSR (molten salt reactor)	Epithermal	Fluoride Salt	1000

The transmutation of the two is subjected to the following:



where it is possible to see that the fertile isotopes transmute into the fissile ones U233 and Pu239 after a radiative capture and the occurrence of  $\beta^-$  decays.

Quantitatively, the conversion ratio  $C$  [2] describes this phenomenon. It is defined as the ratio between the average number of fissile atoms produced and the ones consumed in a reactor. This ratio is of major importance and having it greater than unity is an advantageous situation, allowing to define the breeding gain  $G = C - 1$ . This number describes, on the average, the fissile isotopes “gained” per atom consumed. Building a nuclear reactor where such conversion constraint is satisfied requires another condition in addition to the criticality one: each fission event must imply another fission event and also a neutron which transmutes a fertile isotope. In order to satisfy this second constraint, it is necessary to build a reactor where  $\nu$  is higher and where parasitic captures are inhibited. Both these conditions are met in Fast Nuclear Reactors (FNRs), i.e. reactors which exploit fission by neutron having energies higher than 100KeV.

Nowadays, thermal reactors are the most common technology used for electricity generation from nuclear power. They exploit neutron with energies lower than 1eV. Historically, they were the first operated reactors, because of the smaller mass required to assure critical condition, with the fission reaction being more probable at thermal energies. Neutrons are produced by fission with an average energy of the order of the MeV and then thermalized by means of a moderator. For example, Pressurized Water Reactor (PWR) light water is used both as a coolant, to remove thermal energy released by fission, and as a moderator. It is obvious that, in such a system, a loss of coolant, or simply a decreasing of water density due to more power released, does not allow to satisfy the criticality condition, because of lack of moderation. In FNR, on the other hand, the moderator is not used - neutrons are not thermalized - but, of course, the coolant is required. The latter is chosen to be as transparent to neutrons as possible in order not to thermalize nor to capture them. A loss of coolant,

in such a system, not only can allow to satisfy criticality condition, but also it can decrease the number of parasitic captures making the reactor supercritical (on the average more than one fission event generated after an initial fission). These discussions introduce the subjects of the next sections: sodium cooled FNR and the ASTRID project.

### 1.3 SFR: Sodium-cooled Fast Reactor

In 1973, an oil crisis led country such as Japon and France, greatly penalized by oil import, to start a massive nuclear program. France, from its side, started to equip itself with the U.S. PWR technology. Electricity production for nuclear energy, then, has grown throughout the years, resulting in an increasing consumption of natural resources, uranium in this case. This element, in fact, is the fuel of PWRs. But not the whole uranium mass is exploited, only the 0.7% of it, equal to the mass concentration of U235 in natural uranium, principally composed by U238. At the beginning of 21th century, the same period GIF Charter was signed, it was common knowledge that actual exploitation of uranium resources was not guaranteed to last until the end of the century, even in the best possible scenario [3]. FNRs were introduced as a promising technology: fast spectrum, as already explained, allows to transmute U238 in Pu239 opening the possibility to a full exploitation of the natural uranium. But it is important to notice that the idea of fast spectrum reactor was not new at that time. In 1951, the first reactor to produce electricity was a liquid metal cooled fast reactor named EBR1. Technologically, it was easier to build: liquid metals present high conductivity and they can operate at high temperature and at atmospheric pressure. But also another reason moved the realization of a first generation of FNRs: in the first decade after WWII plutonium seemed easier to produce than natural uranium to find. Localization of ores and their exploitation was not easy at the beginning [4]. If, at the moment, FNRs seem the only way to assure a less polluting and durable energy source, SFRs have already been operated. Concerning the French situation, PHENIX and SUPERPHENIX were built and operated in the past. Such kind of reactors, now, will guarantee, with the actual french stock of uranium, energy production from nuclear source for the next 5000 years [3]. Five millenniums against less than a century.

Along with a better utilization of natural resources, FNRs will be used to close the fuel cycle of plutonium, burning in such systems the mass of this element that has been continuously produced in the operation of previous reactors. In addition, this kind of reactors will consume the transuranic, reducing, therefore, the intrinsic radiotoxicity of nuclear waste. Such a scenario will be of unutterable interest for the future.

Even if few technological advantages have already been enlisted, concerning the realization of

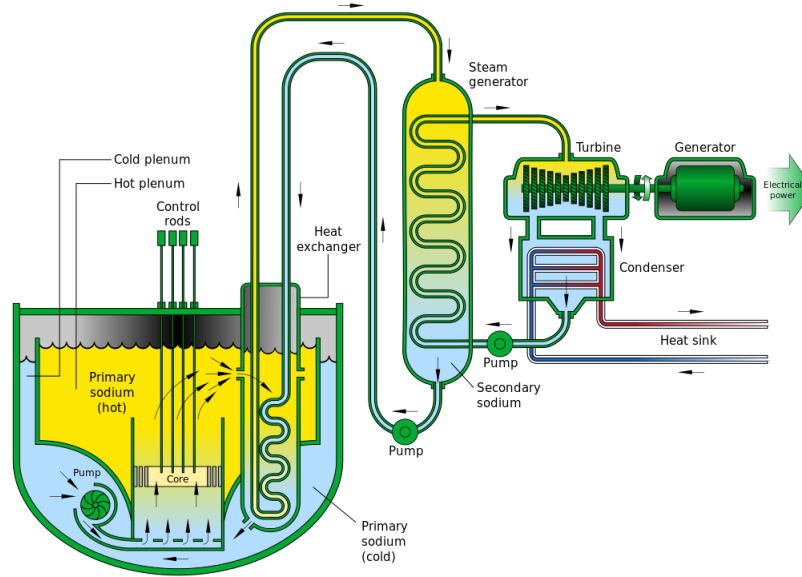


Figure 1.1 SFR scheme

this kind of reactors, other challenges are present, beginning from the choice of the coolant. Sodium seems to be an optimum candidate, because it is available at low price and it possesses a good thermal range of operation, with a fusion point at  $97.85^{\circ}\text{C}$  and a boiling one at  $882.85^{\circ}\text{C}$ . A good margin before boiling is also guaranteed, with a latent heat more than twice that of water. As other liquid metals, it is an excellent thermal conductor and it does not require to be operated at high pressure. Moreover, from a neutronic point of view, it is almost transparent to neutrons and it does not present major activation problems. On the other hand, it is very reactive and it is only present bounded to other elements in nature. It is unstable and easily reacts with water, requiring an intermediate circuit between the primary and the power ones for safety reasons. In figure 1.1, it is possible to distinguish the primary circuit, which removes the heat from the core, and the intermediate circuit, which is used as a junction of the primary with the power circuit, the one whose fluid actually operates the turbines.

Furthermore, another disadvantage of sodium is its opacity, that makes reactor inspections harder. Nevertheless, several attempts of SFR construction have already been made in the past (PHENIX, SUPERPHENIX, MONJU) identifying the major problems and technological challenges, but also giving the opportunity to enrich the knowledge about such systems and to gain the right skills and expertise. In such a scenario, the ASTRID prototype introduces itself as the first GENIV FNR to be build. This reactor is a sodium-cooled one (SFR).



## 1.4 ASTRID: Advanced Sodium Technological Reactor for Industrial Demonstration

In October 1945, General de Gaulle created the “Commissariat à l’Énergie Atomique” (CEA), making France the first country in the world in having a civil organization concerned to the study of nuclear energy and its application. A civil organization, but with a particular regard on defence matters. The nuclear bombs of that year, in fact, particularly concerned the leader, conscious that an answer was required to those “travaux d’apocalypse” (works of apocalypse) as he called them in his Mémoires. From that time everything has changed, even the name of this organization. CEA now stands for “Commissariat à l’Énergie Atomique et aux énergies alternatives”, reflecting the new challenges and the new needs this institution is called to cope with. In the first section, the major concerns of the GIF have been introduced. This forum was an occasion for few countries - France among them - to realize analysis and studies in order to evaluate the technological level achieved and the knowledge accumulated previously regarding nuclear technologies. As a result, SFR seems the technology where France has acquired a competitive edge [5].

In June 2006, the French government passed a law focused on the disposition of long life high activity waste. A prototype, capable of transmutation and separation of long life isotopes, was scheduled for the end of 2020. ASTRID project began and CEA was given the responsibility for the operational management, core design and R& D work. CEA, along with its industrial partners (French ones: EDF, AREVA etc. and international ones: TOSHIBA etc.), presented a first timetable in 2012 (see figure 1.2).

As already said, ASTRID is the prototype of a GENIV reactor and, as a consequence, it must achieved the requirements established by the GIF. The major objective, of course, is to build a prototype which can exploit better the natural resources (uranium, transuranic) and which can allow to close the fuel cycle. Being a prototype, this reactor will be only the first step of a long path; a path that will lead to the beginning of a new reactor series CO<sub>2</sub>-free, sustainable and profitable from an economic point of view. Indeed, the choice of the power (600MWe) is reasonable to extrapolate a business plan for future analogous reactors. Reactors that must reach a target reliability of 80%, assuring a constant power production, one weak side of PHENIX and SUPERPHENIX.

All these goals must be reached in a structure of improved safety. Water-sodium reactions, a major problems in SFR, are avoided using a N<sub>2</sub> power cycle: a Brayton cycle at 180 bar. The research of an increased thermal inertia to assure passive safety along with a better inspectability of the structures, results in a new core conception. This core, that resolves major reactivity problems related to SFR, is called “Coeur à Faible Vidange” (CFV), and it

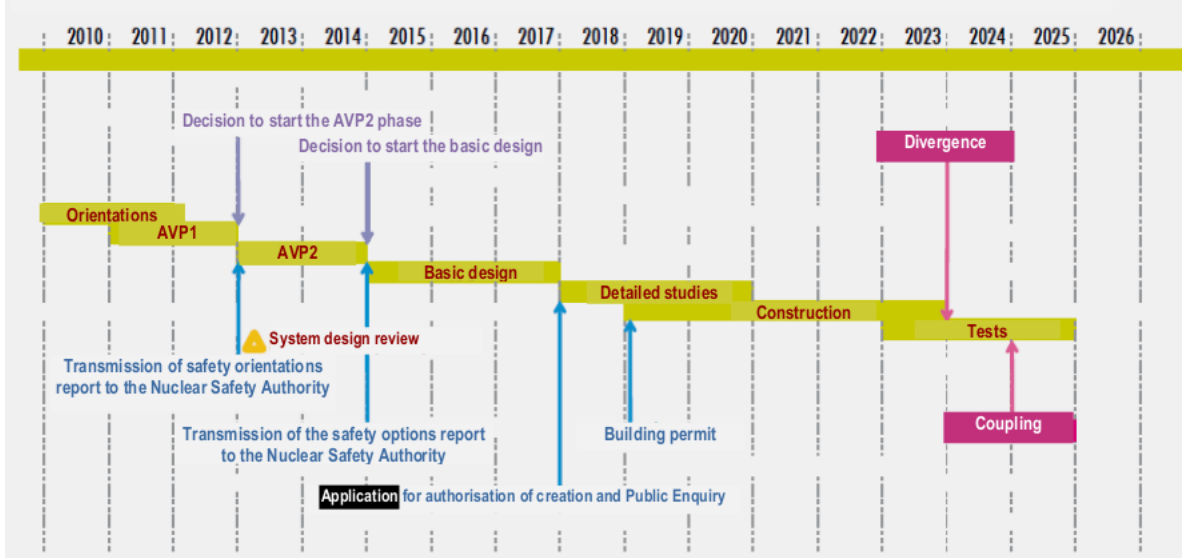


Figure 1.2 Overall schedule of the ASTRID project

will be the subject of the next paragraph.

### 1.5 CFV: Coeur à Faible Vidange

The chain reaction is sustained in the core. A multiplicative medium is, then, designed in order to guarantee the desired performances. But not only neutronic considerations move core designers. Structural and thermohydraulic necessities are also taken into account. As already introduced in section 1.2, a coolant is required in order to remove heat from the core and guarantee the normal operation of the reactor. While in thermal reactors the coolant can also give a neutronic advantage moderating neutron, in fast reactors it is a source of parasitic absorptions. If void replaces the coolant, a reactivity gain can be theoretically reached. The same occurs if the structure collapses or the core melts down at the bottom of the vessel: neutron multiplication in the geometry is enhanced due to the removal of all the structures interposed between the multiplicative mediums. This effect can be relatively reduced increasing the fuel to coolant surface ratio. ASTRID fuel pins, indeed, have a larger radius and a reduced height. The core of a FNR is not at its most reactive geometry [6]. CFV conception, therefore, is a trade off between performances (zero or positive breeding gain, weak reactivity loss during the cycle) and safety concerns. The latter want to avoid more reactive geometries. Doppler effect is enhanced in the core conception so that power excursion are limited. Neutron induced reactions are inhibited where neutron temperature increases. Consequently, an increase in neutron population, that is translated in an increase

of fission events, makes fuel temperature rise, introducing a negative feedback, the Doppler effect, which decreases the neutron population.

In addition, as it is possible to see in figures 1.3 and 1.4, fertile and fissile zones are created within the core in order to increase the flux heterogeneity. A sodium plenum zone is located in the upper part of the core, under an absorbing protection. Axial dimension are reduced in order to exploit neutron leakage in case of “voided” configurations, i.e. configurations where sodium mass is reduced or is absent. In such states, sodium absorption is reduced and, in order to ensure a neutron balance so that production is not enhanced, leakage towards the upper regions increases. Neutrons are, then, absorbed in the absorbing protection, that prevents them from returning into the core. Sodium boiling or core draining, therefore, does not lead to more reactive geometries. This conclusion has been extrapolated also to larger industrial cores [6]. This conception, as a result, satisfies the following objectives:

- favourable transient in case of unprotected loss of flow and heat sink
- no sodium boiling in case of unprotected loss of station supply power (ULOSSP)
- favourable behaviour in case of control rod withdrawal (CRW)

In conclusion, CFV is a core conception of enhanced safety. This result is achieved throughout a core design which guarantees limited power excursion if fuel temperature increases (Doppler effect), and which does not assure a reactivity gain if sodium boils or core is completely drained; a core design which has, and wisely exploits, its non homogeneous neutron population distribution.

## 1.6 APOLLO3: A new code for new challenges

The heterogeneities described in the previous section and the importance of correctly evaluating the physical quantities of interest during SFR operation require new numerical tools for reactor simulation. As a result, in 2009, CEA, with the support of AREVA and EDF, decided to focus on the development of the new deterministic multi-purpose code APOLLO3 and on its fast reactor applications.

### 1.6.1 Nuclear Code Scenario

From its conception to the actual operation of a nuclear reactor, it is of major importance to know the distribution of neutron population throughout the core. In order to do so, an equation, that will be presented in the following chapter, must be solved. This equation was

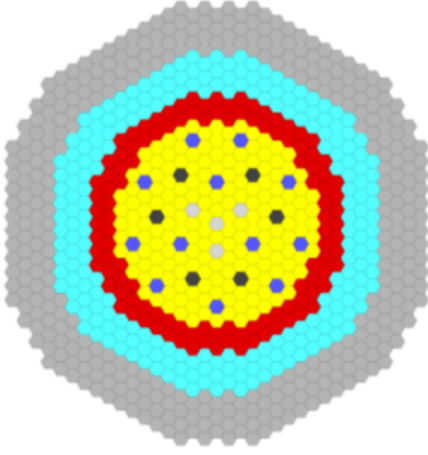


Figure 1.3 CFV core layout

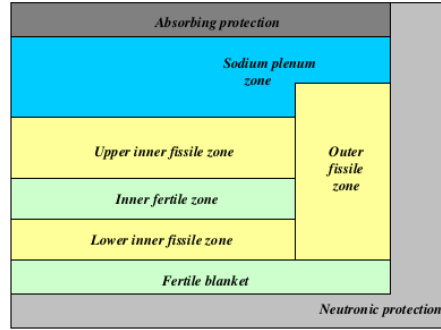


Figure 1.4 CFV core geometry

first introduced by Ludwig Boltzmann to describe transport phenomena in gas. Lately, with the beginning of reactor physics, it was reformulated, to describe neutron transport phenomena as well. This equation simply takes into account that neutrons are neutral particles which move in a certain geometry, generally a reactor core or a part of it for the purpose of this thesis work. Being neutral particles, they are not subjected to electromagnetic fields and their paths proceed in a straight line. Neutrons can escape the geometry under consideration, or induce a reaction. They can collide - beginning a new straight path with a different orientation - or be absorbed. Absorption can imply different nuclear reactions, and fission is among them. Fission produces other neutrons that start again an analogous cycle. Each part of this neutron cycle is described by a proper mathematical operator in the Boltzmann equation. Unfortunately, this equation can't be solved analytically. Numerical solution methods, consequently, are required. Nuclear codes are computer programs aiming to solve numerically the Boltzmann equation in practical situations introducing reasonable hypothesis.

Nowadays, nuclear codes are divided into two major categories: Monte Carlo and deterministic codes. The former use a stochastic approach and are based on the random walk concept: neutron paths are simulated, generations after generations, no matter the geometry of interest. Neutron distribution is acquired through the minimum possible number of hypothesis. The disadvantage is that such precision is reached with a great computational effort. This effort, which is translated in a great computational time for ordinary computer, is accomplished for reference calculations only, for the time being. Excluding supercalculator, widespread present technologies are not capable to perform Monte Carlo calculations in reasonable time. Consequently, for industrial applications, deterministic codes are preferred. These codes are based on a proper discretization of the Boltzmann equation.

At the present time, full core calculations are performed in two steps. These steps are performed using different resolution techniques, applied on different geometries and with different spatial and energy meshes. The first one is the lattice step, performed with the utilization of lattice codes. Such codes resolve the transport equation in reference geometries - usually 2D cells or assemblies - with a finer energy mesh and spatial discretization. The aim of such step is the energy condensation and the spatial homogenization of the parameters of interest for the following step, the core one. These parameters are for example cross sections, isotopic concentrations, leakage coefficient etc. They are stored in Multi Parameter Database and used as input data for next calculations.

The core step performs full core calculations with a coarser energetic mesh and spatial discretization. Proper techniques are used to deal with 3D reactor geometries and apply thermodynamical and kinetic models in order to simulate operational and accidental conditions. As it is possible to note, core calculations are the result of a synergistic effort of more than one code. Along with lattice and core codes, it is necessary to take into account all the codes which elaborate the nuclear data. All these codes, together, compose a platform. In France, the platform used by CEA, EDF and AREVA is composed by: a code that treats nuclear data and estimates uncertainties: CONRAD [7]; a code that evaluates proper input data libraries for deterministic and stochastic codes: GALILEE [8]; a reference Monte Carlo code: TRIPOLI4 [9]; a deterministic lattice code used principally for thermal and epithermal reactors, APOLLO2, and its core counterpart CRONOS2 ; a deterministic lattice code used for fast reactors, ECCO, and its core counterpart ERANOS [10]. As it will be discussed later, during the fuel cycle, inside and outside the core, material compositions change, because of neutron induced reaction and radioactive decay. A depletion code which describes such evolution is consequently required to complete the platform. DARWIN3 is currently used by the French organization presented above [11].

### 1.6.2 APOLLO3: General Objectives

A neutronic platform is a simulation tool and its aim is the evaluation of certain physical quantities in certain configurations, applying proper models. As seen in previous sections, reactor configurations and core conceptions change, requiring new simulation tools. Tools that can also implement new physical models and new mathematical algorithms, exploiting new computer architectures. That's why the life cycle of nuclear codes is equal to, more or less, 40 years. APOLLO3 aims to replace the codes APOLLO2, CRONOS2 and ERANOS. It is coupled with the depletion code MENDEL [12].

APOLLO3 is a new code whose key objective is to merge together the lattice and core steps

in one single code, in order to accomplish one step calculations in the future. In order to do so, computer architectures must be exploited at their best. This is accomplished through the use of massive parallelization. Three main levels of parallelization are considered [13]:

- **Multi Parametrized calculations:** through core subdivision in macro geometries. Multi parameters assemblies calculations are a classical example.
- **Multi Domain calculations:** through the subdivision of the considered geometry in smaller ones and the utilization of domain decomposition techniques in order to reconstruct the mutual dependencies between them
- **Grain Parallelization of the solvers:** exploiting the parallelism of the numerical methods used

However computational time is not the only request of nuclear industry. Other objectives are the following [14]:

- **Flexibility:** from high precision calculations to industrial design
- **Easy coupling** with Monte Carlo and Thermohydraulic/ Thermomechanical codes, including coupling with the SALOME platform [15]
- **Extended application domain:** performing criticality and shielding calculations for all kinds of reactors (a multi spectrum code for FNR, PWR and experimental reactors)
- **Uncertainties assessments** using perturbation methods

### 1.6.3 APOLLO3: A Core Physics Simulation Tool for ASTRID CFV

As already said, an important goal is to develop a multi-purpose code. Of major interest for this thesis are APOLLO3 applications in the simulation of ASTRID CFV core. The major problems arising from ASTRID innovative features are related to the correct simulation of the following elements [13]:

- **radial blanket** loaded with minor actinides
- **neutron shielding** and **reflector**
- **sodium plenum** and **fertile plate**
- flux distribution in a core with outer core height greater than inner one (**Diabolo effect**)

All such problems must be taken into consideration and evaluated in order to supply a reliable code to users and designers. That's why a rigorous method, called VVUQ (Verification, Validation and Uncertainty Quantification), has been used. The general scheme is composed in the following way:

- **Verification:** internal coherence and numerical results of the solvers are verified through non regression test
- **Validation:** in order to evaluate the accuracy of neutronic models and calculation schemes, comparisons with the reference Monte Carlo code TRIPOLI4 are performed
- **Uncertainty Quantification:** the global package, including APOLLO3, the codes which treat the evaluated nuclear data and the nuclear data themselves, is tested comparing it with measurements from dedicated experimental programs. Experimental uncertainties are transposed to neutronic design parameters

Inside such scheme, it is possible to introduce the work of the author, as it will be explained in the next section.

## 1.7 Objective of the Thesis

The aim of this thesis is to validate a depletion model which is capable to correctly represent the isotope evolution in a SFR core. As will be explained in section 3.2, two major categories of depletion models can be distinguished: macroscopic depletion and micro-depletion. Because depletion models are applied to core calculations, they use condensed and homogenized quantities deriving from proper lattice steps. For thermal reactors, depletion lattice calculations are performed and their quantities are stored, at each time step, in proper time-dependent multi-parameterized libraries (known as SAPHYB or MPO databases in french chain of calculation). The ECCO/ERANOS calculation scheme for fast reactors, on the contrary, performs only time zero lattice calculations in order to create a time zero library. A proper micro-depletion model, then, is applied for core calculations. In this work, this model will be called MICRO SIGMA ZERO ( $\sigma_0$ ). It is based on the approximation that multi-parameterized libraries in SFRs are time independent. This approximation leads to a time-saving model (no lattice depletion calculations are performed, only time zero ones) which require less memory for the library storage. Libraries, in fact, are not time parameterized.

This thesis is an opportunity to re-discuss this approximation and to answer the question: *Is*

*the ECCO/ERANOS MICRO SIGMA ZERO model accurate enough to describe the isotope evolution in CFV configuration with the aid of APOLLO3 code?*

## 1.8 Contents of the Thesis

In order to answer the research question previously introduced, this thesis will be organized in 6 chapters. After a brief introduction on the background of the ASTRID project and the French nuclear code scenario, a proper literature review of the methods used to solve the Boltzmann and the depletion equations is proposed in chapter 2. In chapter 3, different depletion models are introduced and compared for a single cell geometry. Lattice depletion is validate with respect to TRIPOLI4 and ECCO. Optimized evolution parameters are found and set for the following lattice calculations.

In chapter 4, a fissile-fertile cluster geometry is discussed. The first part of the chapter focuses on the lattice evolution geometry, while the second compares the depletion models. In chapter 5, a 2D core plane geometry is investigated. Although several approximations are made, this geometry gives an idea of the behaviour of the models in a more complex configuration. In chapter 6, conclusions are discussed and future work is proposed.



## CHAPTER 2 LITERATURE REVIEW

### 2.1 The Transport Equation

The linear form of the Boltzmann transport equation is derived in this section. Particle balance in a control volume during time interval  $\Delta t$  is assured, neglecting neutron-neutron interaction. This simplifies the problem avoiding the introduction of a non linear term. The notation used in this work follows [16]. Further information can be also found in [2, 17].

First of all, the concept of neutron density  $n$  is defined:

$$n(\vec{r}, \vec{\Omega}, v_n, t) = \frac{\text{\#neutrons}}{\text{unit volume, solid angle and velocity}} \left[ \frac{\text{neutrons}}{\text{cm}^3 \cdot \text{cm/s} \cdot \text{sr}} \right]$$

$n$  is a probability density and, as it is possible to notice, it depends upon 7 variables:

- 3 spatial variables  $\vec{r}$ , describing the position where the neutron density is evaluated
- 2 angular variables  $\vec{\Omega}$ , describing the direction this neutron population is travelling to
- 1 energy variables  $v_n$ , describing the speed the neutron population is travelling at (that in a non relativistic approximation can imply a kinetic energy equal to  $E_k = \frac{1}{2}m_n v_n^2$ , where  $m_n$  is the neutron mass)
- 1 time variable  $t$ , describing the time which the neutron population is considered at.

In a control volume  $C$ , the total number of neutrons whose speed is included in the interval  $[v_n, v_n + dv_n]$  and whose travelling direction sweeps the solid angle  $d^2\Omega$  is equal to

$$n_{tot} = \int_C d^3r \, n(\vec{r}, \vec{\Omega}, v_n, t) dv_n d^2\Omega \quad (2.1)$$

This integral neutron population can change in the time interval  $\Delta t$ . The change  $\Delta n_{tot}$  is equal to

$$\Delta n_{tot} = \int_C d^3r \left[ n(\vec{r}, \vec{\Omega}, v_n, t + \Delta t) - n(\vec{r}, \vec{\Omega}, v_n, t) \right] dv_n d^2\Omega \quad (2.2)$$

In this time interval, the neutron population can decrease due to collision events or leakage. Introducing the concept of total macroscopic cross section  $\Sigma(\vec{r}, v_n, t)$ , which quantifies the interaction probability per unit of travelling path with one of the possible present nuclei, for a neutron located in  $\vec{r}$  with a speed  $v_n$ , no matter the incident direction, the number of

collision in the control volume  $C$  in the time interval  $\Delta t$  is equal to:

$$\Delta Coll = \int_C d^3r \Sigma(\vec{r}, v_n, t) \left[ v_n n(\vec{r}, \vec{\Omega}, v_n, t) \right] dv_n d^2\Omega \Delta t \quad (2.3)$$

where  $\Sigma(\vec{r}, v_n, t)v_n$  identifies the probability per second of a collision event.

The number of neutrons which escapes the control volume, then, is

$$\Delta Leak = \int_{\delta C} d^2r \left[ (\vec{\Omega} \cdot \vec{N}) v_n n(\vec{r}, \vec{\Omega}, v_n, t) \right] dv_n d^2\Omega \Delta t \quad (2.4)$$

where  $\delta C$  identifies the surface of the control volume and  $\vec{N}$  its outgoing normal vector.

Applying the divergence theorem:

$$\Delta Leak = \int_C d^3r \left[ \vec{\nabla} \cdot (\vec{\Omega} v_n n(\vec{r}, \vec{\Omega}, v_n, t)) \right] dv_n d^2\Omega \Delta t \quad (2.5)$$

It is possible to collapse the product between the neutron speed and the population density introducing a scalar quantity called angular neutron flux:

$$\phi(\vec{r}, \vec{\Omega}, v_n, t) = v_n n(\vec{r}, \vec{\Omega}, v_n, t) \quad \left[ \frac{\text{neutrons}}{\text{cm}^2 \cdot \text{s} \cdot \text{cm/s} \cdot \text{sr}} \right]$$

However, during the time interval, in the control volume, neutrons can be generated. For the time being a source density, which will be properly described later in this work,  $Q(\vec{r}, \vec{\Omega}, v_n, t)$  is introduced, making possible to express the generation term as follows:

$$\Delta Gen = \int_C d^3r \left[ Q(\vec{r}, \vec{\Omega}, v_n, t) \right] dv_n d^2\Omega \Delta t \quad (2.6)$$

It is possible to sum up all this information writing the following balance:

$$\Delta n_{tot} = -\Delta Coll - \Delta Leak + \Delta Gen \quad (2.7)$$

Discarding the volume integral and making explicit the angular flux where it is possible, the balance can be rewritten:

$$\begin{aligned} \frac{n(\vec{r}, \vec{\Omega}, v_n, t + \Delta t) - n(\vec{r}, \vec{\Omega}, v_n, t)}{\Delta t} = \\ = -\vec{\nabla} \cdot (\vec{\Omega} \phi(\vec{r}, \vec{\Omega}, v_n, t)) - \Sigma(\vec{r}, v_n, t) \phi(\vec{r}, \vec{\Omega}, v_n, t) + Q(\vec{r}, \vec{\Omega}, v_n, t) \end{aligned}$$

Considering that the neutron travelling direction does not depend on the spatial variables  $\vec{r}$  and taking the limit  $\Delta t \rightarrow 0$ , it is possible to write the **differential form of the transport**

equation:

$$\frac{1}{v_n} \frac{\partial \phi(\vec{r}, \vec{\Omega}, v_n, t)}{\partial t} + \vec{\Omega} \cdot \vec{\nabla} \phi(\vec{r}, \vec{\Omega}, v_n, t) + \Sigma(\vec{r}, v_n, t) \phi(\vec{r}, \vec{\Omega}, v_n, t) = Q(\vec{r}, \vec{\Omega}, v_n, t) \quad (2.8)$$

## 2.2 Cross Sections

In the previous section, the total macroscopic cross section  $\Sigma(\vec{r}, v_n, t)$  has been introduced. This cross section is the sum of all the macroscopic cross sections which describe neutron induced nuclear reactions such as capture, scattering, fission and spallation reactions, only to list the most important in reactor physics:

$$\Sigma(\vec{r}, v_n, t) = \sum_x \Sigma_x(\vec{r}, v_n, t) \quad (2.9)$$

where  $x$  is a general neutron induced nuclear reaction.

These reactions can occur with more than one isotope, making these terms the results of a summation over the  $N_{iso}$  isotopes considered as well:

$$\Sigma_x(\vec{r}, v_n, t) = \sum_{i=1}^{N_{iso}} \Sigma_{x,i}(\vec{r}, v_n, t) \quad (2.10)$$

$\Sigma_{x,i}(\vec{r}, v_n, t)$  is linearly proportional to the isotope concentration  $N_i$  throughout a coefficient  $\sigma_{x,i}(v_n)$ :

$$\Sigma_{x,i}(\vec{r}, v_n, t) = N_i(\vec{r}, t) \sigma_{x,i}(v_n) \quad (2.11)$$

$\sigma_{x,i}(v_n)$  is called microscopic cross section and it is a physical property of the considered isotope. This quantity is a proportional coefficient introduced to estimate the effective interaction area which a motionless nucleus seen by an incident neutron. Its unit of measure is the barn, defined as follows:

$$1b = 10^{-24} cm^2$$

Microscopic cross sections are the fundamental data required in reactor physics calculations. The correct evaluation of these cross sections is greatly important and it is the result of experiments, theoretical models and uncertainty quantification. These evaluated data are stored in JEFF (Joint Evaluated Fission and Fusion file) libraries, following an American format called ENDF (Evaluated Nuclear Data File). These data libraries are constantly revised and are set to JEFF3.1.1 version for this work [18]. JEFF libraries contain all the data of interest in reactor physics and criticality application, including neutron and photon induced reactions, for a range of incident neutron energy from  $10^{-5}$  eV to 150 MeV. Cross

section values are stored in a pointwise format and interpolation functions are provided in order to reconstruct continuous function  $\sigma(E_n)$ .

In figure 2.1, it is possible to see the microscopic cross section of U238, as a function of the incident neutron energy, for capture and fission. It is possible to notice that  $\sigma(E_n)$  is not a monotonous function, but presents a large number of peaks called resonances. Nuclear energy levels are not continuous, but discrete. Incident neutron energies, which correspond to well defined excitation levels, present higher interaction probability. Resonances are studied with experimental data, but above 10 keV they become impossible to resolve for heavy nuclei. Statistical approach and theoretical models are used in order to cope with this problem. CEA uses CONRAD [7] in order to create its evaluated nuclear data libraries to be included in JEFF3.1.1; this code merges empirical results and theoretical estimations in order to guarantee high quality evaluations with the associated uncertainties.

In figure 2.2, it is possible to observe a scheme which shows how input cross section libraries are created for stochastic and deterministic code. The major difference is that stochastic codes use pointwise libraries, while deterministic codes use groupwise ones. The latter present group-averaged cross sections: to each energy group an averaged value is associated based on equation:

$$\Sigma^g(\vec{r}) = \frac{1}{\phi^g(\vec{r})} \int_{E_{g+1}}^{E_g} dE \Sigma(\vec{r}, E) \phi(\vec{r}, E) \quad (2.12)$$

This multi-group approach tends to flatten the resonances observed in figure 2.1: only one value must represent an energy domain that can contain numerous resonances. In order to account for the resonances, preserving group-wise cross section libraries, probability tables are introduced. They are created using CALENDF code [19]. A description of how they are created is beyond the purpose of this work. For the moment, it is worth saying that probability tables provide quadrature formulas to evaluate Lebesgue integral. Each weight  $\omega_k$  is associated to the probability that, inside the energy group  $G$ , the cross section  $\sigma_{x,i}$  assume a certain value  $\hat{\sigma}_{x,i}$ . Probability tables are also used in Monte Carlo codes for the resonance description of the unresolved energy domain ( $E > 10$  keV) [20].

Concerning the resonances, another effect must be accounted.  $\sigma_{x,i}(v_n)$  has been defined to represent the interaction probability between an incident neutron at  $v_n$  velocity and a motionless nucleus. However in reactor physics application nuclei are not motionless, they have a proper temperature and velocity  $v_A$ . The probability distribution of the nuclei velocity for materials at thermal equilibrium, follows the Maxwell-Boltzmann distribution [16]. The interaction probability, hence, is not related to the incident neutron velocity  $v_n$ , but to the relative neutron-nucleus one:

$$v_R = |\vec{v}_n - \vec{v}_A|$$

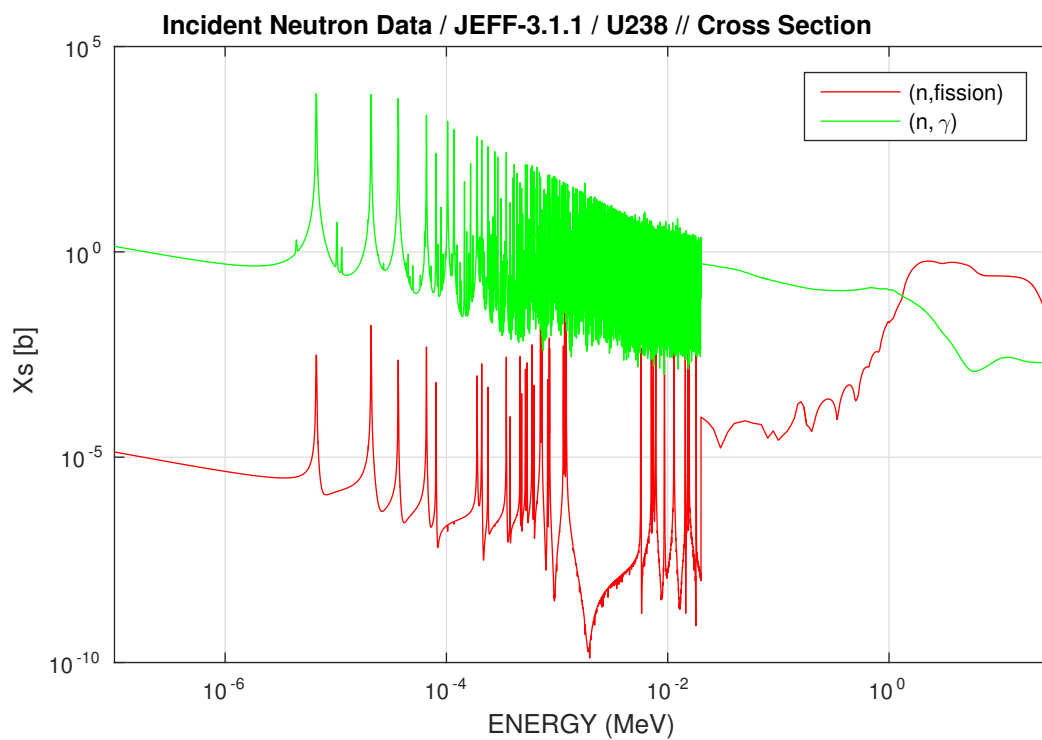


Figure 2.1 Capture ( $n,\gamma$ ) and Fission ( $n,\text{fission}$ ) U238 cross sections

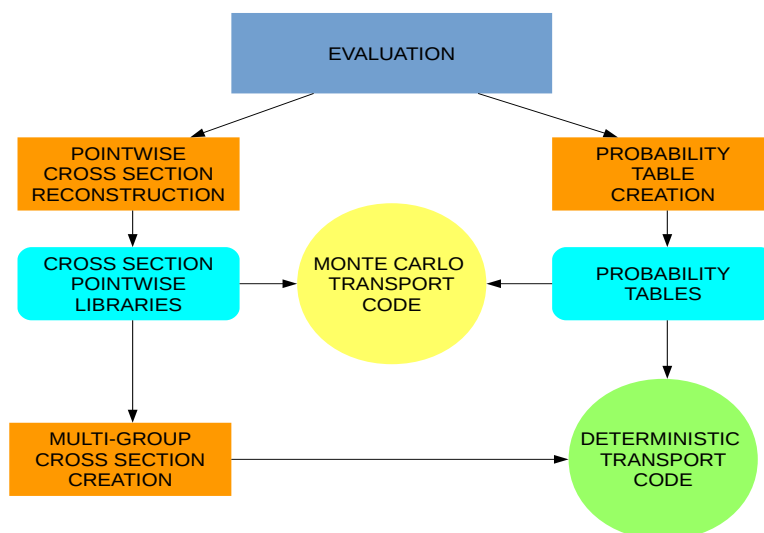


Figure 2.2 Input Cross section library creation scheme

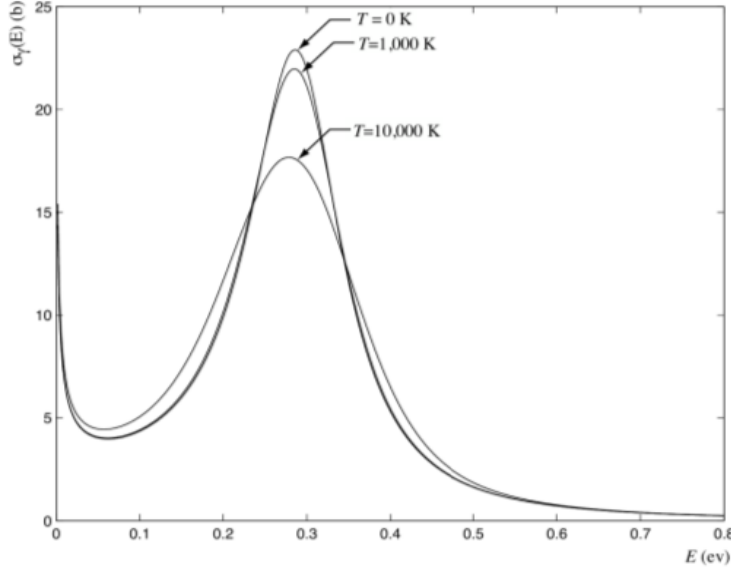


Figure 2.3 Doppler-Broadening Effect

$p(\vec{v}_A)$  is the Maxwell-Boltzmann probability distribution at a defined temperature  $T$ . The actual cross sections used in input libraries are a convolution, throughout the whole energy domain, of the 0 K cross sections by  $p(\vec{v}_A)$ :

$$\bar{\sigma}_{x,i,T}(v_n) = \frac{1}{v_n} \int_{\infty} d^3v_A p(\vec{v}_A) |\vec{v}_n - \vec{v}_A| \sigma_{x,i}(|\vec{v}_n - \vec{v}_A|) \quad (2.13)$$

The effect of the convolution is observable in figure 2.3. Increasing the temperature, the peak height decreases. This fact can be explained thinking about the resonance peak associated to  $v_n$  velocity at 0 K. If the nucleus is motionless, there is only one neutron velocity  $v_n$  associated to that energy of the neutron-nucleus system; if the nucleus starts moving, more neutron velocities can compose the energy required for the interaction. The probability peak is reduced, spread over a greater number of velocities. It is important to notice that formula 2.13 preserve the total number of interactions. This is true if an infinite dilution is considered. Considering a finite geometry, a nuclear reactor for instance, this fact is no longer true. Increasing the temperature reduces the interaction probability. This phenomenon is called Doppler effect and it is of major interest for the safety concerns of ASTRID conception.

In APOLLO3, a new modelization of the Doppler-broadening in the resonance domain has been introduced in order to rigorously describe the phenomenon [21]. In addition, the way scattering events are simulated has been improved [22].

Returning to the macroscopic cross section  $\Sigma_{x,i}(\vec{r}, v_n, t)$ , formula 2.11 underlines that, while

the microscopic cross sections are time-independent physical properties (this statement will be re-discussed in 2.4.4), isotope concentrations change in time and space. For the purpose of this work, the time variation of the concentrations is of primary interest. It is important, then, to explain why concentrations vary: some nuclear reactions - principally neutron capture, fission and spallation ones- modify the target nuclei. Operating a nuclear reactor, therefore, means to ensure a neutron balance taking into account changes in the isotope concentrations.

### 2.3 Depletion Calculation

In a nuclear reactor, as previously discussed, isotope concentrations continuously change. This fact modify the composition of the materials. In the fuel, for instance, radiative capture and fission occur. Isotopes transmute and fission products appear. This change continuously modifies the macroscopic cross sections which appear in 2.8.

Steady-state reactor physics does not solve the time dependent Boltzmann equation. Operational requirements are set to exploit the reactor at certain condition; but, to account for concentration evolution, an approximation must be made in order to neglect the time variable dependence. Time is discretized into time steps:  $t_1, t_2, \dots, t_N, \dots$ . At each time step  $t_N$ , the steady-state Boltzmann equation is solved by means of a transport code, both stochastic and deterministic:

$$\vec{\Omega} \cdot \vec{\nabla} \phi(\vec{r}, \vec{\Omega}, v_n, t_N) + \Sigma(\vec{r}, v_n, t_N) \phi(\vec{r}, \vec{\Omega}, v_n, t_N) = Q(\vec{r}, \vec{\Omega}, v_n, t_N) \quad (2.14)$$

The flux distribution and the reaction rates are evaluated at  $t_N$ . These information are used to compute the new concentrations at  $t_{N+1}$ , which provide the new macroscopic cross sections to solve the Boltzmann equation at the new time step. It is possible to observe the scheme in figure 2.4. The time interval  $\Delta t = t_{N+1} - t_N$  must be smaller than the time scale of the flux change, for the approximation to be verified. The flux distribution changes at each time step, but not considerably so that it can be represented by a straight line or a parabola. It is possible, hence, to decouple the concentration evolution and the flux distribution evaluation. For the former, a system of equations must be solved: the Bateman equations. These ones account for concentration variations. For each isotope  $k$ , the variation is equal to the difference between the rates of its production and of its transmutation due to absorption or spontaneous decay. The source term is:

$$S_k(t) = \sum_{j=1}^J \left[ \sum_{g=1}^G Y_{k,j}^g < \sigma_{f,j} \Phi >_g(t) \right] N_j(t) + \sum_{j=1}^K \lambda_{j \rightarrow k}(t) N_j(t) \quad (2.15)$$

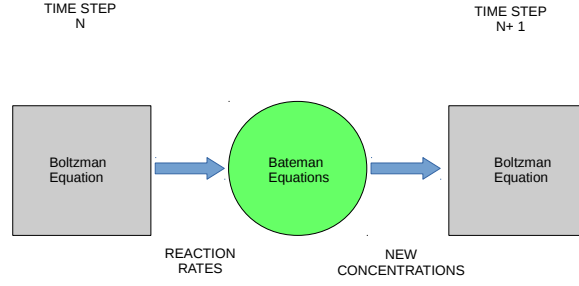


Figure 2.4 Depletion calculation scheme

where:

- $J$  is the number of fissile isotopes
- $K$  is the number of depleting isotopes
- $G$  is the number of fission yield groups
- $\langle \sigma_{f,j} \Phi \rangle_g(t)$  is the volume averaged fission reaction rate of isotope  $j$  integrated over the energy fission yield group  $g$
- $Y_{k,j}^g$  is the fission yield of  $g$  group for the production of isotope  $k$  from fissionable isotope  $j$
- $\lambda_{j \rightarrow k}(t)$  is equal to the radioactive constant  $\lambda_j$  or  $\langle \sigma_{x,j} \Phi \rangle(t)$  reaction rate, integrated over the whole energy domain, for production of isotope  $k$  by  $j$ .

The transmutation term is equal to:

$$\Lambda_k(t)N_k(t) = (\lambda_k + \langle \sigma_{a,k} \Phi \rangle(t)) N_k(t) \quad (2.16)$$

The first order system of  $K$  equations is

$$\frac{dN_k}{dt} + \Lambda_k(t)N_k(t) = S_k(t) \quad (2.17)$$

for all the depleting isotopes  $k=1,\dots,K$ .

Replacing the time dependent reaction rates with the Greek letter  $\tau$ , it is possible to write



the Bateman equations in a matrix form:

$$\frac{d\vec{N}}{dt} = \bar{\bar{A}}(\lambda, \tau(t)) \cdot \vec{N}(t) \quad (2.18)$$

where it is possible to separate in matrix  $\bar{\bar{A}}$  the time independent component depending on the decay constants, which are physical properties of the nuclei, from the reaction rates, which are time dependent and vary with the reactor operating condition. A description of matrix  $\bar{\bar{A}}$  is presented in section 2.5, along with a discussion about the representation of the reaction rate time variation (linear or parabolic). The importance of flux normalization will be discussed in section 2.5.1.

All the fundamental equations, which this work deals with, have been presented at the moment. The chapter, from now on, will focus on the numerical methods used to solve these equations. The first section will discuss the numerical methods and the solvers used for the Boltzmann equation; the second one will concern the numerical methods used to solve the Bateman equations.

## 2.4 Solution of the Boltzmann Equation

### 2.4.1 Different Forms of the Transport Equation

Beside formula 2.14, it is possible to distinguish other forms of the Boltzmann equation. These forms can be used in certain resolution methods of the transport equation. From now on, the neutron velocity  $v_n$  will be replaced with its kinetic energy  $E$  in the formula. Another quantity the neutron energy can be described with is the lethargy  $u = \ln\left(\frac{E_0}{E}\right)$ , where  $E_0$  is the neutron reference energy, usually set to 10 MeV.

#### The Characteristic Form

Defining with the greek letter  $\Gamma$  a characteristic (a straight line with direction  $\vec{\Omega}$ , corresponding to a possible neutron trajectory), it is possible to parametrize the neutron position along this direction: starting from  $\vec{r} \in \Gamma$ , each neutron position in the characteristic is described by  $\vec{r} - s\vec{\Omega}$ . Equation 2.14 can be, consequently, reformulated in its characteristic form:

$$-\frac{d}{ds}\phi(\vec{r} - s\vec{\Omega}, \vec{\Omega}, E, t_N) + \Sigma(\vec{r} - s\vec{\Omega}, E, t_N)\phi(\vec{r} - s\vec{\Omega}, \vec{\Omega}, E, t_N) = Q(\vec{r} - s\vec{\Omega}, \vec{\Omega}, E, t_N) \quad (2.19)$$

## The Integral Form

Integrating the equation 2.19 on an infinite domain, the integral form of the transport equation is obtained:

$$\phi(\vec{r}, \vec{\Omega}, E, t_N) = \int_0^{+\infty} ds e^{-\tau_{opt}(s, E, t_N)} Q(\vec{r} - s\vec{\Omega}, \vec{\Omega}, E, t_N) \quad (2.20)$$

where the optical path  $\tau_{opt}$  is introduced to account for the neutron density attenuation along the characteristic. It is defined as follows:

$$\tau_{opt}(s, E, t_N) = \int_0^s ds' \Sigma(\vec{r} - s'\vec{\Omega}, E, t_N) \quad (2.21)$$

If a finite domain is considered, the integral form becomes:

$$\phi(\vec{r}, \vec{\Omega}, E, t_N) = e^{-\tau_{opt}(b, E, t_N)} \phi(\vec{r}_f, \vec{\Omega}, E, t_N) + \int_0^b ds e^{-\tau_{opt}(s, E, t_N)} Q(\vec{r} - s\vec{\Omega}, \vec{\Omega}, E, t_N) \quad (2.22)$$

where  $\vec{r}_f$  represents the position where the characteristic enters the domain and  $b = |\vec{r} - \vec{r}_f|$ . In order to simplify the notation, from now on, the dependency of the quantities from the time step  $t_N$  won't be explicitly written. Of course, if nothing else is said, this dependency will continue to implicitly exist.

### 2.4.2 Source Density

The source density  $Q(\vec{r}, \vec{\Omega}, E)$  has been previously introduced in order to define the particle balance. It is composed by a fission term, a scattering term and a term accounting the external sources (spontaneous fissions or other reactions):

$$Q(\vec{r}, \vec{\Omega}, E) = Q_{scatt}(\vec{r}, \vec{\Omega}, E) + Q_{fiss}(\vec{r}, \vec{\Omega}, E) + S_{ext}(\vec{r}, \vec{\Omega}, E) \quad (2.23)$$

At nominal condition, the external source term is negligible and it is not taken into account. The scattering neutron source density, on the contrary, is considered. It describes the source of neutrons, which sweep a certain solid angle  $d^2\Omega$  with a certain energy in  $[E, E + dE]$ , produced by a scattering event of incident neutrons in  $d^2\Omega' dE'$  phase space. In order to represent this term, the macroscopic differential scattering cross section  $\Sigma_s(\vec{r}, E \leftarrow E', \vec{\Omega} \leftarrow \vec{\Omega}')$  is introduced. It corresponds to the probability density that an incident neutron in  $d^2\Omega' dE'$  is scattered into the  $d^2\Omega dE$  phase space. In the assumption of isotropic materials:

$$Q_{scatt}(\vec{r}, E, \vec{\Omega}) = \frac{1}{2\pi} \int_{4\pi} d^2\Omega' \int_0^{+\infty} dE' \Sigma_s(\vec{r}, E \leftarrow E', \vec{\Omega} \cdot \vec{\Omega}') \phi(\vec{r}, E', \vec{\Omega}') \quad (2.24)$$

where a Legendre polynomial expansion can be performed on the differential scattering cross section. A description of the Legendre polynomial expansion is beyond the point of this work. Every information can be found in [16]. For the time being, it is worth saying that the Legendre polynomial expansion of the macroscopic scattering cross section is limited to order  $L$  ( $\Sigma_{s,L}(\vec{r}, E \leftarrow E')$ ).  $L = 0$  means isotropic scattering, whereas  $L = 1$  describes linearly anisotropic scattering. In this work, to correctly account for flux gradient,  $L = 3$  is used for the future calculations.

The fission source term, now, can be discussed. Usually, in reactor calculations, it is supposed to be isotropic and it describes the neutrons produced by fission events on the fissile isotopes. Incident neutron energy is represented with  $E'$ , whereas  $E$  describes the secondary neutron energy. Neglecting the dependency of the secondary neutron fission spectrum on the incident neutron energy, the fission source term is written as follows:

$$Q_{fiss}(\vec{r}, E, \vec{\Omega}) = \frac{1}{4\pi} Q_{fiss}(\vec{r}, E) = \frac{1}{4\pi} \sum_{j=1}^J \chi_j(E) \int_0^{+\infty} dE' \nu_j(\vec{r}, E') \Sigma_{f,j}(\vec{r}, E') \phi(\vec{r}, E') \quad (2.25)$$

where

- $J$  is the number of fissile isotopes
- $\Sigma_{f,j}(\vec{r}, E')$  : macroscopic fission cross section of isotope  $j$ ,
- $\nu_j(\vec{r}, E')$  : average secondary neutron number for the fissile isotope  $j$ ,
- $\chi_j(E)$  : energy averaged secondary neutron fission spectrum (normalized to 1),
- $\phi(\vec{r}, E) = \int_{4\pi} d^2\Omega \phi(\vec{r}, E, \vec{\Omega})$  : integrated flux (or scalar flux).

It is important to notice that, because steady-state conditions are considered, no distinction between prompt and delayed neutron is made.

The major part of the actual deterministic codes —APOLLO2 and ECCO are an example— uses 1 energy averaged fission spectrum for transport calculations. Secondary neutron energy-independent fission spectra are averaged using weighting functions which are typical of the reactor applications.

However, in APOLLO3 and in Monte Carlo codes, it is possible to relate the secondary neutron fission spectrum to the incident neutron energy, writing the fission source term in

the following way:

$$Q_{fiss}(\vec{r}, E) = \sum_{j=1}^J \int_0^{+\infty} dE' \nu_j(\vec{r}, E', E) \Sigma_{f,j}(\vec{r}, E', E) \phi(\vec{r}, E') \quad (2.26)$$

This is the most rigorous way to write the fission source term. The numerical methods to treat with this term will be explained in section 2.4.3, after introducing the multigroup approach. The energy discretization of this term will be presented, such as performed in TRIPOLI4 and in APOLLO3.

### Eigenvalue Problem

In most reactor physics applications, an eigenvalue problem must be solved. The external source in the source density is neglected during reactor operations at nominal conditions. This leads to the presence of the neutron flux in each term of the transport equation. Physically, this means that the neutron flux itself is the only cause of the presence of a neutron flux. Because the solution of the steady-state transport equation 2.14 is the aim of transport codes, an equilibrium between the neutrons produced and the ones absorbed or escaping the system must be set, in the calculation domain, to assure steady-state condition. This justifies the introduction of an artificial parameter  $k$  which divides the neutron fission source to adjust the neutronic equilibrium. The source term is consequently written as follows:

$$Q(\vec{r}, \vec{\Omega}, E) = Q_{scatt}(\vec{r}, \vec{\Omega}, E) + \frac{1}{4\pi k} Q_{fiss}(\vec{r}, E) \quad (2.27)$$

The following eigenvalue problem must then be solved:

$$A\phi = \frac{1}{k} F\phi \quad (2.28)$$

where

$$A\phi = \vec{\Omega} \cdot \vec{\nabla} \phi(\vec{r}, \vec{\Omega}, E) + \Sigma(\vec{r}, E) \phi(\vec{r}, \vec{\Omega}, E) - Q_{scatt}(\vec{r}, \vec{\Omega}, E) \quad (2.29)$$

and

$$F\phi = \frac{1}{4\pi} Q_{fiss}(\vec{r}, E) \quad (2.30)$$

The solution of equation 2.28, over a certain geometry domain and with certain boundary conditions, leads to a discrete number of eigenvalue  $k_i$  to which corresponding eigenfunctions  $\phi_i$  are associated.

The eigenfunction  $\phi_0$ , associated to the maximum eigenvalue  $k_0$ , is called fundamental mode. It is the only function among  $\phi_i$  which do not change sign in the geometry domain and it is

representative of the real flux present in the system [16].

The eigenvalue  $k_0$  is called effective multiplication factor  $k_{eff}$  (or infinite multiplication factor  $k_{inf}$ , if leakage are not accounted and infinite geometries are considered). This value can be demonstrated to be real, positive and non degenerate. If it is equal to 1, the system is in steady state condition (criticality is assured). On the contrary, if it is greater than 1, super-critical condition is set and neutron population diverges in time (the fission production is higher than required). Neutron population decreases in time if  $k_{eff} < 1$ . Sub-critical condition is met and the fission production is smaller than required to maintain a steady state neutron balance.

### 2.4.3 Multigroup Approach

The independent variables of the steady state Boltzmann equation are the three components of the space vector  $\vec{r}$ , the energy and the two components of the solid angle  $\vec{\Omega}$ . In order to reduce the number of unknowns, a multigroup approach is used. This approach results in the utilization of energy averaged quantities. Consequently,  $G$  energy groups create a system of  $G$  Boltzmann equations whose properties are energy condensed. The  $G$  transport equations are:

$$\vec{\Omega} \cdot \vec{\nabla} \phi^g(\vec{r}, \vec{\Omega}) + \Sigma^g(\vec{r}) \phi^g(\vec{r}, \vec{\Omega}) = Q^g(\vec{r}, \vec{\Omega}) \quad (2.31)$$

for  $1 \leq g \leq G$ .

Defining the energy boundaries as follows:

$$0 < E_{G+1} < E_G < \dots < E_{g+1} < E_g < \dots < E_1 < +\infty$$

it is possible to introduce the quantities of interest:

$$\phi^g(\vec{r}, \vec{\Omega}) = \int_{E_{g+1}}^{E_g} dE \phi(\vec{r}, E, \vec{\Omega}) \quad (2.32)$$

$$\phi^g(\vec{r}) = \int_{E_{g+1}}^{E_g} dE \phi(\vec{r}, E) = \int_{4\pi} d^2\Omega \phi^g(\vec{r}, \vec{\Omega}) \quad (2.33)$$

$$\Sigma^g(\vec{r}) = \frac{1}{\phi^g(\vec{r})} \int_{E_{g+1}}^{E_g} dE \Sigma(\vec{r}, E) \phi(\vec{r}, E) \quad (2.34)$$

Concerning the fission source density, equation 2.26 can be rewritten. It is possible to consider the fission source as a function of both energy group  $g'$  of the neutron causing the fission and energy group  $g$  of the neutron produced by the fission. For each energy group pair  $g$  and  $g'$ , it is possible to introduce a component of the multigroup fission matrix  $\sigma_{f,j}^{g' \rightarrow g}$ : it represents

the secondary neutron number produced in the energy group  $g$  by an incident neutron in  $g'$  from a single target nucleus of the isotope  $j$ . It incorporates the prompt and delayed fission neutron components obtained with a nuclear data elaboration code as GALILEE [8].

Using the multigroup fission matrix, the fission term becomes:

$$Q_{fiss}^g(\vec{r}) = \sum_{j=1}^J \sum_{g'=1}^{G'} N_j(\vec{r}) \sigma_{f,j}^{g' \rightarrow g} \phi^{g'}(\vec{r}) \quad (2.35)$$

where  $\phi^{g'}(\vec{r})$  is the scalar flux integrated over the energy group  $g'$  (see 2.4.3).

The multigroup fission matrix approach is currently used for Monte Carlo nuclear code as TRIPOLI4 [9]. This approach is far more accurate than the one presented in equation 2.25, but it is not easy to implement in deterministic code. Different iterative procedures have been implemented to better estimate the fission source for APOLLO2 calculations [23, 24]. Nevertheless, for fast neutron system, 4 macro-group secondary neutron fission spectra have been demonstrated to be accurate enough for the fission source representation [24]. APOLLO3 is capable to deal with 4 macro-group spectra. The influence of the number of spectra in depletion calculations will be analyzed in chapter 3.

In table 2.1, it is possible to see the energy boundaries of the macro-groups. Using a number NMG of macro-groups, the fission term becomes:

$$Q_{fiss}^g(\vec{r}) = \sum_{j=1}^J \sum_{mg=1}^{NMG} \chi_{j,mg}^g \sum_{g'=Inf(mg)}^{Sup(mg)} N_j(\vec{r}) \nu_j^{g'}(\vec{r}) \sigma_{f,j}^{g'}(\vec{r}) \phi^{g'}(\vec{r}) \quad (2.36)$$

where

$$\chi_{j,mg}^g = \frac{\sum_{g'=Inf(mg)}^{Sup(mg)} \sigma_{f,j}^{g' \rightarrow g} w^{g'}}{\sum_{g'=Inf(mg)}^{Sup(mg)} \nu_j^{g'} \sigma_{f,j}^{g'} w^{g'}} \quad (2.37)$$

$Inf(mg)$  and  $Sup(mg)$  are respectively the upper and lower boundaries of the macro-group  $mg$ .  $w^{g'}$  is the proper weighting function, integrated over the energy group  $g'$ .

Considering the scattering source term introduced in 2.36, it is possible to write the source

Table 2.1 Energy Boundaries of fission spectrum macro-groups

	Sup(mg)		Inf(mg)
I	20 MeV	-	1.35 MeV
II	1.35 MeV	-	497 keV
III	497 keV	-	183 keV
IV	183 keV	-	10 <sup>-5</sup> eV

density as follows:

$$Q^g(\vec{r}, \vec{\Omega}) = \frac{1}{2\pi} \sum_{g'} \int_{4\pi} d^2\Omega' \Sigma_s^{g' \rightarrow g}(\vec{r}, \vec{\Omega}' \cdot \vec{\Omega}) \phi^{g'}(\vec{r}, \vec{\Omega}') + \frac{1}{4\pi k} Q_{fiss}^g(\vec{r}) \quad (2.38)$$

where

$$\Sigma_s^{g' \rightarrow g}(\vec{r}, \vec{\Omega}' \cdot \vec{\Omega}) = \frac{1}{\phi^{g'}(\vec{r}, \vec{\Omega}')} \int_{E_{g+1}}^{E_g} dE \int_{E_{g'+1}}^{E_{g'}} dE' \Sigma_s(\vec{r}, E' \rightarrow E, \vec{\Omega}' \cdot \vec{\Omega}) \phi(\vec{r}, \vec{\Omega}', E') \quad (2.39)$$

The distinction between lattice step and core one for deterministic nuclear codes has already been introduced in 1.6.1. One of the major difference between these steps is the number of energy groups  $G$  used. For SFR applications, in lattice calculations  $G$  is set to 1968, while it is equal to 33 at core step.

Input cross section libraries, read by APOLLO3, are created with GALILEE [8], performing a condensation of the JEFF3.1.1 evaluated data into 1968 energy groups. In equation 2.34, it is possible to see that a proper flux  $\phi^g$  must be used to conserve the reaction rates. Because the flux  $\phi^g$  is the quantity to be evaluated, a weighting function  $w^g$  proper of fast systems is used to guarantee accurate results in the widest range of applications.

The choice of the number of energy groups is made so that the wider resonances are represented by the group cross sections themselves, while the narrower ones can be treated in narrow resonance approximation in the sub-group method (see 2.4.4) [25]. In the next section, self-shielding will be discussed.

#### 2.4.4 Self-Shielding

The multigroup approach has been previously discussed. Energy averaged quantities are used and, in order to preserve the reaction rates, the flux is used as weighting function. But the flux is the quantity to be evaluated, so, as already discussed, weighting functions  $w^g$  are used. These weighting functions, nevertheless, do not take into account the spatial distribution of the flux. They just represent an energy spectrum. But, in a nuclear reactor, heterogeneities are present and the flux assumes also a spatial distribution. Resonances are more effective in a region where an higher flux  $\phi^g(\vec{r})$  is present.

As a result, a spatial distribution for the microscopic cross sections  $\bar{\sigma}_{x,i,T}(E, \vec{r})$  arises because of resonance condensation into energy groups. In thermal reactor, a phenomenon called rim-effect is present inside the fuel pin. The pin flux distribution is not homogeneous but it presents a peak in the external region and a depression in the internal one. Reaction rates are, then, higher in the outer regions. This phenomenon is absent in fast systems where a flatter flux is present (see appendix A).

A self-shielding method, therefore, creates a microscopic cross section library which is space dependent. To do so, cross section values are interpolated from input libraries with the aid of dilution parameters and the Livolant-Jeanpierre approximation; or they are evaluated by means of a flux calculation with sub-groups. The latter is called sub-group method and will be presented later. For more information, it is possible to consult [16, 17, 26].

Before discussing in detail the sub-group method and its variation by Tone, it is worth reminding that the flux distribution used in the multigroup approach is time dependent. The self-shielding method, then, introduces also a time dependency on the microscopic cross section library  $\bar{\sigma}_{x,i,T}(E, \vec{r}, t_N)$ . The variation of the microscopic cross section library, and its effect on the multiplication factor during the reactor operation, will be studied in 3.1.1, where self-shielding re-iteration will be discussed.

### Sub-Group Method

In the sub-group method, Riemann integrals are replaced with Lebesgue ones. Cross sections are considered the integration variable:

$$I = \frac{1}{\Delta u} \int_{u_g}^{u_{g+1}} F[\sigma(u)] du = \int_{\min_g(\sigma)}^{\max_g(\sigma)} F(\sigma) \pi(\sigma) d\sigma \quad (2.40)$$

where  $u$  is the lethargy defined previously and  $\pi(\sigma)$  is  $\sigma$  probability density.

Integral 2.40 is solved using a quadrature formula. The probability tables produced by CALENDF [19] contains a number  $K$  of couples  $\{\sigma_k, \omega_k\}$  for each group  $g$ , with  $\sum_{k=1}^K \omega_k = 1$ . Each  $k$  is a sub-group in the energy group  $g$ . The probability density is written in the following way:

$$\pi(\sigma) = \sum_k \delta(\sigma - \sigma_k) \omega_k \quad (2.41)$$

so that

$$I = \sum_k F(\sigma_k) \omega_k \quad (2.42)$$

Resonant isotopes are treated one at a time and, for fast systems, no significant correlation occurs in mixtures. The resonant isotope is defined with “\*” superscript, whereas “+” identifies the other non resonant isotopes. The subscript “ $i$ ”, meanwhile, identifies quantities integrated over the region  $V_i$ . For region  $i$ , the total cross section is equal to:

$$\Sigma_i(u) = \Sigma_i^+(u) + N_i^* \sigma^*(u) \quad (2.43)$$



and the source term is decomposed in a fission, (n,xn), an inelastic and an elastic scattering contribution:

$$Q_i(u) = Q_{f,i}(u) + Q_{(n,xn),i}(u) + Q_{inel,i}(u) + Q_{el,i}(u) \quad (2.44)$$

The contribution of the non resonant isotopes is highlighted in the elastic scattering term:

$$Q_{el,i}(u) = Q_{el,i}^+(u) + N_i^* r^* (\phi_i(u)) \quad (2.45)$$

where  $r^* (\phi_i(u))$  is the slowing-down operator term defined as follows:

$$r^* (\phi_i(u)) = \int_0^{+\infty} du' \int_{V_i} d^3r \sigma_s^*(\vec{r}, u \leftarrow u') \phi(\vec{r}, u') \quad (2.46)$$

The ECCO sub-group method and the one used for APOLLO3 calculations imply the narrow resonances hypothesis. Resonances, then, are considered narrow and isolated. A collision in  $u'$  is considered out of the resonance zone [24, 26]. This means that the flux distribution in  $u'$  is not affected by resonances. A constant distribution of the flux  $\phi(\vec{r}, u')$  can be consequently supposed. The slowing-down operator is rewritten as a constant:

$$r^* (\phi_i(u)) = \sigma_p^* \quad (2.47)$$

The narrow resonance assumption is valid in the energy region exploited by fast neutron systems, if a proper energy mesh is used.

The multigroup transport equation becomes for region  $i$ :

$$\begin{aligned} \vec{\Omega} \cdot \vec{\nabla} \phi_i^g(\vec{\Omega}, u) + (\Sigma_i^{g+} + N_i^* \sigma^*(u)) \phi_i^g(\vec{\Omega}, u) = \\ = \frac{1}{4\pi} \left( Q_{f,i}^g(u) + Q_{(n,xn),i}^g(u) + Q_{inel,i}^g(u) + Q_{el,i}^{g+}(u) + N_i^* \sigma_p^* \right) \end{aligned} \quad (2.48)$$

with  $u \in [u_g, u_{g+1}]$ .

Applying the quadrature formula and considering the neutron balance satisfied for each sub-group  $k$ , the sub-group transport equation to be solved becomes:

$$\begin{aligned} \vec{\Omega} \cdot \vec{\nabla} \phi_{i,k}^g(\vec{\Omega}) + (\Sigma_i^{g+} + N_i^* \sigma_k^*) \phi_{i,k}^g(\vec{\Omega}) = \\ = \frac{1}{4\pi} \left( Q_{f,i}^g(u) + Q_{(n,xn),i}^g(u) + Q_{inel,i}^g(u) + Q_{el,i}^{g+}(u) + \frac{1}{\omega_k} N_i^* \sigma_p^* \right) \end{aligned} \quad (2.49)$$

for  $1 < k < K$ .

Applying the collision probability method (see 2.4.6), the  $K$  sub-group transport equations are solved for each group  $g$ . A fundamental hypothesis is made: the neutron source is

supposed to be decorrelated from resonant cross sections. This is true if resonances are numerous and statistical distributed or if the multigroup energy mesh is fine [26].

For the resonant isotope, the cross section for  $x$  reaction can be now evaluated in region  $i$ :

$$\sigma_{x,i}^{*,g} = \frac{\int_g \sigma_x^*(u) \phi_i(u) du}{\int_g \phi_i(u) du} = \frac{\sum_{k=1}^K \sum_j \omega_k \sigma_{x,k}^* p_{ij,k} Q_j^g}{\sum_{k=1}^K \sum_j \omega_k p_{ij,k} Q_j^g} \quad (2.50)$$

where  $p_{ij,k}$  is the reduced collision probability term of the sub-group  $k$ . This term is evaluated by means of the probability table  $p_{ij,k} = p_{ij}(\sigma_k)$ . An iterative procedure, on the contrary, must be set for the flux calculation, required by the sub-group self-shielding. The  $Q_j^g$  source term is updated at each power iteration.

### Tone's Method

This method has been implemented by Tone in 1975 [27]. The time saved is of the order of a factor 30 with respect to the previous method. This occurs mainly because only 1  $P_{ij}$  per group is calculated and not  $K$  sub-group  $p_{ij,k}$ . The method is applied before, separately. The collision probability method is applied also in this case. With respect to the ordinary CPM (see section 2.4.6), a major assumption is made concerning the neutron flux in region  $j$  coming from region  $i$ :  $\phi_{ij}(u)$  is proportional to the group averaged flux  $\phi_{ij}^g$  by means of a coefficient  $\alpha_j(u)$  which depends only on region  $j$ :

$$\phi_{ij}(u) = \frac{V_i P_{ij}(u)}{V_j \Sigma_j(u)} Q_i(u) \approx \alpha_j(u) \phi_{ij}^g \quad (2.51)$$

where  $u \in [u_g, u_{g+1}]$  and  $P_{ij}(u)$  is the collision probability term.

The total flux over the region  $j$  is  $\phi_j(u) = \sum_i \phi_{ij}(u)$ . After doing few manipulations and distinguishing the resonant isotope, it is possible to explicit  $\phi_j(u)$ :

$$\phi_j(u) = \frac{\sum_i V_i Q_i^g P_{ij}^g}{\sum_i V_i N_i^* (\sigma^*(u) + \sigma_{0,i}^{*,g}) P_{ij}^g} ; \quad u \in [u_g, u_{g+1}] \quad (2.52)$$

where the dilution cross section is identified (macroscopic cross sections of the  $n$  nuclei different from the resonant one divided by the resonant isotope concentration):

$$\sigma_{0,i}^{*,g} = \sum_{n \neq m} \frac{N_i^n \sigma_i^{n,g}}{N_i^*} \quad (2.53)$$

and  $P_{ij}^g = \int_g P_{ij}(u) du$ .

For the resonant isotope, the cross section for reaction  $x$  can be now evaluated in region  $i$ :

$$\sigma_{x,i}^{*,g} = \frac{\int_g \sigma_x^*(u) \phi_i(u) du}{\int_g \phi_i(u) du} \quad (2.54)$$

with

$$\int_g \sigma_x^*(u) \phi_i(u) du = \int_g \frac{\sigma_x^*(u) du}{\sum_i V_i N_i^* (\sigma^*(u) + \sigma_{0,i}^{*,g}) P_{ij}^g} = \sum_{k=1}^K \frac{\omega_k \sigma_{x,k}^*}{\sum_i V_i N_i^* (\sigma_{x,k}^* + \sigma_{0,i}^{*,g}) P_{ij}^g} \quad (2.55)$$

and

$$\int_g \phi_i(u) du = \int_g \frac{du}{\sum_i V_i N_i^* (\sigma^*(u) + \sigma_{0,i}^{*,g}) P_{ij}^g} = \sum_{k=1}^K \frac{\omega_k}{\sum_i V_i N_i^* (\sigma_{x,k}^* + \sigma_{0,i}^{*,g}) P_{ij}^g} \quad (2.56)$$

Tone's method does not require a flux calculation. The source term does not appear in formula 2.54. However, the group averaged collision probabilities  $P_{ij}^g$  are evaluated by means of an iterative procedure. In fact, macroscopic cross sections  $\Sigma_{x,i}^{*,g}$  are required to calculate the collision probabilities, but the collision probabilities themselves are required in equation 2.54.

It is important to notice that the fundamental hypothesis of the Tone method is related, in a sort of way, to the assumption that the region, where the nuclide is located, is spatially isolated. It is “distant” or slightly sensitive to the presence of other materials containing the same isotope. This assumption is reasonable in CFV core configuration because fuel pins are separated and no major spatial self-shielding effect is observed.

In section 3.1.1, the validity of the application of the Tone method during the evolution will be discussed, comparing this method with the sub-group one previously introduced.

#### 2.4.5 General Resolution Algorithm

After a self-shielding method is applied, the multigroup macroscopic cross section library can be created in order to perform the flux evaluation in a number  $G$  of energy groups. Equation 2.28 must be solved in the multigroup approach. A system of  $G$  equations is set and, although numerous numerical methods have been implemented to solve it (see 2.4.6 and 2.4.7), the general iteration procedure is described below. It involves an inverse power method: a first initialization of the flux vector  $\vec{\phi}_0$  is made and an initial value of the multiplication factor, usually  $k_0 = 1$ , is set. It is the beginning of an *outer iteration* (index  $e$ ).

Every energy group equation is separately resolved: internal iterations are made (index

*i*). Energy group equation is solved following the neutron slowing-down (from 1 to  $G$ ). The diffusion source term  $Q_{scatt}^g$  is evaluated and, inverting the  $A$  operator of the group  $g$  (identified with  $A^g$ ), it is possible to write:

$$\phi_{i+1}^g = \frac{1}{k_e} (A^g)^{-1} F \phi_i \quad (2.57)$$

A Gauss-Seidel fixed point iteration method is usually implemented for equation 2.57 [28]. The scattering source term is updated every time  $\phi^g$  is converged before starting evaluating  $\phi^{g+1}$ . If neutrons are supposed to up-scatter, up-scattering iteration are required. Once that all the energy spectrum is treated, the multiplication factor, and consequently the fission source, is updated and a new outer iteration starts, until convergence is reached:

$$k_{e+1} = k_e \frac{F \phi_{e+1}}{F \phi_e} \quad (2.58)$$

The inverse power method converges to the eigenvector associated to the highest eigenvalue, i.e. the fundamental mode solution  $k_0, \phi_0$ .

The difficult part is to explicitly write equation 2.57 with  $(A^g)^{-1}$  term. In fact, the solution of the transport equation becomes the solution of mono-energetic fixed source equations.

Before discussing the actual numerical method used to solve the transport equation, another important aspect of the problem modelization is introduced: the boundary conditions.

## Boundary Conditions

Different boundary conditions can be applied to close the system of equations:

- **Albedo boundary conditions:**

In the neutron boundary surface  $S$ , with outgoing normal vector  $\vec{N}$ , in position  $\vec{r}_b \in S$ , the incoming flux with direction  $\vec{\Omega}'$  is proportional to the outgoing flux  $\phi^g(\vec{r}_b, \vec{\Omega})$  by a factor  $\beta$ :

$$\phi^g(\vec{r}_b, \vec{\Omega}) = \beta \phi^g(\vec{r}_b, \vec{\Omega}') \quad ; \quad \beta \in [0, 1] \quad (2.59)$$

with

$$\vec{\Omega} = \vec{\Omega}' - 2|\vec{N} \cdot \vec{\Omega}'| \vec{N} \quad (2.60)$$

If  $\beta = 0$ , a vacuum boundary condition is set. If it is equal to 1, a specular reflective boundary condition is set.

- **Periodic boundary conditions:**

In a periodic lattice grid, this boundary condition corresponds to a case where the flux

in a surface  $S$  is equal to another in a surface  $S'$ , parallel to the first one:

$$\phi^g(\vec{r}_b, \vec{\Omega}) = \phi^g(\vec{r}_b + \Delta r, \vec{\Omega}) \quad (2.61)$$

where  $\Delta r$  is the lattice pitch.

- **White boundary conditions:**

If an incident neutron strikes the boundary surface  $S$ , it is reintroduced with a reflective condition in the volume, following an isotropic angular distribution.

### 2.4.6 TDT Solver

Numerical methods to solve the multigroup transport equation will be presented in this section and in the following one. Only the methods actually used in this work will be treated. For further information, on the methods exposed and on the ones not discussed, it is possible to consult ad hoc manuals [16, 17, 28].

All the methods discussed are present in APOLLO3 code. They are written mainly in C++ and FORTRAN 90, incorporating and extending the capabilities of previous codes: APOLLO2, CRONOS2 and ERANOS. For lattice calculations, i.e. calculations with a fine energy mesh and small geometries, IDT and TDT solvers are provided. They implement respectively short and long characteristic methods [29].

However, only the TDT solver will be discussed. In fact, it is the solver that has been used to perform the lattice calculations presented later in the work. In TDT, the solution of the transport equation can be obtained in two ways: the Collision Probability Method (CPM) and the Method of Characteristics (MOC).

### CPM

The CPM solves the integral form of the transport equation (formulas 2.20 and 2.22). As it can be noticed, this form is nothing else but an integration of the transport equation along a certain track. The track follows a particular direction  $\vec{\Omega}$  and the exponential term is a damping factor. Equation 2.20 can be integrated over all the solid angle. Supposing the source term to be isotropic, the integrated flux is the following:

$$\phi^g(\vec{r}) = \frac{1}{4\pi} \int_{4\pi} d^2\Omega \int_0^\infty e^{-\tau_{opt}(s)^g} Q^g(\vec{r} - s\vec{\Omega}) ds \quad (2.62)$$

The isotropy of the source is a limit of this method that can be partly overcome with a “transport correction”. This correction modifies the total cross section  $\Sigma$  and the order 0

expansion of the scattering cross section  $\Sigma_{s0}$  to account for anisotropic effect.

The total reaction rate over the region defined by the volume  $V_j$  can now be evaluated:

$$\int_{V_j} \Sigma^g(\vec{r}) \phi^g(\vec{r}) d^3r = \frac{1}{4\pi} \int_{V_j} \Sigma^g(\vec{r}) d^3r \int_{4\pi} d^2\Omega \int_0^\infty e^{-\tau_{opt}(s)^g} Q^g(\vec{r} - s\vec{\Omega}) ds$$

$$V_j \Sigma_j^g \phi_j^g = \frac{1}{4\pi} \int_{V_j} \Sigma^g(\vec{r}) d^3r \int_{4\pi} d^2\Omega \int_0^\infty e^{-\tau_{opt}(s)^g} Q^g(\vec{r} - s\vec{\Omega}) ds$$

with

$$\phi_j^g = \frac{1}{V_j} \int_{V_j} \phi^g(\vec{r}) d^3r$$

$$\Sigma_j^g = \frac{1}{V_j \phi_j^g} \int_{V_j} \Sigma^g(\vec{r}) \phi^g(\vec{r}) d^3r$$

A new, more comfortable, variable can be introduced defined as follows  $\vec{r}' = \vec{r} - s\vec{\Omega}$ . Its differential is equal to  $d^3r' = s^2 d^2\Omega ds$ . Then the source term is integrated over all the region  $i$  that appears in the lattice (that are infinite in this case, that's why the volume is defined with the notation  $V_i^\infty$ ). In order to simplify the previous equations the following quantity is defined:

$$Q_i^g = \frac{\int_{V_i^\infty} Q^g(\vec{r}') s^{-2} e^{\tau_{opt}(s)^g} d^3r'}{\int_{V_i^\infty} s^{-2} e^{\tau_{opt}(s)^g} d^3r'}$$

and finally the following expression can be written:

$$V_j \Sigma_j^g \phi_j^g = \sum_i \left[ Q_i^g \frac{1}{4\pi} \int_{V_j} d^3r \Sigma^g(\vec{r}) \int_{V_i^\infty} d^3r' \frac{e^{-\tau_{opt}(s)^g}}{s^2} \right] \quad (2.63)$$

where the summation over all the region  $i$  composing the unit cells in the lattice is made.

Equation (2.63) is further manipulated. The following quantity is introduced

$$P_{ij}^g = \frac{1}{4\pi V_i} \int_{V_j} d^3r \Sigma^g(\vec{r}) \int_{V_i^\infty} d^3r' \frac{e^{-\tau_{opt}(s)^g}}{s^2} \quad (2.64)$$

that expresses the probability for a neutron born in whatever region  $i$  to interact in the particular region  $j$  considered. Actually, using the term 'born' both the meaning of fission born and scattered born is taken into account.

In case of constant cross section in region  $j$ ,  $\Sigma_j^g$ , it can be written

$$p_{ij}^g = \frac{P_{ij}^g}{\Sigma_j^g} = \frac{1}{4\pi V_i} \int_{V_j} d^3r \int_{V_i^\infty} d^3r' \frac{e^{-\tau_{opt}(s)^g}}{s^2} \quad (2.65)$$

$p_{ij}^g$  are the coefficients composing the reduced collision probability matrix that is aimed to be evaluated in this section.

Returning to equation (2.63), the compact notation is

$$V_j \Sigma_j^g \phi_j^g = \sum_i Q_i^g V_i P_{ij}^g \quad (2.66)$$

Two properties must be introduced: the reciprocity and the conservation. The first is mathematically defined as follows

$$p_{ij}^g V_i = p_{ji}^g V_j \quad (2.67)$$

which means that the product between the reduced probability and the volume of the region where the neutron is born remains the same if the neutron is born in one of the regions  $i$  and reacts in region  $j$  or vice versa.

The second property is the conservation one. It claims that in an infinite lattice all the neutron born somewhere in a region  $i$  must necessarily react somewhere in a region  $j$ :

$$\sum_j p_{ij}^g \Sigma_j^g = 1, \forall i \quad (2.68)$$

Equation (2.66) can finally get its last formulation, applying the previous properties:

$$\phi_i^g = \sum_j Q_j^g p_{ji}^g \quad (2.69)$$

Now a system made of  $I$  equations is built, where  $I$  is the number of regions in the unit cell composing the lattice. Solving it means having the value of the flux in the different regions. To get the fluxes  $\phi_i^g$  a tracking procedure must be implemented.

It is possible to divide a major geometry in a certain number of sub-geometries. The CPM method is applied independently on these geometries. Then, they can be coupled by means of escape and transmission probabilities. This method is called Interface Current (IC).

## MOC

The method of characteristics is now synthetically introduced. For further information concerning the tracking procedure, the boundary conditions and the acceleration techniques, it is possible to consult Le Tellier [30]. The notation used to introduce the method also derives from his work.

Before starting to present the equations involved, it is important to underline the advantages that explain why this method is the preferred one for lattice calculations. With respect to

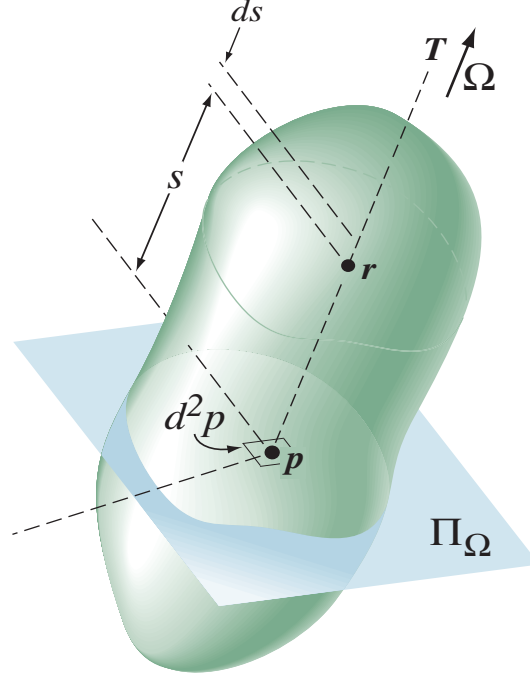


Figure 2.5 MOC integration formalism

CPM, it allows the treatment of anisotropic source and it does not produce full matrix of the order of number of regions. This leads to the use of a more refined tracking mesh and to more accurate results.

In this method, the tracking procedure is of major importance. In figure 2.5, it is possible to visualize its role. A neutron in  $\vec{r}$ , with a certain direction  $\vec{\Omega}$ , is projected on the trajectory defined by  $\vec{T}$  at the point defined by the line variable  $s$ . Neutron flux variables become  $(s, \vec{T})$ . This parametrization of the space in tracking lines provides, as a consequence, a discretization of the angular directions and of the characteristic density on the plane  $\Pi_\Omega$ . In addition, a subdivision in  $K$  segments occurs where a tracking line crosses a calculation region. For each segment  $k$ , equation 2.19 can be integrated over the sub-domain of length  $L_k = \int_{s_k}^{s_{k+1}} ds$ :

$$\phi^g(s_{k+1}, \vec{T}) - \phi^g(s_k, \vec{T}) + \int_{s_k}^{s_{k+1}} ds \Sigma^g(s, \vec{p}) \phi^g(s, \vec{T}) = \int_{s_k}^{s_{k+1}} ds Q^g(s, \vec{T}) \quad (2.70)$$

Equation 2.70 is nothing else than a balance in the sub-domain  $k$  between the outgoing and incoming flux, the collision and the source term.

Because of memory and time calculation matters, the Step Characteristic (SC) scheme is currently used. This scheme is based on the assumption that the source term and cross sections are constant inside each sub-domain  $k$ :  $\Sigma^g(s, \vec{p}) = \Sigma_k^g(\vec{p})$  and  $Q^g(s, \vec{T}) = Q_k^g(\vec{\Omega})$ . Other schemes, which assume a polynomial variation of the two terms, can eventually be



used.

As a consequence of the SC scheme, equation 2.19 can be analytically integrated. The transmission and the balance equations are respectively presented:

$$\phi_{k+1}^g(\vec{T}) = \phi^g(s_{k+1}, \vec{T}) = \phi_k^g(\vec{T})e^{-\tau_{k,opt}^g} + Q_k^g(\vec{\Omega})\frac{1 - e^{-\tau_{k,opt}^g}}{\Sigma_k^g(\vec{p})} \quad (2.71)$$

$$L_k \bar{\phi}_k(\vec{T}) = \int_{s_k}^{s_{k+1}} ds \phi(s, \vec{T}) = \phi_k(\vec{T})\frac{1 - e^{-\tau_{k,opt}^g}}{\Sigma_k^g(\vec{p})} + Q_k^g(\vec{\Omega})\frac{L_k}{\Sigma_k^g(\vec{p})} \left(1 - \frac{1 - e^{-\tau_{k,opt}^g}}{\tau_{k,opt}^g}\right) \quad (2.72)$$

with  $\tau_{k,opt}^g = \int_{s_k}^{s_{k+1}} ds \Sigma_k^g(\vec{p}) = L_k \Sigma_k^g(\vec{p})$ .

Sweeping all the tracking lines over all the sub-domains, from 1 to  $K$ , it is possible to evaluate the flux distribution. Because of the tracking parametrization, it is possible to reconstruct the outgoing flux from a surface  $S_\alpha$ , with outgoing normal vector  $\vec{N}_\alpha^{out}$ , integrating all over the tracking lines concerned:

$$J_\alpha^{g,out} = \int_{S_\alpha} d^2 r_b \int_{\vec{\Omega} \cdot \vec{N}_\alpha^{out} > 0} d^2 \Omega (\vec{\Omega} \cdot \vec{N}_\alpha^{out}) \phi^g(\vec{r}_b, \vec{\Omega}) \stackrel{MOC}{=} \int_\Upsilon d^4 T \chi_\alpha(\vec{r}_{k+1}) \phi(s_{k+1}, \vec{T}) \quad (2.73)$$

where  $\vec{r}_b$  describes all the position vectors which lie on the surface  $S_\alpha$  and  $\chi_\alpha(\vec{r}_{k+1})$  is the characteristic function. This function describes  $S_\alpha$  with the tracking parametrization of the space. The subscript  $k+1$  underlines the fact that the outgoing boundary of the sub-domain  $K$  is considered for the concerned tracking lines.

In conclusion, it is important to say that, in order to reduce calculation time, the flux must be correctly initialized and accelerated. Numerous acceleration techniques are implemented in TDT solver [31, 32].

#### 2.4.7 MINARET Solver

For core calculations, APOLLO3 presents three different solvers: MINOS, MINARET and PASTIS. In this work, MINARET solver is the only one that will be used. This solver allows performing 2D/3D transport calculations using the Simplified Spherical Harmonics method (SPn) or the Discrete Ordinates method (Sn) [29]. The latter will be used for core calculations in 33 energy groups. This solver will be used for the depletion models that will be implemented.

## Sn

In Sn method, the transport equation is solved for a discrete number of angular directions  $\vec{\Omega}_n$ . A quadrature formula is applied for the angular integration. The unit sphere is decomposed into areas of weight  $w_n$ . As a consequence, the scalar flux becomes:

$$\phi^g(\vec{r}) = \int_{4\pi} d^2\Omega \phi^g(\vec{r}, \vec{\Omega}) \approx \sum_n w_n \phi^g(\vec{r}, \vec{\Omega}_n) \quad (2.74)$$

The number of angles  $N$ , the unit sphere is discretized into, is an even number. The choice of the angular directions is important and subjected to symmetry constraint. The aim is the conservation of the maximum number of moments. This allows to correctly represent the source term and its heterogeneities, reducing the ray-effect [16].

For a particular direction  $\vec{\Omega}_n$ , the differential form of the Boltzmann equation is solved:

$$\vec{\Omega}_n \cdot \vec{\nabla} \phi^g(\vec{r}, \vec{\Omega}_n) + \Sigma^g(\vec{r}) \phi^g(\vec{r}, \vec{\Omega}_n) = Q^g(\vec{r}, \vec{\Omega}_n) \quad (2.75)$$

In MINARET, the previous equation is solved with a Discontinuous Galerkin Finite Element Method (DGFEM). A spatial mesh is introduced to discretize the 2D/3D geometry. This mesh is usually triangular (or prismatic by extrusion) [33]. In each element  $V_\alpha$ , equation 2.75 is integrated after projecting it on a basis function  $\psi(\vec{r})$ . Integrating by part and applying the divergence theorem, the following equation is obtained:

$$\begin{aligned} \int_{V_\alpha} d^3r [\Sigma^g(\vec{r}) \phi(\vec{r}, \vec{\Omega}_n) - \phi^g(\vec{r}, \vec{\Omega}_n) \vec{\Omega}_n \cdot \vec{\nabla}] \psi(\vec{r}) = \\ = - \int_{S_\alpha} d^2r_b \vec{\Omega}_n \cdot \vec{N}_\alpha^{out} \phi^g(\vec{r}_b, \vec{\Omega}_n) \psi(\vec{r}_b) + \int_{V_\alpha} d^3r Q^g(\vec{r}, \vec{\Omega}_n) \psi(\vec{r}) \end{aligned} \quad (2.76)$$

where  $S_\alpha$  is the surface of the element,  $\vec{N}_\alpha^{out}$  is its outgoing normal vector and  $\vec{r}_b$  identifies the position vectors on the surface  $S_\alpha$ . The basis function  $\psi(\vec{r})$  is a polynomial. Its degree can be zero ( $P_0$ ), one ( $P_1$ ) or two ( $P_2$ ).

This method works by propagating the flux evaluation as a wave front. External elements are the starting point, then neutron directions are followed. Equation 2.76 is then solved for each element, assuring the integral neutron balance in  $V_\alpha$ . An estimation of the flux inside the volume is required. Therefore, the flux variation in the volume is expanded on the basis function  $\psi(\vec{r})$  (Galerkin). As with every finite element method, it is important to correctly interface each element to the other, using the flux coming from the first as the incoming of the second.

In order to assure the convergence, preconditioning techniques must be implemented. The

Diffusion Synthetic Acceleration (DSA) is used in MINARET. After each internal iteration, an error estimation is done using the diffusion operator or a transport one with less angular directions. This accelerates the external iterations. But, because the same discretization of the variables is not accomplished, instability problems could arise. They are eliminated by introducing a stabilization parameter  $\alpha$  [33, 34].

In order to reduce the calculation time, parallelization techniques are implemented. A first parallelization technique is the one which concerns the angular directions, that are treated independently and then coupled. A second technique lies on a domain decomposition method (DDM): the spatial mesh is divided into macro-domains. The macro-domains are constituted by more elements where the flux is independently evaluated. They are then interfaced to assure the consistency of the flux evaluation in the whole geometry [35].

#### 2.4.8 Homogenization and Condensation

The lattice step provides flux evaluations on reduced reference geometries with fine energy meshes. These fluxes are then used as weighting functions to average the cross sections over the space (homogenization) and energy (condensation) domain. Because more operational conditions are studied at lattice step, multi-parametrized cross section libraries are created to be used for core calculations. If depletion calculations are made, cross sections are usually parametrized also in burn-up.

##### Space Homogenization

The scalar flux is used to homogenize the cross sections over the volume:

$$\Sigma^g = \frac{\int_V d^3r \Sigma^g(\vec{r}) \phi^g(\vec{r})}{\int_V d^3r \phi^g(\vec{r})} \quad (2.77)$$

The flux-volume homogenization allows the preservation of reaction rates and is applied to the homogenization of fission and differential cross sections. In this work, formula 2.77 is the only one used to homogenize the cross sections.

##### Energy Condensation

The input cross section library is further condensed from  $G$  to  $H$  energy groups. Considering all the energy groups  $g$  which are contained in the macro-group  $h$ , the condensation is done

in the following way:

$$\Sigma^h(\vec{r}) = \frac{\sum_{g \in h} \Sigma^g(\vec{r}) \phi^g(\vec{r})}{\sum_{g \in h} \phi^g(\vec{r})} \quad (2.78)$$

Differential scattering cross sections are also condensed in this way:

$$\Sigma_s^{h' \rightarrow h}(\vec{r}) = \frac{\sum_{g' \in h'} \sum_{g \in h} \Sigma_s^{g' \rightarrow g}(\vec{r}) \phi^{g'}(\vec{r})}{\sum_{g' \in h'} \phi^{g'}(\vec{r})} \quad (2.79)$$

#### 2.4.9 Leakage Model

Lattice calculations are usually performed on reference cell geometries with reflective or periodic boundary conditions. This allows to simulate an infinite lattice grid (fundamental mode). Of course, the flux deriving from these calculations is not representative of the actual flux present in a finite reactor. The presence of a leakage term can modify the flux spectrum and, as a consequence, the cross sections used at core step. Therefore, in order to better represent the flux distribution cross sections are condensed with, a leakage model is introduced. Because no information on the real core geometry and operation conditions is assumed, the best approximation is to suppose the system to be in steady-state condition (i.e.  $k_{eff} = 1$ ). In  $B_n$  models, a buckling parameter  $B^2$  is introduced to represent the curvature of the flux throughout the grid, which is implicitly reduced to finite dimension.  $B^2$  is adjusted so that a critical medium is considered.

In this work, the homogeneous  $B_1$  leakage model will be applied. Few words, then, are spent on this model in appendix B. For additional information, it is possible to consult Hébert [16] or Faure's master thesis [36].

#### 2.4.10 Stochastic approach and Monte Carlo method

In the previous sections, the great number of approximations deterministic codes are subjected to have been introduced. This number can be reduced by replacing the deterministic solution of equation 2.14 by a stochastic approach based on Monte-Carlo simulation of the neutron-transport process. However this reduction is reached by means of an increase calculation effort.

In this approach, calculation geometry is first tracked as in MOC and CPM. This is done not to implement a numerical method, but to create a possible neutron path. Neutrons, in fact, are directly simulated from their first appearance in the geometry to the time they disappear, as they undergo absorption reactions or escape the geometry. For a single neutron, each collision and flight direction is associated to a number sampled from a random number generator.

Random number generators are very important. Each aspect of the neutron lives is sampled from them, so that Monte Carlo codes are based on random number sequences. These sequences are created with numbers  $r_i \in [0, 1]$ . These values are then projected on the probability distribution to represent. Unfortunately, it is not possible to create pure random numbers with a numerical algorithm. That's why pseudo-random sequences are used. In TRIPOLI4, they are created using a linear congruential algorithm [9, 37].

Neutron lives are then randomly simulated with a *random walk* algorithm. Neutrons are spatially (position, flight direction) and energy located and a statistical weight  $w_i$  is associated to each one of them. The energy variable can be treated continuously or using a multigroup approach (multigroup Monte Carlo).

Statistical instruments are then used to process the information deriving from the collection of the neutron simulations. Neutron flux and other quantities are evaluated, associating to them a statistical uncertainty. These uncertainties can be reduced if more neutrons are considered [16].

In criticality calculations, neutron histories are divided into cycles. A cycle is called *batch* and consists in a certain number  $N$  of neutrons. This number allows to estimate the fission neutron distribution. Dividing the secondary fission neutron number by  $N$ , it is possible to estimate the multiplication factor  $k_{eff}$  at each batch. The particles of the successive batch are then distributed following the evaluated fission source. At the end of the simulation, in order to get a converged fission source, the first batches are discarded.

It is important to note that Monte Carlo methods lie on a statistical estimation of the desired quantities. The reaction rate formula is reminded for a reaction  $x$  and an isotope  $iso$ :

$$\tau_{x,V,iso}^{\Delta E} = \int_V d^3r \int_{\Delta E} dE \Sigma_{x,iso}(\vec{r}, E) \phi(\vec{r}, E) \quad (2.80)$$

where  $\Delta E$  is the energy domain considered and  $V$  the volume.

Three different estimator can be introduced:

- **Analog estimator:** This estimator is directly related to the simulation process. The actual collisions are summed during the random walk, considering the weight  $w_i$  of the particle:

$$(\tau_{x,V,iso}^{\Delta E})_{analog} = \sum_{i=1}^I w_i \quad (2.81)$$

where  $I$  is the total number of scored values. Only  $x$  reaction with the isotope  $iso$  in  $V$  with energy in  $\Delta E$  are scored.

- **Collision estimator:** The summation is multiplied by the fractional reaction proba-

bilities:

$$(\tau_{x,V,iso}^{\Delta E})_{collision} = \sum_{i=1}^I w_i \frac{\Sigma_{x,iso,k}^g}{\Sigma_k^g} \quad (2.82)$$

with  $g \in \Delta E$  and  $k \in V$ . This estimator is more efficient than the analog one because scores are recorded even if reaction  $x$  does not occur.

- **Track-length estimator:** The scalar flux is equal to the total length travelled by the neutrons present in one cubic centimetre volume in one second. This definition is used to sum over the considered volume the track-length  $\Delta L_i$  of each particle:

$$F = \sum_{i=1}^{I_V} w_i \Delta L_i \quad (2.83)$$

where  $I_V$  is the number of particles crossing  $V$ . Starting from the flux estimation, the reaction rate is:

$$(\tau_{x,V,iso}^{\Delta E})_{track-length} = \sum_{i=1}^{I_V} w_i \Sigma_{x,iso,k}^g \Delta L_i \quad (2.84)$$

If the number of neutron histories tends to infinite, the three estimators converge to the same value.

## 2.5 Solution of the Bateman Equations

The matrix form of the Bateman equations was presented in 2.18. It is here re-proposed.

The system to be solved is:

$$\begin{cases} \frac{d\vec{N}}{dt} = \bar{\bar{A}}(\lambda, \tau(t)) \cdot \vec{N}(t) \\ \vec{N}(0) = \vec{N}_0 \end{cases} \quad (2.85)$$

where  $\vec{N}_0$  is the concentration vector at time zero.

The  $A_{ij}$  elements of the evolution matrix  $\bar{\bar{A}}$  are decomposed in the sum of a constant and a time-dependent term:

- $(A_{ij})_{j \neq i} = \lambda_{ij} + \tau_{ij}(t)$ : non diagonal elements corresponding to the formation of a nucleus  $i$  from  $j$ .  $\lambda_{ij}$  is the decay constant of nucleus  $j$  towards  $i$  and  $(\tau_{ij}(t))_{j \neq i} = \int_0^{+\infty} dE \sigma_{ij}(t, E) \phi(t, E)$  is the formation by neutron reaction of nucleus  $i$  from  $j$
- $A_{ii} = -(\lambda_i + \tau_i(t))$ : diagonal elements corresponding to the disintegration of nucleus  $i$ .  $\lambda_i$  is the decay constant of nucleus  $i$  and  $\tau_i(t) = \int_0^{+\infty} dE \sigma_i(t, E) \phi(t, E)$  its disintegration rate by neutron reaction.

Before presenting the numerical methods to solve the system, the importance of the flux normalization and of the depletion chain is discussed.

### 2.5.1 Flux Normalization

The solution of equation 2.28, in multigroup approach, results in an eigenvector  $\vec{\phi}_0$ . This vector is not normalized. Its normalization is a key point in the creation of an evolution matrix  $\bar{A}$  representative of the actual evolution of the system. In fact, the flux term is used to account for the reaction rates, which describe the disintegration and formation of the isotopes.

Defining  $t_0$  the initial time of the evolution interval, and with  $t_f$  its final time, it is possible to distinguish two normalization techniques:

- **Constant flux depletion:**

the flux is imposed to be the same, equal to a value  $F$ , at the beginning and at the end of the interval:

$$\sum_{g=1}^G \phi^g(t_0) = \sum_{g=1}^G \phi^g(t_f) = F \quad (2.86)$$

where  $G$  is defined as the number of energy groups.

- **Constant power depletion:**

at the beginning and at the end of the time interval, the power released is imposed equal to  $W$  (in MW):

$$\begin{aligned} \sum_{j=1}^J \left[ \sum_{g=1}^G \kappa_{f,j}^g \sigma_{f,j}^g(t_0) \phi^g(t_0) \right] N_j(t_0) + \sum_{j=1}^{N_{iso}} \left[ \sum_{g=1}^G \kappa_{\gamma,j}^g \sigma_{\gamma,j}^g(t_0) \phi^g(t_0) \right] N_j(t_0) = \\ = \sum_{j=1}^J \left[ \sum_{g=1}^G \kappa_{f,j}^g \sigma_{f,j}^g(t_f) \phi^g(t_f) \right] N_j(t_f) + \sum_{j=1}^{N_{iso}} \left[ \sum_{g=1}^G \kappa_{\gamma,j}^g \sigma_{\gamma,j}^g(t_f) \phi^g(t_f) \right] N_j(t_f) = C_0 W \end{aligned} \quad (2.87)$$

where  $\kappa_{f,j}^g$  and  $\kappa_{\gamma,j}^g$  are the energy released in MeV respectively per fission and radiative capture in the energy group  $g$  of the isotope  $j$ ,  $J$  is the number of fissile isotope,  $N_{iso}$  the number of all the isotope present and  $C_0$  is a conversion factor from MW to MeV.

It is important to underline that the flux normalization is only imposed at the beginning and at the end of the time interval, not within the interval. In this work, the constant power depletion technique will be used.

### 2.5.2 Depletion Chain

The depletion chain describes the father-daughter relations of the different nuclides. It contains information on the neutron induced reactions and disintegration modes of each nuclide  $j$ : the daughter nuclides that can be formed, the relative importance of each reaction or decay mode  $\rho$  (called branching ratio  $\beta_{\rho,j}$ ) and the decay constant  $\lambda_j$ . Usually, nuclides are divided into two major categories: actinides (or heavy nuclei) and fission products. A third category contains the structural materials. In fact, also the nuclei in the cladding, for instance, are modified by neutron induced reactions.

In figure 2.6, it is possible to see the uranium cycle. This cycle is of primary interest in a fast reactor charged with MOX fuel. It is important to underline that, in a reactor, actinides different from the ones present in the fresh fuel can be produced. These actinides can be distinguished into fissile isotopes or not fissile isotopes. Fissile isotopes produce fission products with a certain probability  $Y(A, E)$ , where  $A$  is the atomic mass number of the fission product and  $E$  is the energy the fission reaction occurs at. This probability is called fission product yield. The probability distribution is usually normalized to 2. Two fission products are produced per fission if ternary fission is neglected.

In figure 2.7, it is possible to see the fission product yields for U235 at 0.0253 eV. The points represent the fission product. In a depletion chain, not all the possible fission products are considered. In fact, the aim of the depletion chain is not to physically describe all the productions and transmutations that occur in a reactor (that is a number incredibly high), but to represent the reactivity loss during the reactor operation. As a consequence, only a limited number of fission products and actinides is considered in a lattice or micro-depletion calculation, usually lumping those isotopes which quickly disintegrate with more stable ones. Only the isotopes with a time-scale comparable with the one of the reactor operation, and which are important to describe the reactivity loss, are taken into account in the depletion chain. As a consequence of the lumping procedure, the values and the fission-daughter relations that appear in a depletion chain do not directly derive from the JEFF evaluation, but they are properly re-elaborated. Since the description of the reactivity loss is different in each kind of reactor (PWR, SFR, CANDU,...), different depletion chain can be used. The dependency of the fission yields from the incident neutron fission energy is condensed into energy groups:  $Y^g(A)$ .

In this work, the CEA-V5 depletion chain is used. This is a multi-purpose depletion chain which contains 126 fission products, 26 actinides and 5 additional isotopes. Comparing it with a reference chain with far more isotopes (885 fission products and 26 actinides), it represents the 99.9% of the reactivity loss in a SFR [38]. Fission yields are defined both for thermal fission ( $< 2.5$  KeV) and fast fission ( $> 2.5$  KeV).



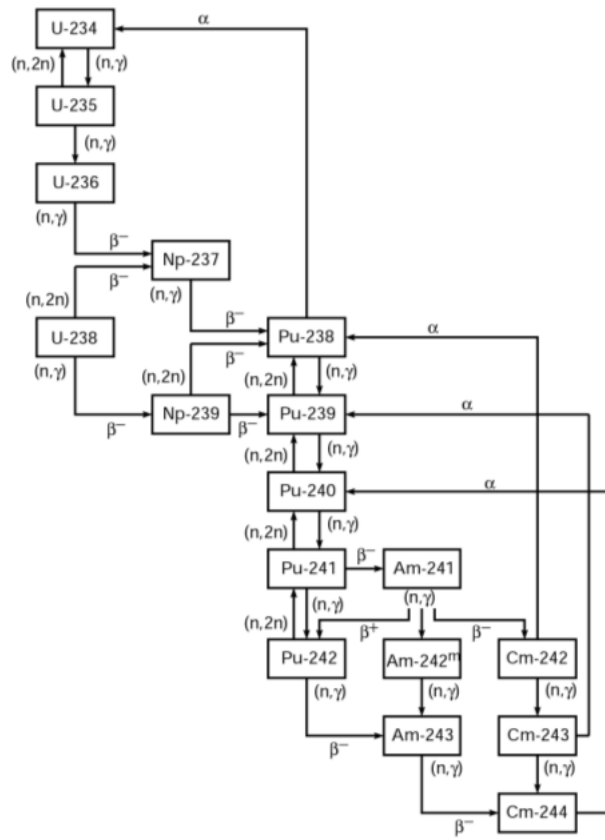


Figure 2.6 Depletion chain of the uranium cycle

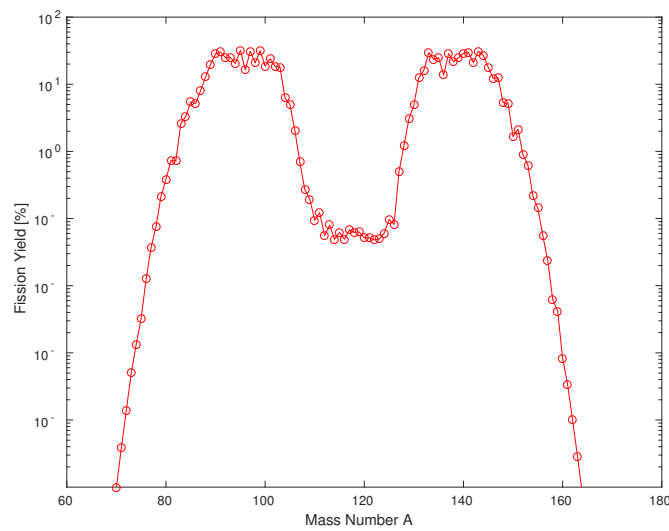


Figure 2.7 Fission product yields for U235 @0.0253 eV

### 2.5.3 ERANOS depletion solver

The ERANOS depletion solver is based on the assumption that the evolution matrix  $\bar{\bar{A}}$  is time independent. During the time interval  $\Delta t = t_f - t_0$ , the reaction rates are supposed to be constant:  $\bar{\bar{A}}(\lambda, \tau(t_0))$ . An analytic technique can be used to solve system 2.85. The exponential matrix  $e^{\bar{\bar{A}}(\lambda, \tau(t_0))t}$  is introduced:

$$\vec{N}(t_f) = \left( e^{\bar{\bar{A}}(\lambda, \tau(t_0))t_f} \right) \cdot \vec{N}_0 \quad (2.88)$$

This matrix is represented by a Taylor's series:

$$e^{\bar{\bar{A}}(\lambda, \tau(t_0))t} = \bar{\bar{I}} + \bar{\bar{A}}t + \frac{1}{2}\bar{\bar{A}} \cdot \bar{\bar{A}}t^2 + \dots \quad (2.89)$$

Unfortunately, it is not possible to have an infinite Taylor's series to exactly reproduce the exponential matrix.  $\Delta t$  is consequently divided into sub-interval whose length follows a power of 2. The first sub-interval is half the second which is a quarter of the third and so on. This sub-division reduce the expansion order of the Taylor's series required.

### 2.5.4 MENDEL depletion solver

The DARWIN depletion solver can be used in various application fields such as nuclear fuel cycle, dismantling, thermonuclear fusion, accelerator driven systems, medicine etc [11]. MENDEL offers iso-capacity with DARWIN and aims to be its successor [12]. In this work, MENDEL is used for reactor physics calculations, coupled with a transport code as APOLLO3 or TRIPOLI4. Among the various methods implemented to solve the depletion equations, in this case, a 4<sup>th</sup> order Runge-Kutta integration method is used to solve the integral:

$$\vec{N}(t_f) = \vec{N}(t_0) + \int_{t_0}^{t_f} \bar{\bar{A}}(\lambda, \tau(t)) \cdot \vec{N}(t) dt \quad (2.90)$$

Integral 2.90 requires an estimation of the time variation of the evolution matrix  $\bar{\bar{A}}$ . Reaction rates continuously change, even if  $\Delta t$  is small enough to assure a weak variation of the operative conditions.  $\tau(t)$  can be assumed constant or it can be linearly or quadratically extrapolated. Imposing a variation of the reaction rates allows to deal with a linear problem. Once that the reaction rate variation is set (a constant, or a linear/quadratic polynomial), the monostep approach consists only in applying the Runge-Kutta integration method to get  $\vec{N}(t_f)$ .

For the multistep approach, more complex algorithm are implemented. This complexity results in more accurate estimations of  $\vec{N}(t_f)$ . That's why multistep methods are preferred

in solving differential equations. Two different multistep algorithms, that will be later presented, are implemented for TRIPOLI4 and APOLLO3: the first is a predictor-corrector scheme, while the second is a predictor-evaluation-corrector scheme.

However, both monostep and multistep approaches solve integral 2.90 with the same numerical method. Defining the sub-interval  $h = t_{i+1} - t_i \in \Delta t$ , the 4<sup>th</sup> order Runge-Kutta method is the following:

$$\begin{cases} \vec{k}_1 = h\bar{\bar{A}}(t_i) \cdot \vec{N}_i \\ \vec{k}_2 = h\bar{\bar{A}}(t_i + \frac{h}{2}) \cdot (\vec{N}_i + \frac{\vec{k}_1}{2}) \\ \vec{k}_3 = h\bar{\bar{A}}(t_i + \frac{h}{2}) \cdot (\vec{N}_i + \frac{\vec{k}_2}{2}) \\ \vec{k}_4 = h\bar{\bar{A}}(t_i + h) \cdot (\vec{N}_i + \vec{k}_3) \\ \vec{N}_{i+1} = \vec{N}_i + \frac{\vec{k}_1}{6} + \frac{\vec{k}_2}{3} + \frac{\vec{k}_3}{3} + \frac{\vec{k}_4}{6} + O(h^5) \end{cases} \quad (2.91)$$

with  $\vec{N}_i = \vec{N}(t_i)$  and  $\vec{N}_{i+1} = \vec{N}(t_{i+1})$ .

In figure 2.8, it is possible to get a visual representation of the method. An increment of the function is evaluated once at  $t_i$  and twice at the midpoint. It is then evaluated at  $t_{i+1}$ . The Simpson integration formula is then applied to estimate  $\vec{N}_{i+1}$  [39]. Proper algorithms are implemented to optimize the size of the integration step  $h$ .

### TRIPOLI4 Predictor-Corrector scheme

In TRIPOLI4, a predictor-corrector scheme is implemented. This scheme is a multistep method implemented to solve a system of differential equation. Differently from the monostep scheme, where only one flux evaluation is required, this one requires two flux evaluations. This fact doubles the calculation time. Increasing the calculation effort, however, allows to get more accurate results. The scheme is here described:

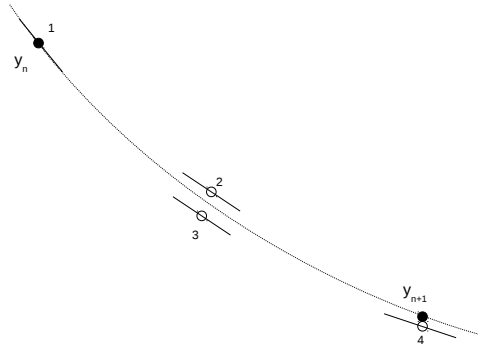


Figure 2.8 Fourth order Runge-Kutta integration method

- **Predictor step:**  $\vec{N}(t_f)^{(p)}$  is evaluated using constant reaction rates at  $t_0$ :  $\tau(t_0)$ . Flux  $\phi(t_f)^{(p)}$  is then evaluated at  $t_f$ , using  $\vec{N}(t_f)^{(p)}$ .
- **Corrector step:**  $\vec{N}(t_f)^{(c)}$  is evaluated using  $\phi(t_f)^{(p)}$  and  $\vec{N}(t_0)$  to compute the reaction rates  $\tau(t_0)^{(c)}$ .

Finally, the concentrations at  $t_f$  are the average of the concentrations evaluated at the predictor and corrector steps:

$$\vec{N}(t_f) = \frac{\vec{N}(t_f)^{(p)} + \vec{N}(t_f)^{(c)}}{2} \quad (2.92)$$

In this work, all the TRIPOLI4 depletion calculations are performed with this multistep method.

### APOLLO3 Predictor-Evaluation-Corrector scheme

In APOLLO3, a predictor-evaluation-corrector scheme is implemented. This scheme is a multistep method implemented to solve a system of differential equation. Differently, from the predictor-corrector scheme, an evaluation step is added. As it will be later explained, the scheme is more complex, but it ensures a convergence test on the results.

The first major difference with the TRIPOLI4 scheme is that reaction rates can be assumed to vary linearly or quadratically. Or they can just be a constant. But if a variation is assumed, an extrapolation of the reaction rate behaviour is done by considering an interpolation between  $t_0$  and the previous step  $t_{-1}$  in the case of linear variation,  $t_0$ ,  $t_{-1}$  and  $t_{-2}$  in the case of quadratic polynomial.

The interpolated polynomial is then used to extrapolate the reaction rates at  $t_f$ . This assure a non-constant evaluation matrix  $\bar{A}$ . But, if the operation conditions vary considerably between  $t_0$  and  $t_f$ , the extrapolation of the reaction rates cannot ensure positive values. This fact is physically unacceptable. That's why a constant evolution matrix is used if large flux variations between the initial and final states are expected.

Once that reaction rates are extrapolated, concentrations are evaluated at  $t_f$ . To ensure the convergence of the results, the predictor-evaluation-corrector scheme is implemented:

- **Predictor step:**  $\tau_{ext}^{(p)}(t)$  is extrapolated using  $\tau(t_0)$ ,  $\tau(t_{-1})$  (linearly) and  $\tau(t_{-2})$  (quadratically). Concentrations  $\vec{N}^{(p)}(t_f)$  are evaluated.
- **Evaluation step:**  $\vec{N}^{(p)}(t_f)$  is used to evaluate the flux  $\vec{\phi}^{(p)}(t_f)$  at  $t_f$ . Reaction rates  $\tau^{(p)}(t_f)$  are then computed and used to interpolate  $\tau_{int}^{(ev)}(t)$  along with  $\tau(t_0)$  (linearly) and  $\tau(t_{-1})$  (quadratically). A new evaluation matrix allows to evaluate the concentrations  $\vec{N}^{(ev)}(t_f)$ . If  $\|\vec{N}^{(ev)}(t_f) - \vec{N}^{(p)}(t_f)\| < \epsilon$ , where  $\epsilon$  is the convergence parameter,

the convergence is assumed and  $\vec{N}(t_f) = \vec{N}^{(p)}(t_f)$ ,  $\vec{\phi}(t_f) = \vec{\phi}^{(p)}(t_f)$  and  $\tau(t_f) = \tau^{(p)}(t_f)$ . Otherwise, if convergence is not reached, the corrector step is required.

- **Corrector step:**  $\vec{N}^{(ev)}(t_f)$  is used to evaluate the flux  $\vec{\phi}^{(ev)}(t_f)$ . Reaction rates  $\tau^{(ev)}(t_f)$  are then computed and used to interpolate  $\tau_{int}^{(c)}(t)$  along with  $\tau(t_0)$  (linearly) and  $\tau(t_{-1})$  (quadratically). A new evaluation matrix allows to evaluate the concentrations  $\vec{N}^{(c)}(t_f)$ . If  $\|\vec{N}^{(c)}(t_f) - \vec{N}^{(ev)}(t_f)\| < \epsilon$ , the convergence is assumed and  $\vec{N}(t_f) = \vec{N}^{(ev)}(t_f)$ ,  $\vec{\phi}(t_f) = \vec{\phi}^{(ev)}(t_f)$  and  $\tau(t_f) = \tau^{(ev)}(t_f)$ . Otherwise, if convergence is not reached, the time interval  $\Delta t = t_f - t_0$  is reduced:  $\Delta t \rightarrow \Delta \tilde{t} = \alpha \Delta t$  with  $\alpha \in (0, 1)$ .

Usually the time interval is split in 2 ( $\alpha = 0.5$ ). All the scheme is consequently repeated for  $t \in [t_0, t_0 + \alpha \Delta t]$  and then for  $t \in [t_0 + \alpha \Delta t, t_f]$ .

In this work, the APOLLO3 evolution scheme will be studied in 3.1.1. The differences between the monostep and multistep method and the different extrapolation/interpolation functions will be investigated.

### 2.5.5 Treatment of statistical uncertainties in Monte Carlo burn-up codes

The last few words on the solution of the depletion equations must be spent on the treatment of the statistical uncertainties in Monte Carlo burn-up code. In fact, interfacing a Monte Carlo transport code with a depletion solver means interfacing probabilistic estimations with deterministic results. The problem in the propagation of the statistical uncertainties is related to the fact that, once that the flux and the reaction rates are estimated, with a certain uncertainty  $\sigma$  associated, these values are inserted in the Bateman equations without  $\sigma$ .

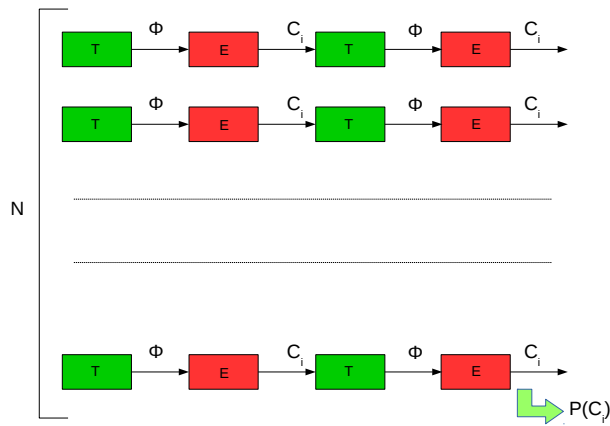


Figure 2.9 Independent transport-depletion simulations

Bateman equations are solved with the values given by the transport code, but the uncertainties associated to these values are not propagated. At each time interval, uncertainties are eliminated when it is time to interface TRIPOLI4 and MENDEL, so that the values introduced in the depletion equations are treated as deterministic results and not as statistical estimated quantities.

Therefore, in order to correctly propagate the uncertainties and to associate  $\sigma$  also to the concentrations, not only one simulation with a great number of neutron histories is accomplished, but more independent simulations with a smaller number of histories [40]. These simulations allow to evaluate isotope concentrations more times with different flux estimations and consequently to reproduce a statistical distribution of the concentrations. Using statistical instruments, it is then possible to associate a certain statistical uncertainty to the concentrations at each time step. This procedure is visualized in figure 2.9 and it allows to correctly propagate the uncertainties also for flux, multiplication factor and reaction rates.

## CHAPTER 3 EVOLUTION OF A CFV CELL GEOMETRY

The aim of this chapter is to present depletion calculations performed on a CFV elementary cell geometry. It is divided into two part in order to distinguish the lattice depletion and the core one. Comparing core depletion models is the aim of this work but, in order to do so, depletion calculations on the lattice part of APOLLO3 must be validated. It is important, before starting, to stress the point that APOLLO3 is able to perform both lattice and core calculations. From now on, if not expressed otherwise, the term “lattice” will describe 1968 energy group calculations with the transport solver TDT-MOC. The term “core” will describe 33 energy group calculations with the transport solver MINARET. Other differences, that will be explained later, are present. All APOLLO3 calculations, nevertheless, use MENDEL depletion solver.

### 3.1 Lattice Depletion

This introductory part does not aim to start answering to the research question, but it introduces and validates the instruments that will be used in section 3.2.

In fact, its purpose is to validate lattice depletion calculations in APOLLO3. In order to do so, the Monte Carlo reference code TRIPOLI4 has been used. This code shares with APOLLO3 the depletion solver MENDEL. To exclude the presence of possible errors in MENDEL, the chain of codes ECCO/ERANOS has been added to this inter code validation procedure. ERANOS, in fact, has its own depletion solver and can provide a third party guarantee. The descriptions of the depletion solvers has been provided in section 2.5.

Before starting with the actual validation, it is necessary to discuss certain option and modelling choices which concern APOLLO3 calculations:

- Evolution Temporal Scheme: focusing on reaction rates’ extrapolation/interpolation type and monostep/multistep scheme differences
- Self-shielding reiteration during the evolution: is it necessary? For what nuclei? At which time step?
- Does the use of the Tone method (see section 2.4.4) introduce a drift of the reactivity difference during the evolution?

All the calculations will be performed on the geometry shown in figure 3.1. This geometry represents 1/12 of an hexagonal CFV cell. 4 zones are identified:

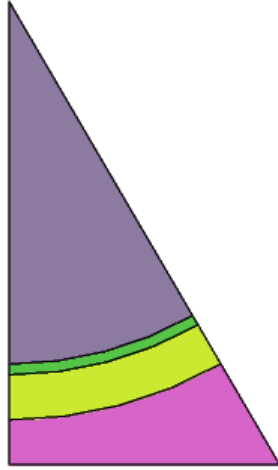


Figure 3.1 CFV cell geometry

- the external coolant zone containing the sodium
- the external ring representing the cladding, a Ni-Fe-Cr alloy
- the voided gap embracing the fuel
- the internal circular surface containing MOX fuel.

Both lattice and core APOLLO3 calculations are performed with specular reflective boundary conditions. It is important to say, before starting, that both the evolution and self-shielding geometries that will be used for lattice calculations do not divide the fuel region in sub-region to account for the rim effect. In fast reactors, in fact, the flux distribution inside the fuel pin is almost constant, contrarily from thermal reactors (see appendix A). At higher energy, neutrons are less likely to interact, and this increases their mean free path, flattening the flux distribution. Thus, sub-region inside the fuel, then, are not required.

### 3.1.1 Preliminary Studies

#### Evolution Temporal Scheme

In order to validate the evolution temporal schemes, a depletion calculation, where the self shielding of only the heavy nuclei is reiterated at each time step, has been considered.



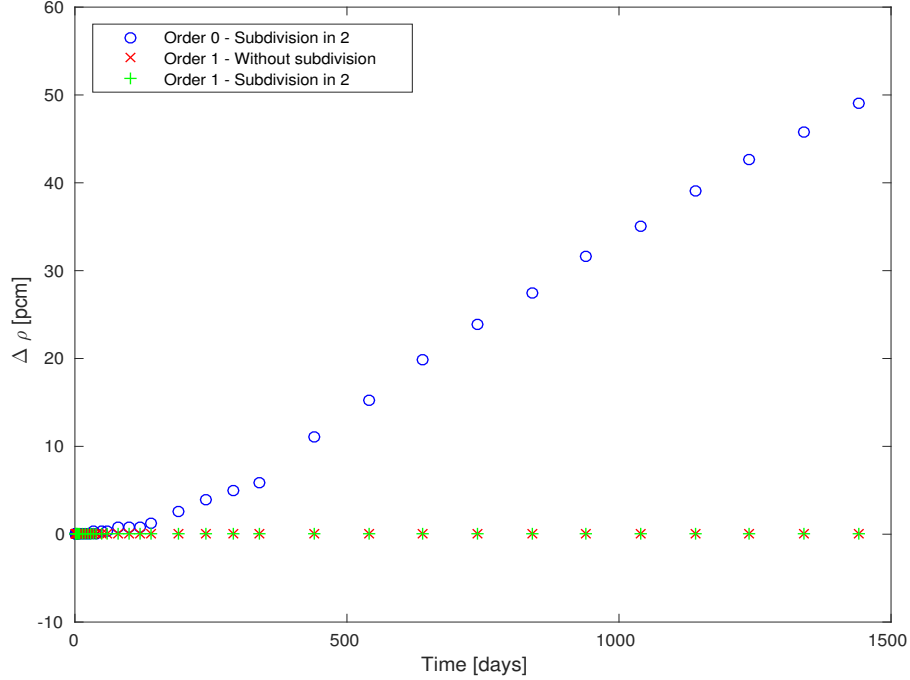


Figure 3.2 Convergence of CFV cell  $k_{inf}$  in the different evolution temporal scheme of “lattice” APOLLO3 (reference: parabolic scheme)

Amongst the eight heavy nuclei initially present in the fresh fuel, five are those self-shielded at each time step (U235, U238, Pu239, Pu240, Pu241). In such a case, the next section will show that a good estimation of the reactivity loss is obtained with respect to a calculation where 74 fission products, representing 99% of anti-reactivity, are considered.

Constant and linear extrapolation/interpolation options have been compared to a reference parabolic calculation with splitting of the time step in 2. The results of figure 3.2 show:

- the linear option, with or without time splitting in 2, is perfectly converged: differences are smaller than 0.2 pcm all the evolution long. The chosen time steps are well adapted to describe the phenomenon.
- the constant option, even with the time splitting in 2, introduces a linearly increasing drift during the time evolution: this one is equal to +50 pcm at 1440 days. The inflection point at 340 days is the moment when the time step passes from 50 to 100 days. For this option, a convergence criterion of  $10^{-5}$  does not seem satisfying.

These results are interesting because they show that the linear schemes - and among them even the TRIPOLI4 one - are reliable and provide good results.

For all the following calculations, the linear scheme will be used. This option will limit the

number of flux calculations and the information storage with respect to the parabolic one. The possibility of the time-step splitting in 2 is conserved even if, in this case, it is not invoked.

### Self-shielding reiteration

Self-shielding with the method of the sub-group (see 2.4.4) is time demanding and expensive. Despite this, it is the reference method for SFR. This method, indeed, requires a great number of exact 2D collision probability calculations, performed with the module TDT-CPM. An alternative is the Tone method. This one is slightly less accurate but it is greatly faster (up to 30 times). This characteristic makes it more interesting if reiterated self-shielding is required during the evolution.

For time issues, it is not contemplated to self-shield all the heavy nuclei and fission products during the evolution. Four calculations, performed with Tone method and 4 macro groups of fission spectra, have been compared:

1. self-shielding is not reiterated
2. self-shielding is reiterated. Heavy nuclei only are self-shielded.
3. self-shielding is reiterated. Heavy nuclei and the 11 fission products which contribute the most to the capture (60% of the fission product capture) are self-shielded.
4. self-shielding is reiterated. Heavy nuclei and the 74 fission products (99% of the fission product capture) are self-shielded.

The last one is considered as a reference. In figure 3.3, reactivity differences between the reference and the others are shown. Before commenting these results it is important to note that the self-shielding is reiterated at each time step, which is without a doubt unnecessary and can be optimized. Returning on figure 3.3, a limited difference is observed at 1440 days if the number of fission products is reduced to 11 (-6 pcm) or to 0 (-13 pcm). If self-shielding is not reiterated, the difference is a little bit higher. The maximum is at 940 days and it is equal to +19 pcm. At 1440 days, the difference is reduced to +10 pcm.

The detailed analysis of the reactivity balance shows that the error of +19 pcm is the result of minor compensations.

It is not necessary, consequently, to reiterate the self-shielding during the evolution. The shielding of the heavy nuclei only at time zero is enough. However, in order to strictly test core evolution calculations, option number 2 has been chosen and used for the rest of the study. Self-shielding of the heavy nuclei is reiterated.

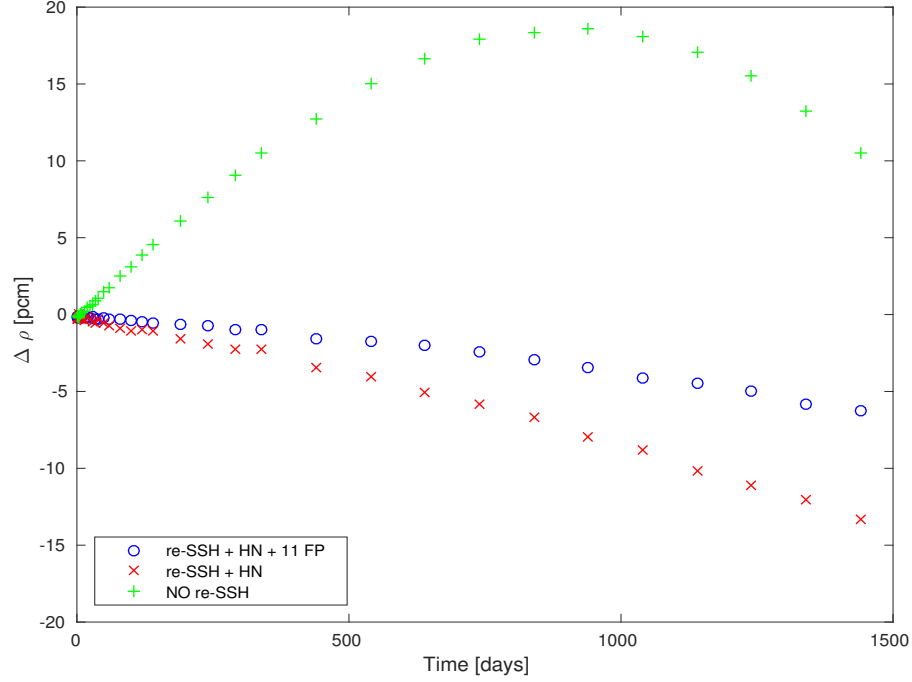


Figure 3.3 Impact of the evolution self-shielding of heavy nuclei and fission products on CFV cell  $k_{inf}$

### Tone Method Validation

At time zero the reactivity difference between the Tone and the sub-group methods is equal to -2 pcm. Its behaviour during the time evolution must be validated. In figure 3.4, it is possible to notice the reactivity difference between the first three models introduced in the previous paragraph. It has not been possible to compare the fourth model. Tone and sub-group methods have been applied for the self-shielding. The drift of the reactivity difference is limited to 3 pcm during the evolution. Tone method will be used from now on.

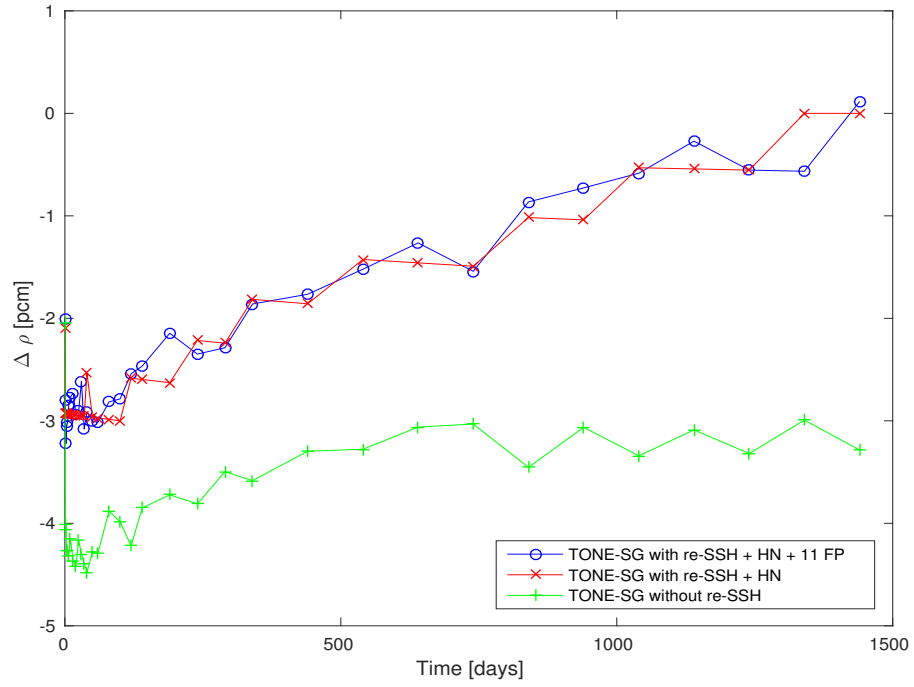


Figure 3.4 CFV cell  $k_{inf}$  comparison during the evolution: Tone Method - Sub-group Method

### 3.1.2 Inter-Code Validation

#### APOLLO3, TRIPOLI4, ECCO/ERANOS

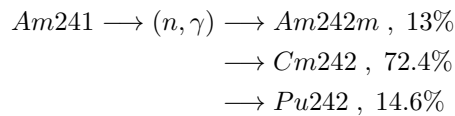
It is useful, before starting the inter-code validation, to remind the reasons why the “lattice” APOLLO3 has been compared to TRIPOLI4 and ECCO/ERANOS:

- TRIPOLI4 flux calculation is used as reference if the number of neutron histories is high enough: for a 2D CFV cell, 2 billion histories are necessary to reach a precision of 3 pcm ( $1\sigma$ ) for the multiplication factor at time 0; 500 million histories provide a precision of 5 pcm ( $1\sigma$ ) at 1440 days. In depletion calculations, such a number of histories can't be simulated, because the transport solver can't be parallelized. In this case, 256 independent simulations have been performed. At each time step, 25.6 million histories have been launched, increasing by a factor 10 the statistic uncertainty:  $\pm 30$  pcm ( $1\sigma$ ).
- The chain of code ECCO/ERANOS guarantees that APOLLO3 and TRIPOLI4 are not subjected to the same errors, because both of them use MENDEL depletion solver and an identical decay chain. ERANOS has its own depletion solver. The decay chain has been translated from the MENDEL one (the same nuclei are present, apart few exceptions of minor entity, and fast fission yields -  $> 2.5keV$  - from JEFF3.1.1 are the same) <sup>1</sup>.

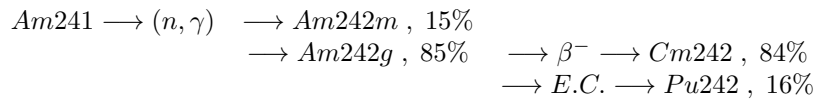
---

<sup>1</sup> Dy165 and Te131m have been neglected and their fission yields added to Ho165 and I131 respectively. Am241 has been modified:

MENDEL chain:



ERANOS chain:



Am242g has been added in order to write an interpretable chain for the ERANOS depletion solver. Another difference is that MENDEL chain presents thermal ( $< 2.5keV$ ) and fast ( $> 2.5keV$ ) fission yields. This division is not interpretable by ERANOS, whose fission yields are independent of the incident neutron energy. Because a SFR is considered, the assumption that all the fissions are fast ones is made. The quantitative discussion of this assumption is postponed to section 3.2.1.

Concerning ECCO, the geometry is not hexagonal but cylindrical (sodium volume is conserved). In addition, isotropic (white) and not specular boundary conditions have been used. The bias related to these approximations is of the order of a few pcm.

## Time 0

In table 3.1, it is possible to see the infinite multiplication factors obtained with the three codes and their comparison with the reference code TRIPOLI4. For APOLLO3 calculations, a particular importance is given to the number of spectra used. If one secondary neutron fission spectrum is used, equation 2.25 describes the fission source and the secondary neutron distribution is independent from the incident neutron energy. Equation 2.36 describes a fission source where NMG macro groups of fission spectra are used. A dependency of the secondary neutrons on the incident neutron energy is introduced.

It is possible then to notice that the difference is limited to a maximum of +29 pcm for the APOLLO3 calculations with 4 macro groups of fission spectra. However, the results are strongly influenced by the number of fission spectra used. In figure 3.5, it is possible to observe the fuel flux difference between the deterministic codes and the Monte Carlo one. This difference is normalized to the energy integrated flux, that has, from its side, been already normalized to the total production ( $\sum_i \sum_g (\nu \Sigma_f)_i^g \phi_g = k_{inf}$ , where  $g$  is the number of energy group and  $i$  the number of the fissile and fissionable isotope).

With respect to 4 spectra, 1 spectrum calculation tends to underestimate the flux distribution over 1 MeV and overestimate it below (see figure 3.6). This is translated, and it is possible to see it in table 3.2, in an underestimation of the U238 fission reaction, that is a threshold reaction (fissionable isotope), and an overestimation of the Pu239 fission, that is a fissile isotope. These effects can compensate to reduce the reactivity difference. In 4 spectra APOLLO3 calculations, where this compensation does not occur, the reactivity difference is higher, even if a better estimation of U238 fission reaction rate is done.

Before passing to depletion calculations, it is important to note that 1 spectrum APOLLO3 calculations are made considering the thermal fission spectrum only (figure 3.7), whereas the ECCO fission spectrum is *ad hoc* averaged for SFR application.

## Depletion Calculations

Depletion calculations are now compared. All the results are listed in appendix C, together with the time mesh used for the MOC reference calculations and cross section library creation. In figure 3.8, the results are shown. The error bars are not negligible in this case. The explanation has already been discussed at the beginning of section 3.1.2. It is interesting to

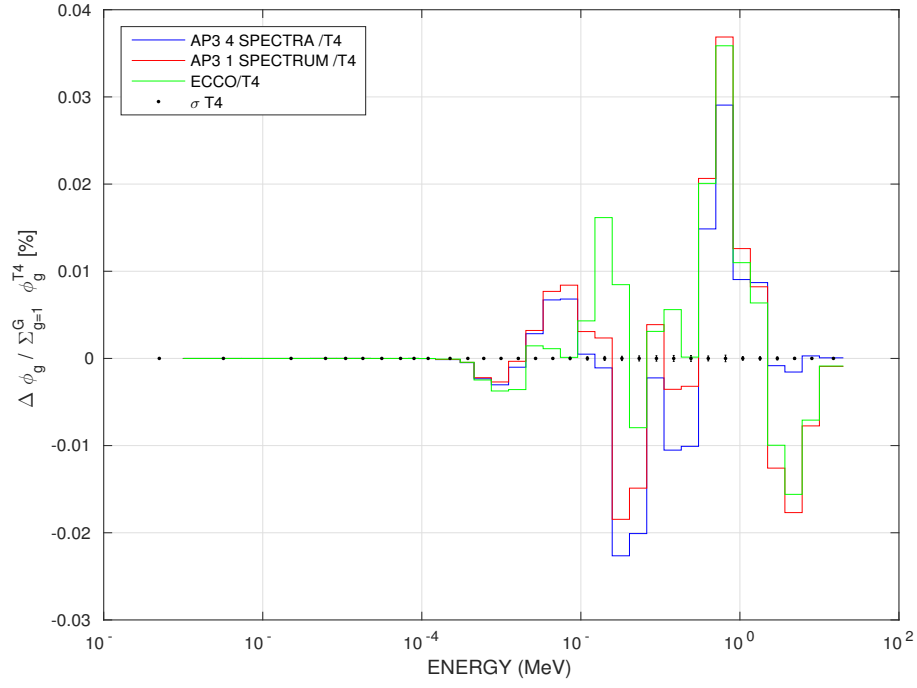


Figure 3.5 Relative flux difference with respect to TRIPOLI4 at time 0

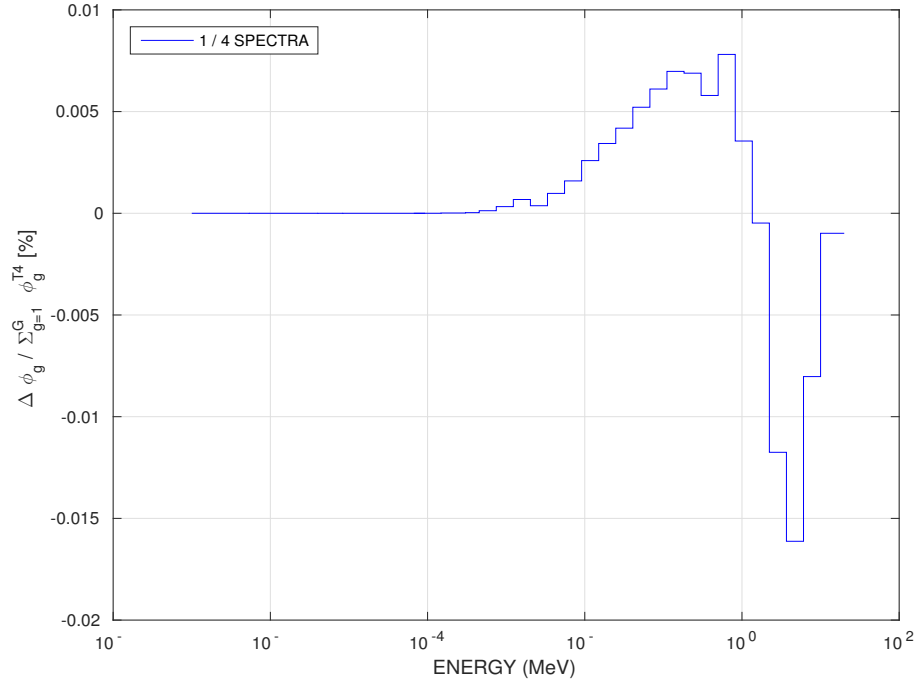


Figure 3.6 Relative flux difference between APOLLO3 1 spectrum and 4 spectra calculations at time 0

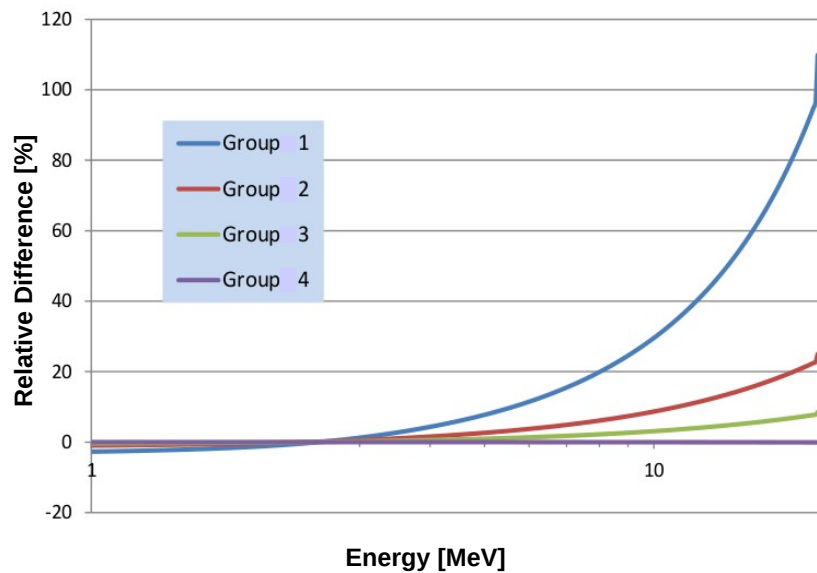


Figure 3.7 Relative difference between the Pu239 4 macro group fission spectra and 1 macro group one in the APOLLO3 library.

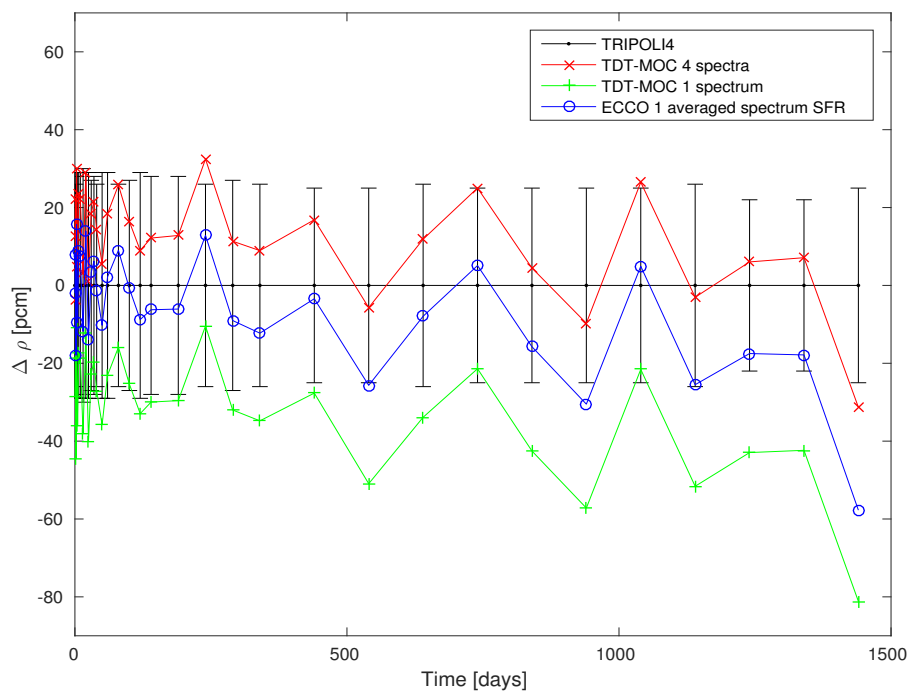


Figure 3.8 CFV cell  $k_{inf}$  comparison during the evolution - APOLLO3 and ECCO with TRIPOLI4



Table 3.1 Inter-code validation: Time 0

TRIPOLI4			
$k_{inf}$		$\sigma$ [pcm]	
1.54609		$\pm 3$	
APOLLO3			
1 SPECTRUM		4 SPECTRA	
$k_{inf}$	$\Delta\rho$ [pcm]	$k_{inf}$	$\Delta\rho$ [pcm]
1.54580	-12	1.54678	+29
ECCO			
1 SPECTRUM			
$k_{inf}$		$\Delta\rho$ [pcm]	
1.54643		+14	

notice that the reactivity difference between the two codes is constant during the evolution and this explains the fact that the three curves are parallel all the evolution long. The number and the type of fission spectra have a dominant role in the neutron balance, as already observed in the previous paragraph. The APOLLO3 4 spectra curve lies inside the error bars during most of the evolution, demonstrating that the choice of 4 macro groups is the most accurate for depletion calculations. Concerning the concentrations, in the appendix D, it is possible to see the final concentrations (time 1440) for the 18 most important actinides and the 74 fission products that contribute for 99% of the total fission product capture. In the table, the concentrations evaluated with TRIPOLI4 and their uncertainties are listed. The relative comparison is made between these results and the concentrations evaluated with APOLLO3 and ECCO.

Focusing on the concentrations obtained with APOLLO3, it is possible to observe that no major difference are present if 4 macro groups of fission spectra are used instead of 1. The difference in the concentration estimation is limited in both the two cases. For the actinides a maximum of  $\pm 1.91\%$  for the Cm244 and Np237 is observed in 1 spectrum calculations. In 4 spectra ones, the difference is limited to  $1.72\%$ . The concentration differences are not high enough to alter significantly reaction rate estimation and, consequently, the neutron balance (see table 3.3).

Before passing to the ECCO concentrations, it is important to remind the modifications applied to the decay chain. These modifications have been made to make the chain interpretable for ECCO code, but they have altered a little bit the results. Modifying the Am241 chain, in fact, a difference has been introduced. At 1440 days, the Am242M concentration is highly overestimated ( $+14.86\%$ ). The other actinides, on the contrary, suffer from errors which are comparable with the APOLLO3 ones (Np237:  $-2.10\%$ ).

Few fission products, equally, present a not negligible difference. Xe131, In115 and Br81 are the ones whose effects on the reactivity is more important. The differences, in this case, arise from the fact that only fast fission yields are used. However, concentration differences slightly affect the neutron balance. Their effects will be discussed in the next section (see table 3.3). It will be possible to conclude that, even if the three codes are not perfectly coherent in the concentration estimation, they are perfectly coherent in the anti-reactivity representation: they describes the loss of reactivity the cell undergoes with good agreement.

### Time 1440

The multiplication factor of the 500 million histories TRIPOLI4, made with the final concentrations of the TRIPOLI4 depletion calculation, is shown in table 3.4. The comparisons between TRIPOLI4 reaction rates and the one obtained with APOLLO3 and ECCO are shown in table 3.3. The same considerations made for time 0 can be done: the difference between a spectrum which depends on the neutron incident energy and one which does not is that the flux is a little bit softer (as observed in figure 3.6). U238 fission, which is a threshold reaction, is underestimated and thermal absorption of Pu239 overestimated. The formation of Pu240, a fissionable isotope similar to U238, shows the same tendency: fission reactions are underestimated.

Concerning APOLLO3, the compensation, in this case, is particularly favourable for 4 spectra; a difference of +52 pcm is present in 1 spectrum case.

Concerning ECCO, in table 3.3, even the reaction rates of the fission products whose concentration differences are not negligible are listed. It is possible to show that their importance in the neutron balance is minor. An overall compensation and the use of a SFR averaged fission spectrum lead to a multiplication factor that is located, as shown in figure 3.8, between the APOLLO3 4 and 1 spectra calculations.

To sum up, it is possible to say that the validation is successful and no major errors are encountered in the MENDEL solver. In fact, even if concentrations differences are observed, the three codes are coherent to describe the anti-reactivity of the fission products, and the evolution of the actinides, without affecting the neutron balance.

In the following section, a reactivity analysis will be done in order to decompose the reactivity loss the CFV cell undergoes. A hierarchy of the fission products will be instituted in order to determine the isotopes which contributes the most to the neutron capture. One spectrum APOLLO3 will be considered, because of the importance it will assume in section 3.2. It will be the reference case for our depletion models. It has not been possible, in fact, to perform core calculations with more than one fission spectrum. This because the author has not found the function already coded at the moment of the calculations.

Table 3.2 Inter-code validation: Time 0 (in pcm, reaction rates normalized to 10<sup>5</sup> neutron production)

APOLLO3/ TRIPOLI4 [pcm]					
	1 SPECTRUM				
	Absorption	Capture	NuFission	Fission	N,xN
U238	-11	15	-84	-26	-6
Pu239	34	10	59	23	0
	4 SPECTRA				
	Absorption	Capture	NuFission	Fission	N,xN
U238	-2	-2	1	0	2
Pu239	23	5	53	18	0
ECCO/ TRIPOLI4 [pcm]					
	1 SPECTRUM				
	Absorption	Capture	NuFission	Fission	N,xN
U238	-13	10	-75	-23	-7
Pu239	45	4	112	41	0

Table 3.3 Inter-code validation: Time 1440 (in pcm, reaction rates normalized to  $10^5$  neutron production)

APOLLO3/ TRIPOLI4 [pcm]					
	1 SPECTRUM				
	Absorption	Capture	NuFission	Fission	N,xN
U238	-12	12	-76	-24	-5
Pu239	10	2	15	8	0
Pu240	-12	-5	-22	-6	-4
Am242M	10	9	0	0	0
Np237	-2	-2	-1	0	0
Cm244	2	1	2	1	0
	4 SPECTRA				
	Absorption	Capture	NuFission	Fission	N,xN
U238	-4	-2	-5	-2	-1
Pu239	1	-2	10	3	0
Pu240	-11	-8	-9	-3	4
Am242M	9	9	1	0	0
Np237	1	1	1	0	0
Cm244	2	1	2	1	0
ECCO/ TRIPOLI4 [pcm]					
	1 SPECTRUM				
	Absorption	Capture	NuFission	Fission	N,xN
U238	-1	21	-70	-22	-6
Pu239	10	-3	31	13	0
Pu240	-13	-5	-28	-8	4
Am242M	12	2	34	10	0
Np237	-2	-2	-1	0	0
Cm244	0	0	0	0	0
Xe131	8	8	0	0	0
Ze93	2	2	0	0	0
Cd111	1	1	0	0	0
I127	4	4	0	0	0
Rb85	0	0	0	0	0
Cd113	0	0	0	0	0
Br81	0	0	0	0	0
In115	1	1	0	0	0

Table 3.4 Inter-code validation: Time 1440

TRIPOLI4			
$k_{inf}$		$\sigma$ [pcm]	
1.31691		$\pm 5$	
APOLLO3			
1 SPECTRUM		4 SPECTRA	
$k_{inf}$	$\Delta\rho$ [pcm]	$k_{inf}$	$\Delta\rho$ [pcm]
1.31600	-52	1.31687	-2
ECCO			
1 SPECTRUM			
$k_{inf}$		$\Delta\rho$ [pcm]	
1.31641		-29	

### 3.1.3 Reactivity Analysis

#### Reactivity Difference Reconstruction

A nuclear reactor shows a delicate balance between the neutrons which are continuously produced and the ones which are continuously absorbed or which escape. In order to sustain a chain reaction, the multiplication factor  $k_{inf}$  is introduced in the steady state Boltzmann equation. The aim of this factor is to adjust the fission source so that a perfect balance can be achieved. In the case where a single cell with reflective boundary conditions is considered, the multiplication factor becomes nothing else than the ratio between the total number of neutrons produced by fission over the absorbed ones. There is no neutron loss due to the leakage.

It is possible to define with  $PROD_{tot}$  the total production reaction rate, with  $ABS_{tot}$  the total absorption reaction rate and with  $NEXC_{tot}$  the (n,xn) reaction rate. The production reaction rate  $PROD_{tot}$  takes into account the secondary fission neutrons and the ones from (n,xn) reactions. The last term, as a convention in APOLLO3, is added also to the macroscopic absorption cross section:

$$\Sigma_{ABS}^{r,g} = \Sigma_{fiss}^{r,g} + \Sigma_{capture}^{r,g} + \sum_x x \Sigma_{NxN}^{r,g} \quad (3.1)$$

Because, usually, reactions where  $x$  is greater than 2 give a negligible contribution, the absorption cross section is corrected subtracting only one time the (n,xn) contribution in order to approximately reduce to 1 the weight factor  $x$  which multiplies  $\Sigma_{NxN}^{r,g}$ :

$$\Sigma_{ABS}^{r,g} - \sum_x \Sigma_{NxN}^{r,g} \approx \Sigma_{fiss}^{r,g} + \Sigma_{capture}^{r,g} + \sum_x \Sigma_{NxN}^{r,g} \quad (3.2)$$

The multiplication factor can be then operatively defined as follows:

$$k_{inf} = \frac{PROD_{tot}}{ABS_{tot} - NEXC_{tot}} \quad (3.3)$$

where

$$\begin{aligned} PROD_{tot} &= \sum_{r=1}^R \sum_{i=1}^{N_f^r} \sum_{g=1}^G \tau_{prod}^{r,i,g} \\ ABS_{tot} &= \sum_{r=1}^R \sum_{i=1}^{N^r} \sum_{g=1}^G \tau_{abs}^{r,i,g} \\ NEXC_{tot} &= \sum_{r=1}^R \sum_{i=1}^{N^r} \sum_{g=1}^G \tau_{nexc}^{r,i,g} \end{aligned}$$

and  $R$  is the total region number,  $N_f^r$  are the fissile isotopes in region  $r$ ,  $N^r$  are the isotope in region  $r$  and  $G$  is the energy group number;  $\tau_x^{r,i,g}$  is the reaction rate for nuclear reaction  $x$ , for the isotope  $i$  in region  $r$  and for the energy group  $g$ .  $\tau_x^{r,i,g}$  is defined as follows:

$$\tau_x^{r,i,g} = N_i^r \sigma_{x,i}^{g,r} \phi_g^r V_r \quad (3.4)$$

where  $N_i^r$  is the concentration of the isotope  $i$  in region  $r$ ,  $\sigma_{x,i}^{g,r}$  is its cross section for  $g$  energy group,  $\phi_g^r$  the scalar flux and  $V_r$  the region volume. The production reaction rate is defined by the following:

$$\tau_{prod}^{r,i,g} = N_i^r \left( \nu_{f,i}^{g,r} \sigma_{f,i}^{g,r} + \sum_x x \sigma_{N_x N,i}^{g,r} \right) \phi_g^r V_r \quad (3.5)$$

Then, the integral reaction rate is defined as

$$\tau_x^{r,i} = \sum_{g=1}^G \tau_x^{r,i,g} \quad (3.6)$$

Usually, the code does not print out normalized reaction rates, so they are normalized to total production, indicating with the star the reaction rates before normalization:

$$\tau_x^{r,i,g} = (\tau_x^{r,i,g})^* \frac{k_{inf}}{PROD_{tot}^*} \cdot 10^{-5} = \frac{(\tau_x^{r,i,g})^*}{ABS_{tot}^* - NEXC_{tot}^*} \cdot 10^{-5}$$

The following relationships are, then, defined:

$$PROD_{tot} = k_{inf} \cdot 10^{-5}$$

$$ABS_{tot} - NEXC_{tot} = 10^{-5}$$

In general  $NEXC_{tot} \ll ABS_{tot}$  and so  $ABS_{tot} \approx 10^{-5}$ .

The reactivity difference is the major objective. It is defined between state 1 and 2, with the following relationship:

$$\begin{aligned} \Delta\rho &= \frac{1}{k_{inf}^1} - \frac{1}{k_{inf}^2} \approx \frac{ABS_{tot}^1}{PROD_{tot}^1} - \frac{ABS_{tot}^2}{PROD_{tot}^2} = \\ &= \sum_{r=1}^R \sum_{i=1}^{N^r} \sum_{g=1}^G \left( \frac{(\tau_{abs}^{r,i,g})^1}{PROD_{tot}^1} - \frac{(\tau_{abs}^{r,i,g})^2}{PROD_{tot}^2} \right) \end{aligned}$$

from which it is possible to define the reactivity difference due to the isotope  $i$  in region  $r$  as follows:

$$RD^{i,r} = \sum_{g=1}^G \left( \frac{(\tau_{abs}^{r,i,g})^1}{PROD_{tot}^1} - \frac{(\tau_{abs}^{r,i,g})^2}{PROD_{tot}^2} \right) \quad (3.7)$$

The reactivity  $\Delta\rho$  is, then, the summation of all the reactivity difference due to every isotope  $i$  in every region  $r$ :

$$\Delta\rho = \sum_{r=1}^R \sum_{i=1}^{N^r} RD^{i,r} \quad (3.8)$$

The importance of isotope  $i$  belonging to region  $r$  is:

$$I = \frac{RD^{r,i}}{\Delta\rho^*} \quad (3.9)$$

where  $\rho^*$  can be the overall reactivity or the one due to a group of few isotopes, e.g. the reactivity difference only related to fission products ( $\Delta\rho_{FP}$ ).

## Reactivity Loss

At the beginning of the calculation scheme the multiplication factor for the MOC reference calculations is  $k_{infBOC} = 1.54580$ . At the end of the calculations it is  $k_{infEOC} = 1.31601$ . There is a difference  $\Delta\rho = \frac{1}{k_{infEOC}} - \frac{1}{k_{infBOC}} = 11296pcm$ .

This reactivity difference is composed by two parts: one due to the absorption reactivity loss and the one due to the NEXC (nuclear reactions: N2N, N3N, ...) reactivity gain. The former is equal to 11313pcm and the latter to 17pcm. The reactivity gain due to NEXC is, consequently, negligible. Focusing on the reactivity loss due to absorption, this term can be split into three terms: 4669pcm due to actinides (41.26%), 6189pcm due to the fission products (54.72%) and the remaining 455pcm due to the structural materials (coolant and fuel clad) (4.02%). In table 3.5, it is possible to observe a list of all the fission products sorted by order of contribution to the fission product anti-reactivity  $\Delta\rho_{FP}$ . It is important to notice that results not dissimilar to [38] have been obtained. An overall idea of the fission product reactivity loss can be given by figure 3.9. Key Isotopes are:

ACTINIDES:    - U238  
                      - Pu239  
                      - Pu240

STRUCTURES    - Fe56

FISSION        - Pd105  
 PRODUCTS     - Ru101  
                      - Rh103  
                      - Tc99



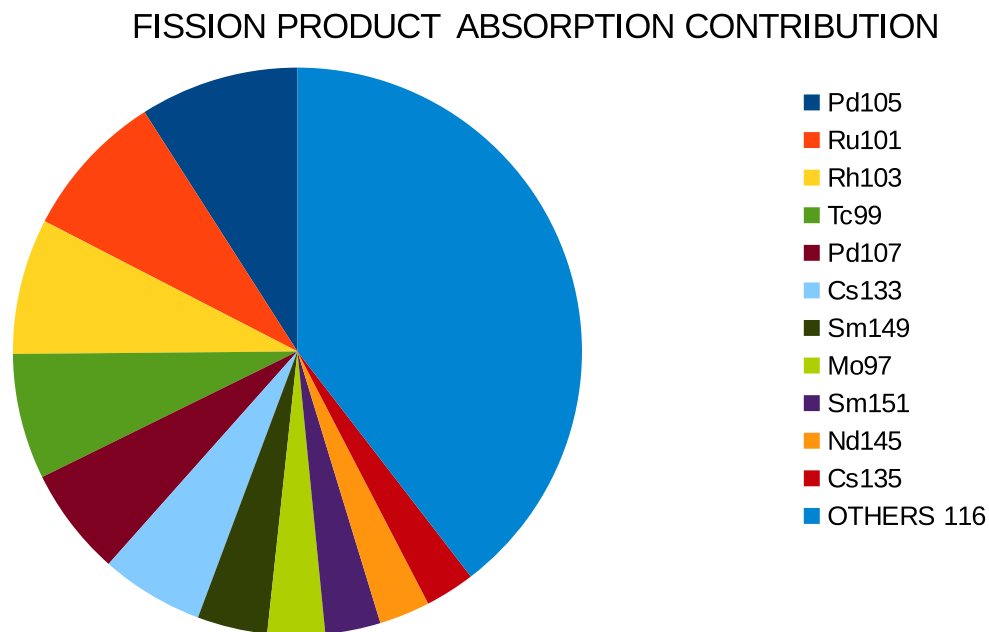


Figure 3.9 Reactivity loss due to fission products

It is now interesting to investigate the reactivity loss due to Fe56. Before doing it, it is important to remind that reaction rates in formula 3.7 are normalized to  $10^5$  neutron source and then divided for the total production. The absorption relative effects of each isotope on the neutron balance, and not their absolute values, are observed. In fact, if a nuclear reactor is operated at constant power without fuel change, the flux, and consequently all the reaction rates of those isotopes whose concentration does not vary, increases with time: fissile material concentrations diminish, then more neutrons are required to obtain the same number of fission. But this happens when the flux is normalized at constant power, not to  $10^5$  neutron source as in this case. Observing Fe56 absorption reaction rate  $\tau_{abs}^{Fe56}$  is equal to 708 at time zero and to 790 at 1440 days. In this case, however, the reactivity difference is reconstructed not considering the absolute number of absorptions per  $10^5$  neutron source, but relativizing it to the secondary neutrons produced. In figure 3.10, it is possible to observe an increase of the relative absorption localized between 1.2-2 keV. Referring to annexe E, it is possible to observe a slight migration of the flux to lower energy. This affects the capture of Fe56. This softening of the flux can be explained with the fact that Pu239 concentration diminishes by 20% with respect to initial concentration. Two concurrent effects take place: the production of fission products, which increase the absorption in the epithermal region

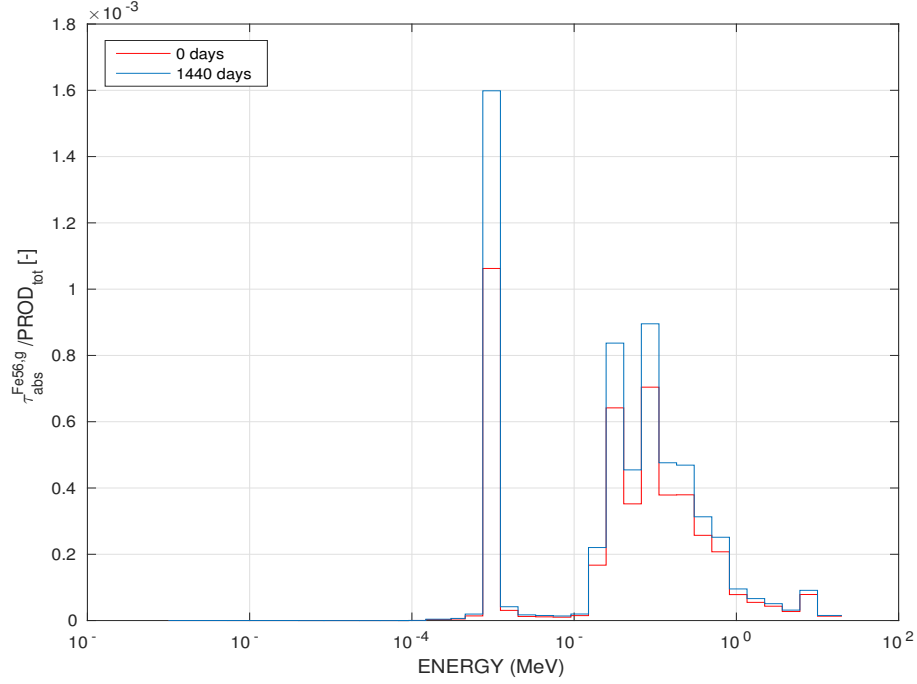


Figure 3.10  $\tau_{abs}^{Fe56g}/PROD_{tot}$  comparison between the beginning and the end of the calculation

(0.1-10 keV), tends to increase the average energy of the neutrons, while the consumption of actinides tends to decrease the absorptions in the same energy region. In this case, the latter is the dominant effect and a flux softening is observed. If an energy condensation of the cross sections is required, a flux shifting means a different weight distribution. A change in flux distribution during the time, for core calculations where energy condensation to 33 groups is performed, means a change in the cross sections to be used. The importance of this change and the effect it can have on the reactivity difference will be the subject of the next section.

Table 3.5 List of all Fission Products by order of contribution to anti-reactivity  $\Delta\rho_{FP}$ 

Contribution in % of $\Delta\rho_{FP}$	
> 1%	Pd105, Ru101, Rh103, Tc99, Pd107, Cs133, Sm149, Mo97, Sm151, Nd145, Cs135, Mo95, Pm147, Ru102, Nd143, Ag109, Ru104, Xe131, Eu153, Sm147, Pd106, Mo100, Mo98, Pr141
0.1 - 1%	Pd108, Zr93, I129, Xe132, Sm152, Xe134, Cd111, Nd146, Eu154, Nd148, I127, Ce142, Nd144, Eu155, Zr91, La139, Cs134, Cs137, Nd150, Zr92, Sm150, Gd157, Ru106, Ru103, Zr94, Ru100, Pd104, Sm148, Rb85, Zr96, Ce140, Gd155, Gd156, Kr83, Pd110, Cd113, Sm154, Nb95, Cd112
0.01 - 0.1%	Ce144, Br81, Te130, Ce141, In115, Tb159, Cd110, Y89, Ba134, Ba138, Sr90, Te128, Pm148M, Eu151, Ba136, Xe136, Kr84, Sb125, Gd158, Pr143, Mo96, Ba137, Nd147, Rb87, Sb121, Zr95, Sb123, Te125, Cd114, Dy161, Se79, Pm149, Gd154, Xe130, Dy160, Ag110M, Mo99, Rh105, Kr85
<0.01%	I131, Nd142, Kr86, Xe133, Gd160, Te127M, La140, Dy162, Dy163, Pm148, Cs136, Te129M, Sr88, Ba135, Ho165, Xe135, Ru105, Dy164, Li6, Eu156, Te131M, Tb160, Er166, Pm151, Sm153, Eu157, I135, Dy165, H3

### 3.2 Core Depletion

The present ECCO/ERANOS calculation scheme for SFR core simulation is composed by the usual two-step scheme: lattice and core. While lattice calculations are performed with 1968 energy groups, core ones use 33 energy group cross sections. Such cross sections, self-shielded and condensed, are evaluated at time zero from 2D ECCO infinite lattice calculations of cells or assemblies (with an infinitesimal concentration of actinides and fission products not present at the initial time). They are then used in 3D ERANOS models to realize full core calculations with a micro-depletion model. This scheme is based on the hypothesis that the 33 energy group microscopic cross sections do not change with the irradiation and the evolution of the composition of the different fissile materials.

The development of a new SFR calculation scheme with APOLLO3 gives us the opportunity to revisit the hypothesis which concerns the core evolution. In fact, other possibilities are present, as the ones used in PWR with the code chain APOLLO2/CRONOS2. The idea is to store self-shielded and condensed macroscopic or microscopic cross sections, parameterizing them in burn-up. These libraries, called “evolving”, are obtained performing depletion calculations at lattice step. They allow, then, the interpolation of the proper cross sections in core calculations. Core evolution can, consequently, be done in 2 ways:

- macroscopic depletion: extrapolating the local burnup variation at each evolution step, the core code performs a linear interpolation of the macroscopic cross sections from the evolving library before evaluating the flux at the new time step.
- micro-depletion: core code solves Bateman equations in order to evaluate isotopic evolution of the nuclei listed in the depletion chain. Used methods are more or less accurate. They have been discussed in section 2.5: constant, linear or parabolic reaction rate extrapolation/interpolation and multistep/monostep methods. Microscopic cross sections are linearly interpolated from the burn-up parameterized evolving libraries.

In the previous chapter, it has been shown that a 1968 group energy mesh does not require the reiteration of the self-shielding during the evolution. This means that microscopic cross sections does not change significantly with the irradiation and the fissile materials’ evolution. Such conclusion must be extended to 33 energy groups and, in addition, homogenized geometry. The aim of the chapter is to compare/validate, on a CFV elementary cell, the 3 evolution methods that can be used for core evolution:

- MACRO: macroscopic depletion
- MICRO SIGMA EVOLVING: micro-depletion with evolving libraries

- MICRO SIGMA ZERO: micro-depletion with time 0 microscopic cross sections.

MICRO SIGMA EVOLVING model is, without a doubt, the more precise. This precision requires more memory storage and time. Cross section libraries must be created. Depletion calculations, consequently, must be performed also at lattice step, differently from the ECCO/ERANOS model. This takes time. The results at each time step must be stored in the parameterized library. This requires memory. It's not without disadvantages that the MICRO SIGMA EVOLVING model- but similarly, with the limitation will see in chapter 5, the MACRO depletion one- is implemented. That's why the possibility of applying MICRO SIGMA ZERO is considered.

The comparison is realized with MINARET - method of the discrete ordinates (see 2.4.7) - on the exact hexagonal cell geometry or the homogenized one. The reference is the MOC APOLLO3 lattice calculation (1968 energy groups) which has created the cross section libraries (self-shielding reiteration of the heavy nuclei only).

The calculations have been done with one fission spectrum only. Consequently, there is no dependence of the fission spectrum from the incident neutron energy. It was not possible, in fact, to perform 4 spectra core calculations at the moment of the study. It is interesting, in figure 3.11, to observe the drift of the reactivity difference between 1 and 4 macro groups during the evolution. This drift is limited to 10 pcm between 0 and 1440 days ( $115000 \frac{MWd}{ton}$ ).

### 3.2.1 Preliminary Studies

#### Validation of the 1968 group micro-depletion

The aim of this section is to verify that the behaviour of the core evolution is similar to the lattice one. For doing so, 2 microscopic cross section libraries, one heterogeneous and one homogeneous, both of them with 1968 energy groups, have been created at time zero and with 1 fission spectrum. They are used to perform the evolution with MINARET core solver. The results are compared with a lattice calculation where self-shielding is not reiterated during the evolution. Microscopic cross sections do not vary. In figure 3.12, the results are shown. At time zero, the reactivity difference is equal to +6 pcm for the heterogeneous case. This difference is related to the fact that TDT-MOC and MINARET solvers do not discretize equally spatial and angular variables in flux evaluation. On the contrary, the homogeneous case present a reactivity difference smaller than 1 pcm. This is related to the fact that the flux is flat and isotropic. The transport equation, then, becomes a balance equation which is necessarily preserved by the flux-volume homogenization.

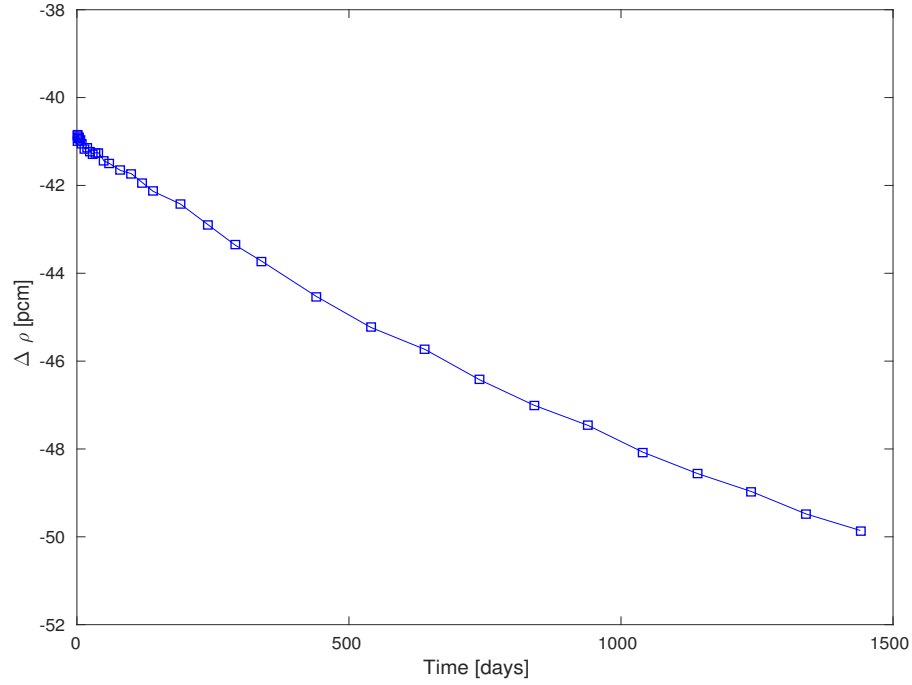


Figure 3.11 Impact of the use of 1 energy independent fission spectrum on the CFV cell  $k_{inf}$  (ref: 4 macro groups of fission spectra)

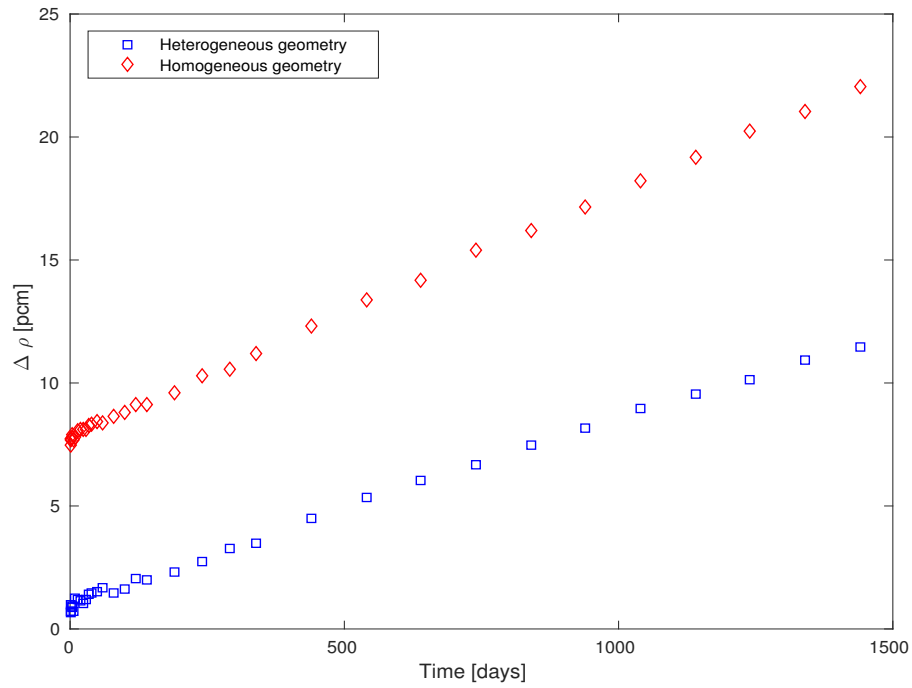


Figure 3.12 MINARET 1968 group “core” calculations compared with reference “lattice” TDT-MOC

During the evolution, the drifts of the reactivity differences are limited to +15 pcm for the heterogeneous case and +10 pcm for the homogeneous one. Concerning the concentrations, the two cases show, for the fission products, a maximum difference of -3.20% for the Sb123. In table 3.5, it has been shown that its contribution to anti-reactivity is smaller than 0.1%. For the actinides, in the heterogeneous case, the difference is limited to -0.53% for Cm246 and it is equal to +0.03% for Pu239.

The concentration differences of the fission products arise from the fission yields. These are defined both for thermal fission ( $< 2.5keV$ ) and fast fission ( $> 2.5keV$ ). While lattice calculations take into account the two groups, the core code uses only the fast one. In table 3.6 and 3.7, it is possible to observe the fission proportions at the beginning and at the end of the calculation. The hypothesis of considering the whole fissions as fast ones seems reasonable. Of course, this approximation introduces errors, as in the case of Sb123. Its difference can be related to the fact that this isotope is principally produced by the thermal fission of Pu239. The same occurs for Gd160 (-3.63%) produced by thermal fission of Pu241. Other isotopes (Dy165, Ho165 and Er166), whose concentrations are smaller than  $10^{17} \frac{atoms}{cm^3}$ , are not correctly estimated (-7.47%, -7.97% and -8.39%).

However, as it is possible to observe from the multiplication factors, the anti-reactivity is correctly represented. The hypothesis is acceptable and this results validate the MINARET solver and the time zero cross section libraries for depletion calculations.

### 33 energy group condensation

It is not possible to perform, with actual technologies, 1968 energy group core calculations. The memory size of the libraries will be unacceptable and the calculation time a limitation. A classical energy condensation to 33 energy groups [25] is done and used for both homogeneous and heterogeneous calculations. In the appendix F, it is possible to observe the energy

Table 3.6 Fission Proportions: Time 0

	Fast	Thermal
Am241	99.41%	0.59%
Pu238	93.40%	6.60%
Pu239	93.67%	6.33%
Pu240	98.70%	1.30%
Pu241	90.77%	9.23%
Pu242	99.73%	0.27%
U235	90.20%	9.80%
U238	99.99%	0.01%

mesh. It is important to notice that cross sections are, by definition, time independent: they represent the virtual surface a nucleus presents to the incident neutron. The larger the surface is, the greater is the probability to react.

In the multigroup approach, however, self-shielding for lattice steps and condensation for core ones introduce a time dependence of the cross sections. They are no more physical quantities; they become flux averaged quantities for particular applications. The finer the energy mesh is, the larger is the range of applications. This is true especially for the input libraries a nuclear code uses. Cross sections are averaged over a flux that is representative of the applications it will be used for. At lattice step, in order to create cross section libraries for core calculations, the actual flux of the cell or of the assembly is used for the condensation. If the energy mesh is coarser, the size of the library is smaller; but the disadvantage is that its application is limited to a flux similar to the one the cross sections have been condensed with. If evolution takes place, a flux shifting can occur, as in this case (see appendix E). This shifting changes the weight function and, consequently, the cross sections. A time zero self-shielded cross section library with 1968 energy groups is capable to reproduce this shifting and correctly estimates the reaction rates which compose the neutron balance. What about a similar library with 33 energy groups? Answering to this question, considering a single cell, is the purpose of this chapter.



Table 3.7 Fission Proportions: Time 1440

	Fast	Thermal
Am242M	90.20%	9.80%
Am243	99.55%	0.45%
Cm242	97.13%	2.87%
Cm243	90.46%	9.54%
Cm244	99.12%	0.88%
Cm245	89.36%	10.64%
Np237	99.91%	0.09%
Np239	100.00%	0.00%
U234	99.68%	0.32%
U236	99.29%	0.71%
Am241	99.33%	0.67%
Pu238	92.74%	7.26%
Pu239	93.04%	6.96%
Pu240	98.51%	1.49%
Pu241	90.05%	9.95%
Pu242	99.68%	0.32%
U235	89.47%	10.53%
U238	99.99%	0.01%

### 3.2.2 Validation: No Leakage Model

In figure 3.13 and 3.14, it is possible to observe the results of the comparison of the 3 models. The reactivity differences between MOC reference case (1 spectrum and self-shielding reiteration of the heavy nuclei only) and the core depletion models is shown. MACRO identifies the macro depletion model; MICRO SIGMA EVOLVING identifies the micro depletion model with the “evolving” cross section libraries (APOLLO2/CRONOS2); MICRO SIGMA ZERO identifies the micro depletion model used in ECCO/ERANOS chain of codes. Two geometries are considered:

- HETEROGENEOUS CASE: the same hexagonal cell geometry of lattice MOC calculations is used. 4 zones are distinguished.
- HOMOGENEOUS CASE: an homogenized hexagonal geometry is used. 1 zone is present.

At time zero, the reactivity difference is equal to +5 pcm for the heterogeneous case. The same difference has been observed in section 3.2.1 and related to a different discretization of the spatial and angular variables in the flux evaluation. At the same time, also the homogenous case shows the same tendency observed in section 3.2.1. The reactivity difference is smaller than 1 pcm. The balance is preserved in the homogenization. This characteristic is maintained during the evolution. At the end of the calculation, for the homogeneous case, the macro depletion model presents a reactivity difference equal to +1.4 pcm.

The other models present a drift. Nevertheless, that is more or less important in one case or another. In the heterogeneous case, the macro depletion model presents a drift equal to +24 pcm. Because the macroscopic cross sections are interpolated from the “evolving” libraries, the difference must be related only to the behaviour of the numerical method used to solve the evolution equations. Concerning the MACRO model, in table 3.8, it is possible to observe an underestimation of the absorption reaction rate of Fe56 (+10 pcm), U238 and Pu239 (+4 pcm). The results present in table 3.8 and 3.9 are obtained using the formula 3.7. The reactivity difference between the reference MOC calculation (state 1) and the MACRO model (state 2) is reconstructed at the end of the calculation.

Moreover, it is possible to compare the reaction rates for the micro depletion models. In this case, the microscopic cross sections are stored. Before passing to the comparison of the absorption reaction rates, a few words must be written concerning the concentration estimation. On figure 3.15 and 3.16, it is possible to observe the time evolution of the relative concentration differences of the 4 fission products which contribute the most to the

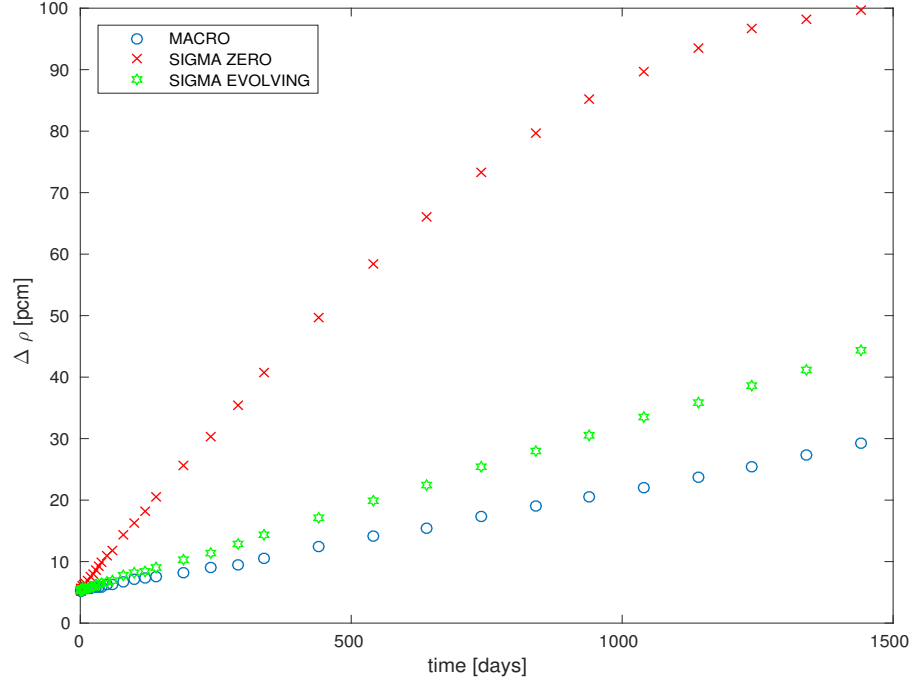


Figure 3.13 Heterogeneous case: CFV cell  $k_{inf}$  comparison between MOC reference and core depletion models

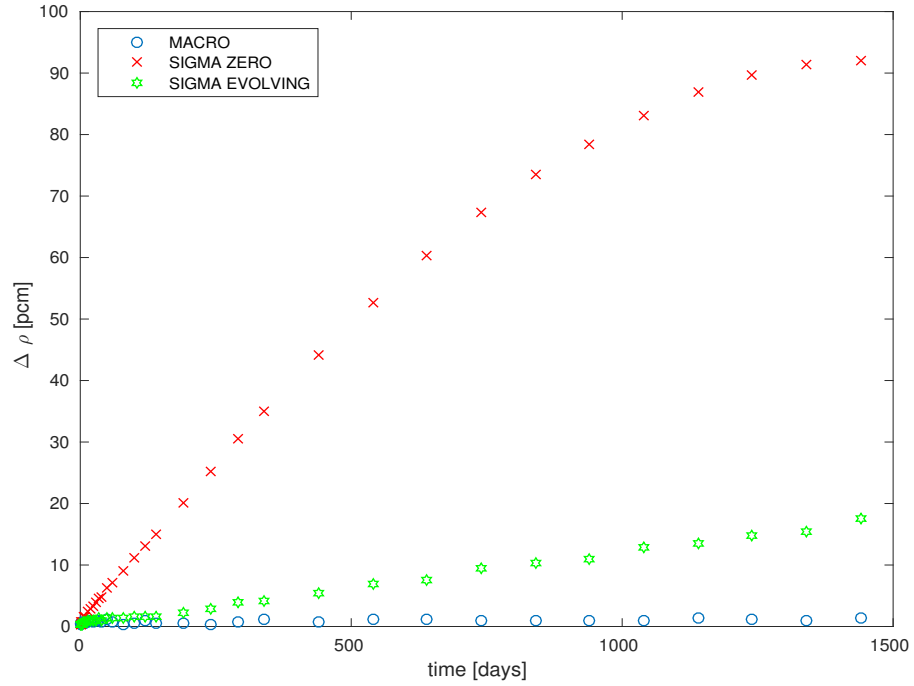


Figure 3.14 Homogeneous case: CFV cell  $k_{inf}$  comparison between MOC reference and core evolution models

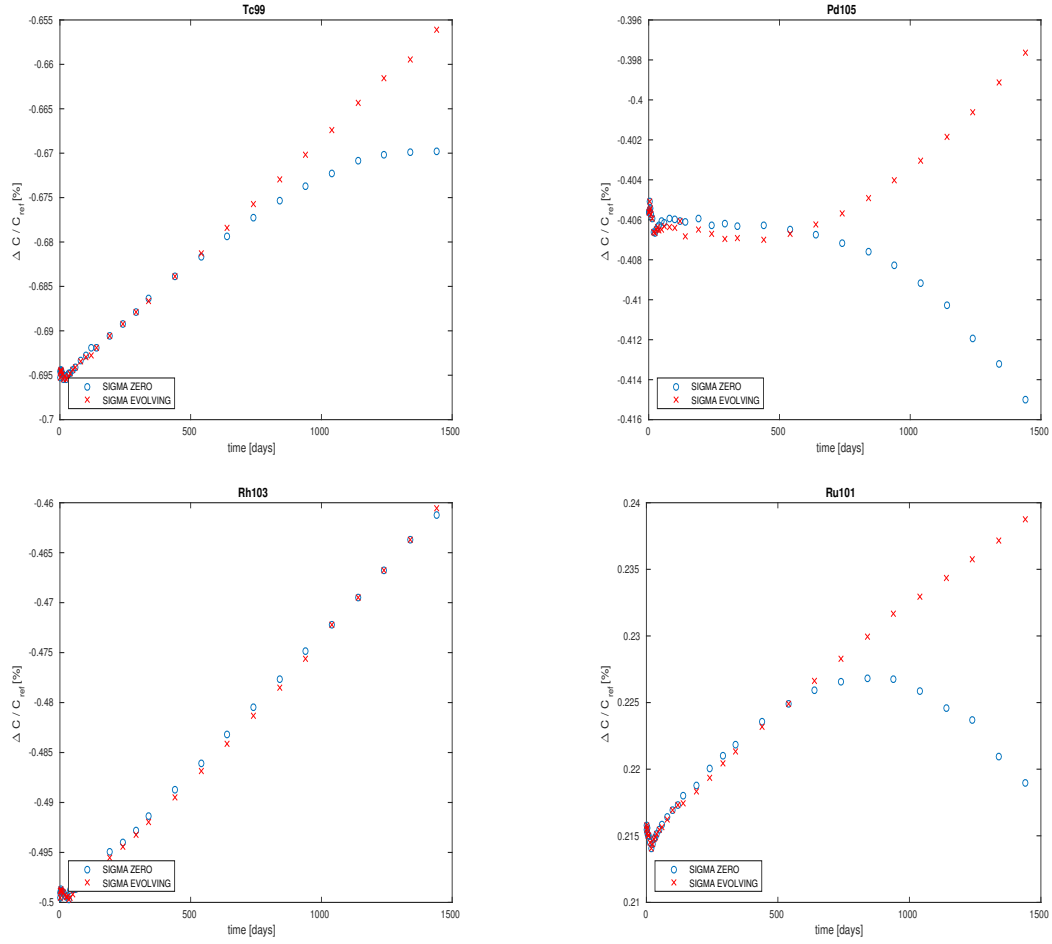


Figure 3.15 Heterogeneous case: Relative difference of the fission product concentrations during the evolution

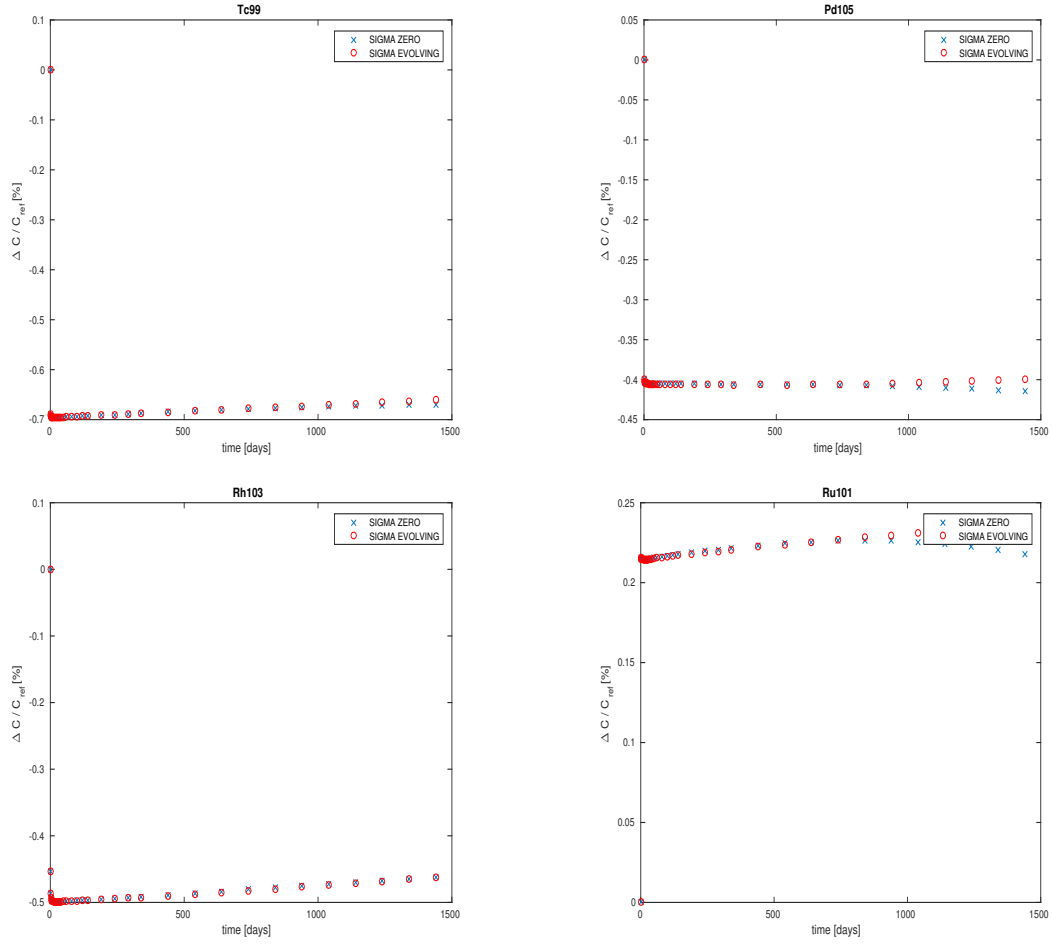


Figure 3.16 Homogeneous case: Relative difference of the fission product concentrations during the evolution

anti-reactivity. These differences are limited to -0.70% (Tc99).

However, the use of only one group fission yields leads to a difference in the estimation of the fission product concentrations. This difference, as discussed in 3.2.1, is around -8% for Dy165, Ho165 and Er166. The contribution to the global anti-reactivity of these isotopes is, after all, limited. Excluding the isotopes listed in 3.2.1, concentration differences are limited to -2.20% for Cd113 in the homogeneous MICRO SIGMA EVOLVING model.

Focusing on the neutron balance at the end of the calculation, it is possible to begin, first of all, considering the flux. In figure 3.17 and 3.18, flux relative differences are shown, normalized to the energy integrated reference flux. In the homogeneous case, MACRO and MICRO SIGMA EVOLVING models do not present any difference. The reactivity difference at the end of the calculation for the SIGMA EVOLVING model is only related to differences in fission product estimation. In the heterogeneous case, this contribution must be added to a drift in the flux evaluation associated with the MACRO depletion model. The drift of the reactivity difference with respect to the initial time for the homogeneous MICRO SIGMA EVOLVING model is equal to +17 pcm; +39 pcm in the heterogeneous geometry.

Concerning the SIGMA ZERO model, the drift is equal to +92 pcm in the homogeneous case; +94 pcm in the heterogeneous one. This drift arises from the fact that reaction rates of U238, Fe56, Pu239, Pu240 and Pu241 are not accurately described (table 3.8 and 3.9).

In figure 3.19, it is possible to observe that the U238 absorption reaction rate is underestimated between 1.2-2 keV by the MICRO SIGMA ZERO model. Because reaction rates are the product of three terms, there are more quantities to consider. First of all, concentrations: U238 concentration is estimated with an error of 0.05%; Pu239 of -0.17%. Concentration difference is not the cause of this underestimation, because an error in the estimation of the concentration results in a scale factor for the reaction rate: all the groups are modified. This is not the case. Then, the flux: a maximum error of 0.04% is made around 100 keV. Between 1.2-2 keV, a strong depression of the flux is not observed. Finally, the microscopic cross sections. These must be the cause of the differences. The softening of the flux, in fact, requires cross sections condensed on softer flux in order not to underestimate the importance of lower energy groups.

As already discussed, this phenomenon has not been observed with 1968 groups. With 33 energy groups, it occurs and introduces a drift. In an global reactivity loss of -11296 pcm the drift represents 0.8% of the total.

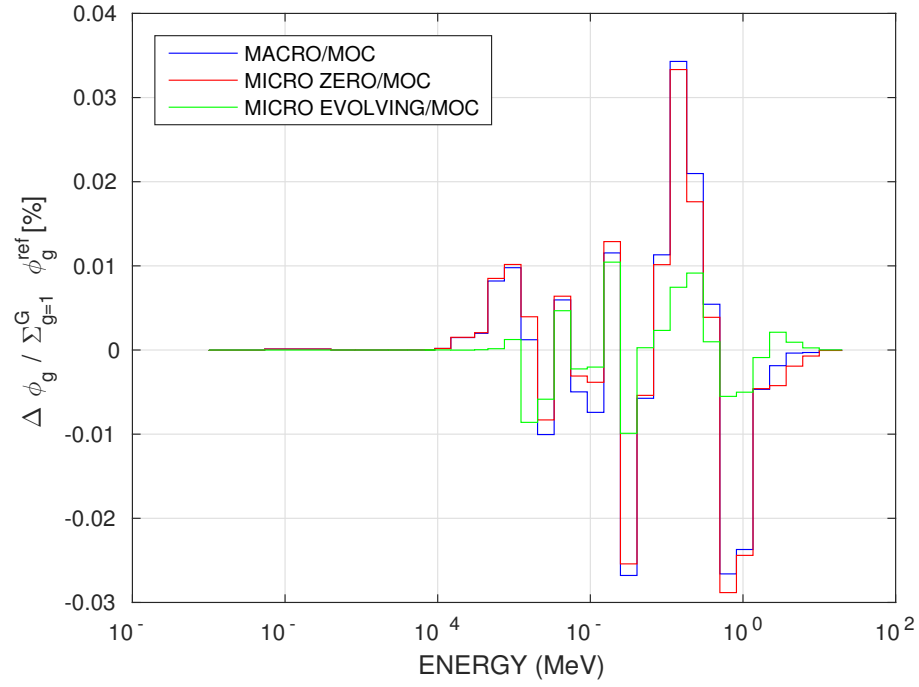


Figure 3.17 Heterogeneous case: CFV cell flux comparison in the fuel region between MOC reference and core depletion models at 1440 days

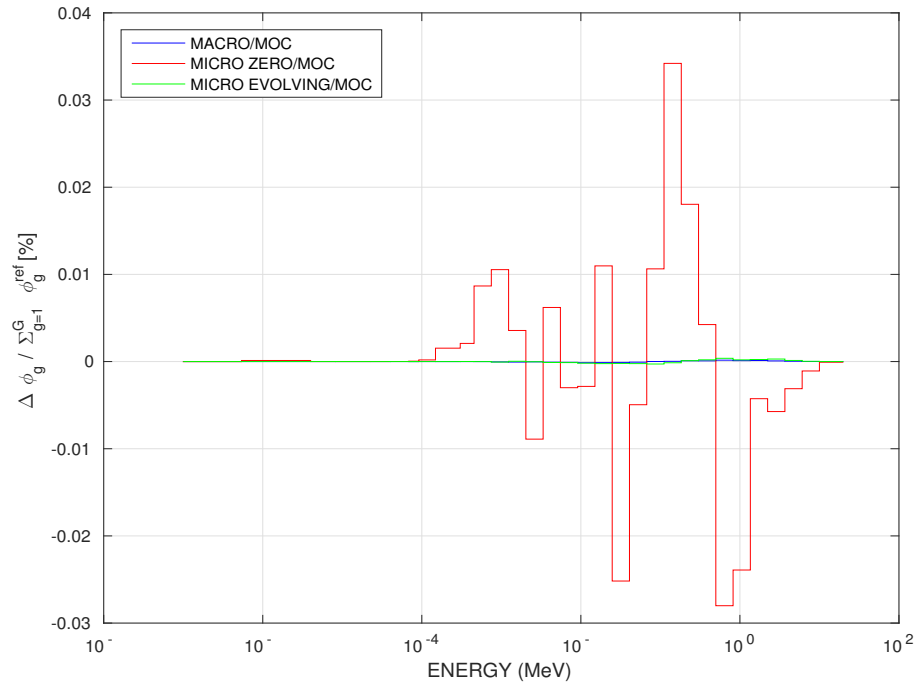


Figure 3.18 Homogeneous case: CFV cell flux comparison between MOC reference and core depletion models at 1440 days

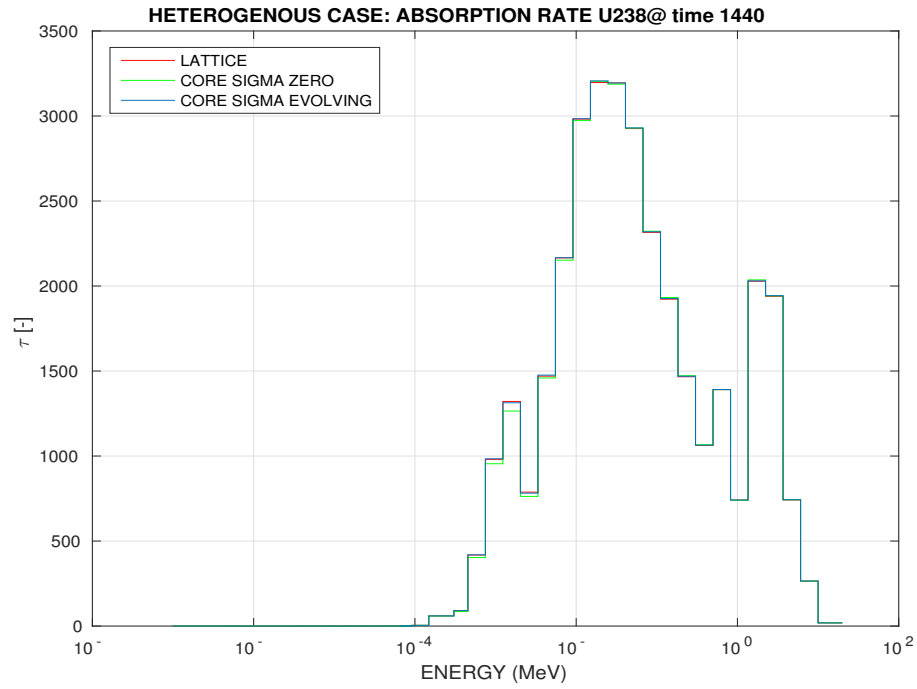


Figure 3.19 Heterogeneous case: comparison of U238 absorption reaction rate in fuel region between MOC reference and core depletion models

Table 3.8 Heterogeneous case: Absorption rate comparison at 1440 days

	MACRO [pcm]	MICRO SIGMA ZERO [pcm]	MICRO SIGMA EVOLVING [pcm]
U238	+4	+124	+5
Pu239	+4	+12	+3
Pu240	+1	-4	+3
Pu241	+0.6	-9	+0.8
Fe56	+10	+7	+10
Tc99	+0.2	+1.5	+3
Ru101	+0.2	-3	-1
Rh103	0	0	+2
Pd105	+0.2	+0.6	+3



Table 3.9 Homogeneous case: Absorption rate comparison at 1440 days

	MACRO [pcm]	MICRO SIGMA ZERO [pcm]	MICRO SIGMA EVOLVING [pcm]
U238	+0.3	+123	+2
Pu239	+0.3	+11	-0.5
Pu240	0	-5	+1
Pu241	+0.1	-9	+0.1
Fe56	0	+7	+0.2
Tc99	0	+1.5	+3
Ru101	0	-3	-1
Rh103	0	0	+2
Pd105	0	+0.6	+2

### 3.2.3 Validation: Leakage Model

In order to subsequently perform full core calculations, leakage models are applied at lattice step. They simulate a finite reactor geometry, even if an infinite lattice is considered. Applying an homogeneous  $B_1$  leakage model to a single cell, a softening of the flux is observed even in this case. The flux softens more in this case with respect to the one without leakage model (see figure 3.20). MICRO SIGMA ZERO, then, is expected to be less accurate in the representation of the time evolution of a cell. Before presenting the values of the multiplication factors, it is important to remind that a leakage model solves the B.15 transport equation. A finite periodic lattice grid, and not an infinite one, is considered. The infinite multiplication factor, then, is just a ratio between neutrons absorbed and produced (neglecting leakage) and do not represent the  $k_{inf}$  of an infinite lattice grid. That's why the infinite multiplication factors of this section and of the previous one are different.

At time zero, the MOC reference calculation presents the infinite multiplication factor  $k_{inf} = 1.72421$  and the effective one equal to unity. At the end of the calculation, the infinite multiplication factor is equal to  $k_{inf} = 1.40024$ . The effective multiplication factor is always equal to unity because the critical buckling is searched. The leakage term diminishes with the irradiation, and the reactivity difference between the infinite multiplication factor at time 0 and after 1440 days is equal to -13419 pcm. The major importance of the softening can be explained by the fact that the introduction of a leakage term reduces the chance of the neutron to be thermalized before escaping. The flux is then harder. Reducing the leakage term during the irradiation tends to soften it. The loss of reactivity and the decrease of Pu239 concentration is another concurrent phenomenon that tends to soften the flux. These two effects synergically reduce the average energy of the flux spectrum, explaining why the relative softening is more important.

Concerning the core depletion model, only the homogeneous geometry is considered, in order to neglect the reactivity difference introduced by the different discretization of the MINARET solver in the heterogeneous case.

In figure 3.21 and 3.22, the results of the models are shown. The effective and infinite multiplication factor are compared with the reference. It is worth underling, before presenting the results of the depletion models, that the leakage model, and so the search of the critical buckling, is applied only at lattice step. Cross sections are then condensed with the evaluated flux and stored in libraries either “evolving” (MACRO, MICRO SIGMA EVOLVING) or not (MICRO SIGMA ZERO). In this case the leakage term  $DB^2$ , that is computed for each time step by the  $B_1$  homogeneous model, is manually added to the transport equation solved by MINARET, in order to have 33 group MINARET calculations analogous to 1968 group MOC ones. Usually, condensed cross sections are directly used in real core geometries

without any leakage term.

Considering the MACRO depletion model, the reactivity differences at the end of the calculation are less than 1 pcm for  $k_{eff}$  and  $k_{inf}$ . The neutron balance is preserved during the evolution. In figure 3.23, it is possible to observe the relative difference in flux distribution, normalized to the reference energy integrated flux. The difference is negligible for the MACRO model. This fact has already been encountered in the previous section.

Focusing now on the concentration at the end of the calculation, major differences arise from the 1 group fission yield approximation. As before, the isotopes listed in 3.2.1 present the most relevant differences. In MICRO SIGMA ZERO depletion model, concentration difference for Dy165 is equal to -5.41%, -2.20% for Sb123 and +1.32% for Cd113. More or less the values observed for the MICRO SIGMA EVOLVING depletion model. However, these isotopes do not affect the neutron balance, and the concentration differences of the 4 most absorbing fission products - Tc99, Ru101, Rh103, Tc99- are limited to -0.47% for Tc99 (see figure 3.24).

Comparing the infinite multiplication factors, the reactivity difference of the MICRO SIGMA EVOLVING model is equal to +16 pcm. It increases to +24 pcm if effective multiplication factors are compared. These differences are coherent with the one observed in the previous section and they are mainly related to the estimation of the fission product concentrations. In table 3.10, formula 3.7 has been used to decompose the reactivity difference of the infinite multiplication factor between the reference MOC calculation (state 1) and the depletion models MACRO, MICRO SIGMA ZERO and MICRO SIGMA EVOLVING (state 2). At the end of the calculation, the concentration difference of U238 is equal to +0.02% for MICRO SIGMA EVOLVING and +0.06% for MICRO SIGMA ZERO. Considering Pu239, +0.03% for MICRO SIGMA EVOLVING and -0.16% for MICRO SIGMA ZERO.

Nevertheless, their contribution to the reactivity difference of the infinite multiplication factor is relevant, as it is possible to see in table 3.10. These differences, and the flux distribution ones (see figure 3.23), can be eliminated using an “evolving” cross section library. It is important to notice that differences are larger if the leakage model is applied, increasing the flux softening phenomenon.

In an overall reactivity loss of -13419 pcm, the drift represents 2% of the total.

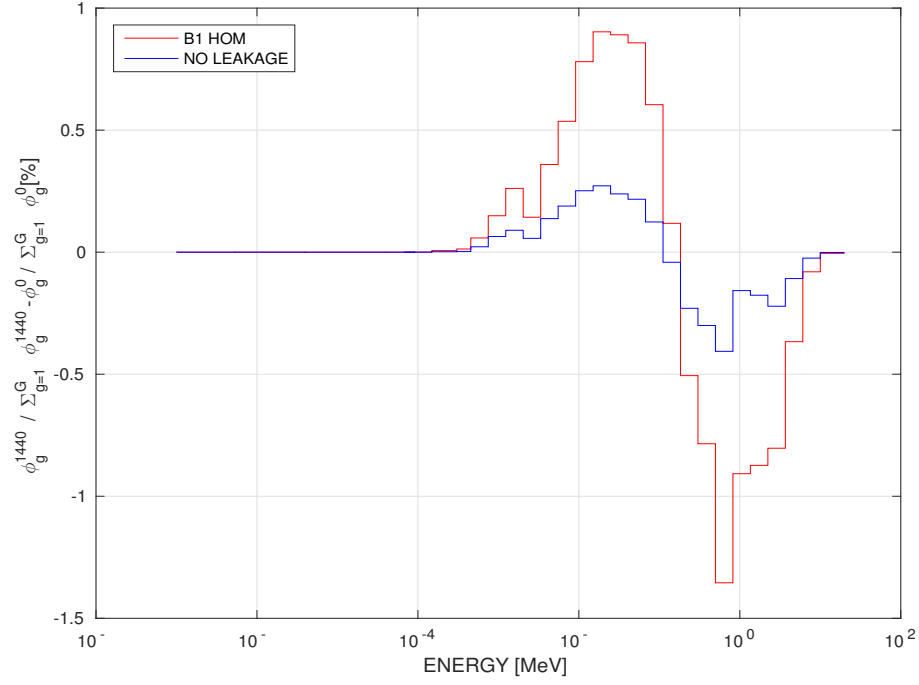


Figure 3.20 Relative spectrum variation of the fuel flux within 0 and 1440 days for CFV cells with or without leakage.

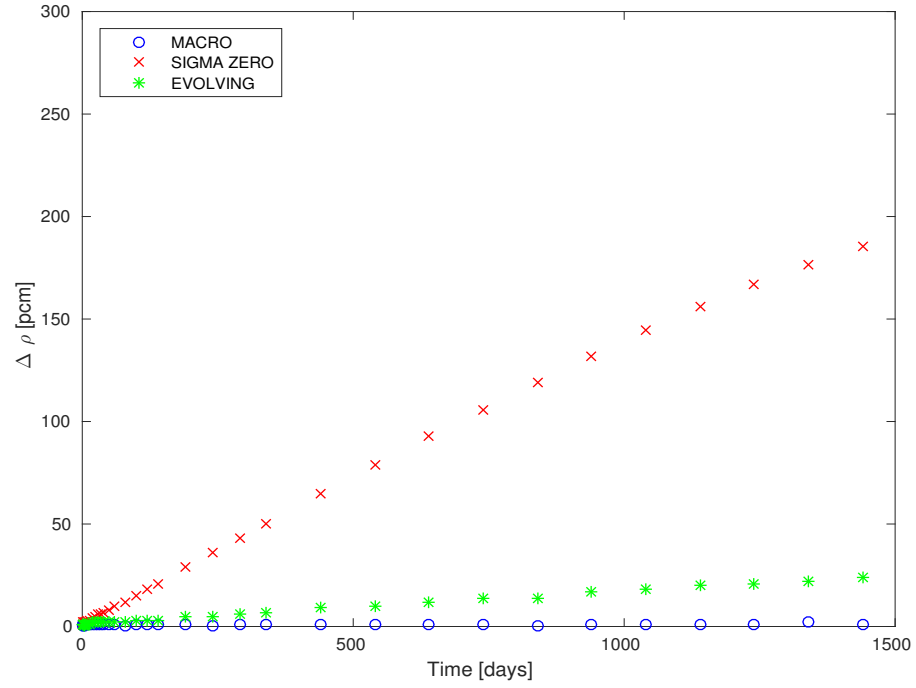


Figure 3.21 Leakage case: CFV cell  $k_{eff}$  comparison between MOC reference and core evolution models

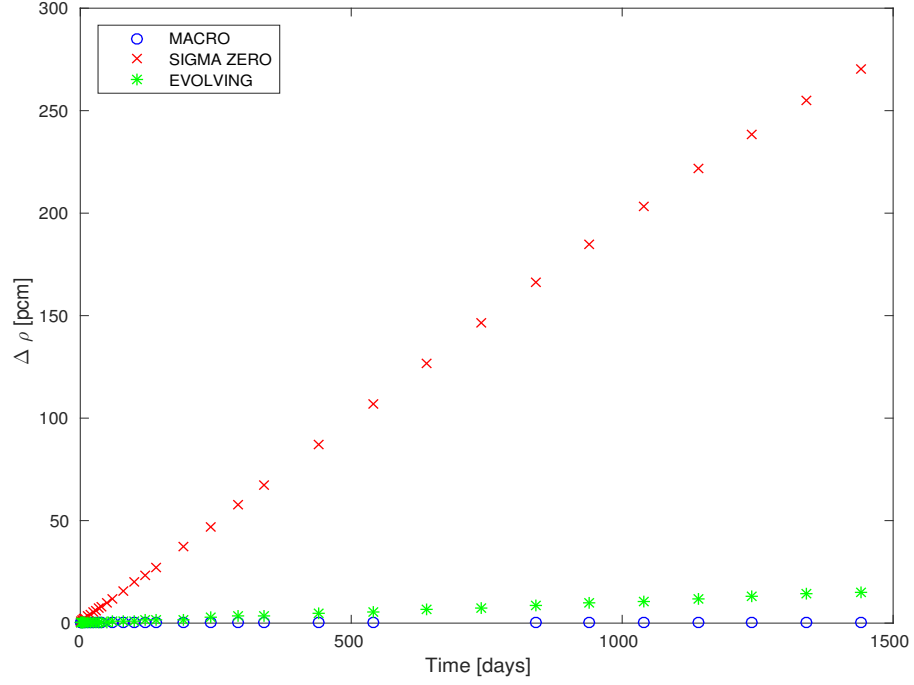


Figure 3.22 Leakage case: CFV cell  $k_{inf}$  comparison between MOC reference and core evolution models

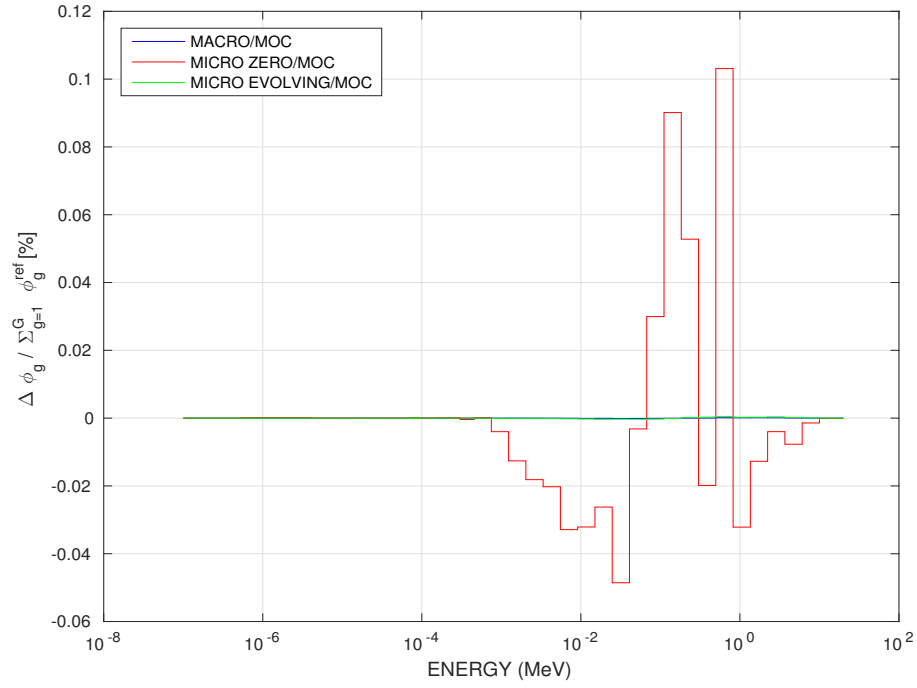


Figure 3.23 Leakage case: CFV cell flux comparison between MOC reference and core depletion models at 1440 days

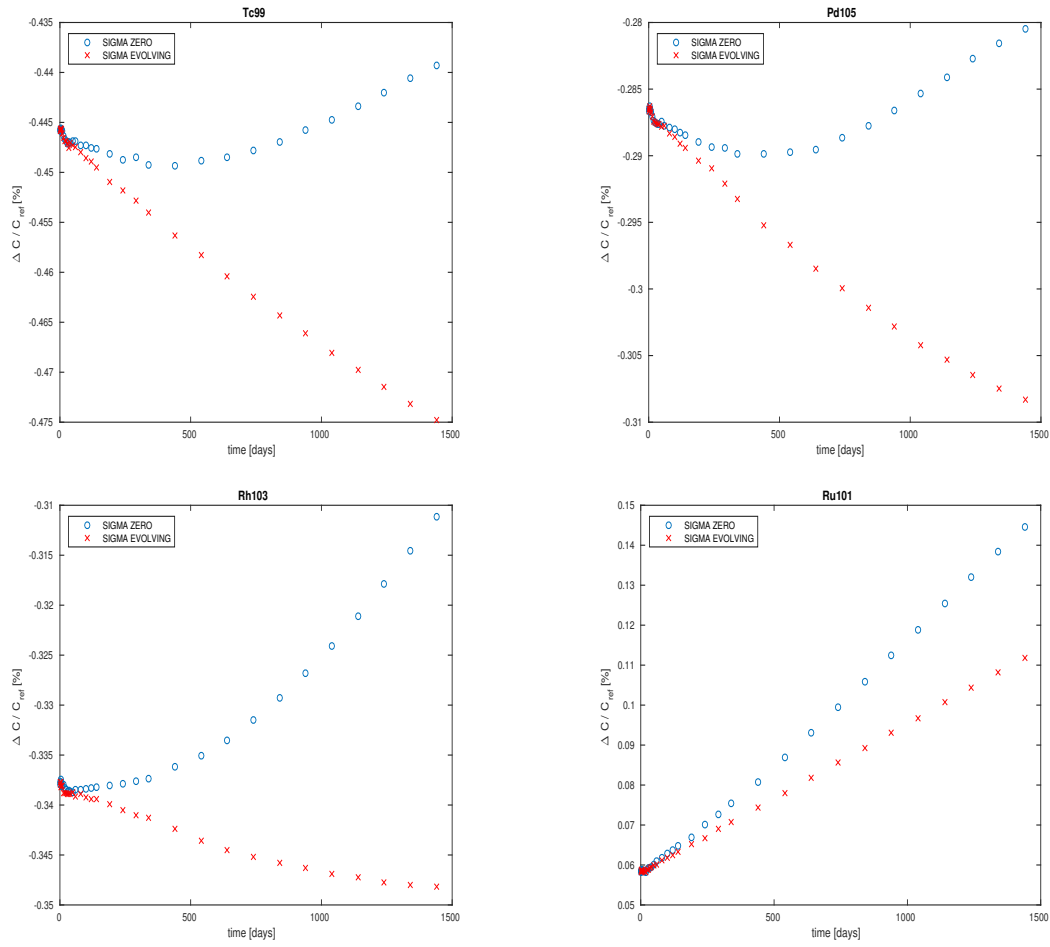


Figure 3.24 Leakage case: Relative difference of the fission product concentrations during the evolution

Table 3.10 Leakage case: Absorption rate comparison at 1440 days

	MACRO [pcm]	MICRO SIGMA ZERO [pcm]	MICRO SIGMA EVOLVING [pcm]
U238	+0.1	+165	+3
Pu239	+0.2	+60	-0.2
Pu240	0	+10	+1
Pu241	0	+6	-0.1
Fe56	0	+6	+0.2
Tc99	0	+3	+2
Ru101	0	+0.7	-0.4
Rh103	0	+2	+2
Pd105	0	+3	+2

### 3.3 Burn-up parametrization of the cross section libraries

In the previous section, it has been shown the importance of the cross section time dependency for core calculations. In a cell case, where no leakage model is applied, the MICRO SIGMA ZERO model leads to a reactivity difference of the order of 100 pcm (0.8% of the overall reactivity loss). The flux shifts towards lower energy and the cross sections are not condensed using the proper time-dependent weight flux. Until now, the MICRO SIGMA EVOLVING model has used a cross section library with a number of burn-up tabulation points equal to 34. The lattice depletion is performed following the time steps enlisted in the table of appendix C. 33 time intervals  $\Delta t$  are used in lattice depletion. These intervals are accurate to represent, during the evolution, actinide and fission product concentrations. The correct representation of Np239 equilibrium concentration, for instance, explains the high number of time steps at the beginning of the calculations. Actinides and fission products are correctly estimated and this fact allows to properly represent the reactivity variations. Nevertheless, the aim of lattice calculations is the creation of cross section libraries and not the correct representation of isotope concentrations. As a consequence, the number of time intervals can be diminished in lattice depletion calculations. In fact, it is not important, at lattice step, to correctly represent the reactivity variations and time intervals can be reduced in order to create cross section libraries with a coarser burn-up mesh parametrization. The goal is to provide a cross section library which is more accurate than the MICRO SIGMA ZERO one, but which does not require a number of lattice steps equal to 34 to be created. Concerning TDT-MOC 1968 energy group lattice calculations, evolution time intervals  $\Delta t$  have been consecutively divided by 2, from 33 to 16,8,4,2 and, finally, to a single interval covering the evolution from 0 to 1440 days. Corresponding cross section libraries have been created. Constant integration scheme has been used in order to avoid negative values for the reaction rates. Convergence test has not been performed in order to avoid the division of the time interval by 2.

From cross section libraries with 34, 17,9,5,3 and 2 tabulation points, core depletion is performed: 33 energy group MINARET calculations for an homogeneous cell geometry and 33 evolution time intervals  $\Delta t$ . A monostep calculation with a linear extrapolation/interpolation of the reaction rates is used by the depletion solver.

The results are shown in figure 3.25. Only one time interval  $\Delta t$  from 0 to 1440 days is required to obtain, with a difference of few pcms, the results of the MICRO SIGMA EVOLVING using 33  $\Delta t$ . With respect to a MICRO SIGMA ZERO model whose difference at the end of the calculation is equal to +92 pcm, the model using a 2 points cross section library gives a final difference equal to +23 pcm (only +5 pcm higher than MICRO SIGMA EVOLVING).

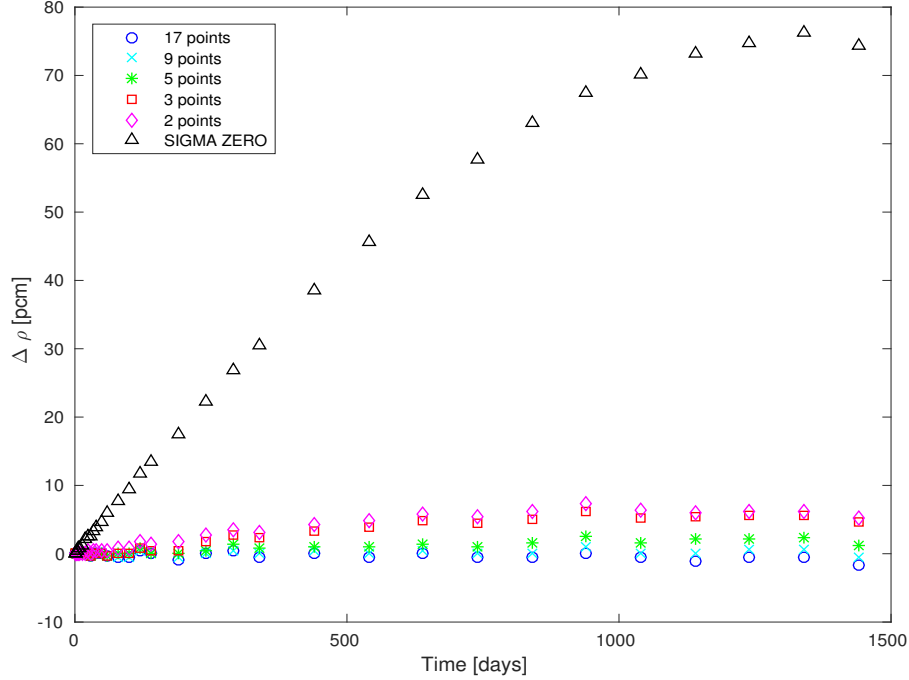


Figure 3.25 Homogeneous case without leakage: CFV cell  $k_{inf}$  comparison between 34 point MICRO SIGMA EVOLVING calculation and core evolution models with 17, 9, 5, 3, 2 burn-up tabulation points in the cross section libraries or only 1 (SIGMA ZERO).

Time and memory are saved without reducing the accuracy of the results. This remarkable result, which can be explained by the great linearity of the phenomenon, justifies the use of a burn-up parametrization of the cross sections in the SFR project calculation scheme with APOLLO3.

### 3.4 Conclusions

In this chapter, a CFV cell geometry charged with MOX fuel has been studied. In the first section, APOLLO3 lattice calculation options have been investigated. Indications have been provided about the correct temporal evolution scheme and the necessity of repeating or not self-shielding calculations. Then, an inter-code validation has been performed between APOLLO3, TRIPOLI4 and ECCO/ERANOS neutronic codes. The results have been shown to be coherent and sensitive to the fission spectra used. Before passing to core depletion, a reactivity analysis has been done in order to underline the isotopes which contribute the most to the reactivity loss. Considering the actinides, these isotopes are U238, Pu239; Pd105, Ru101, Rh103 and Tc99 are the most reactive fission products.

In the second section, three depletion models have been presented and compared. Two of



them are actually used in thermal reactor simulations: the MACRO depletion model and the MICRO SIGMA EVOLVING one. The other one is currently used in ECCO/ERANOS SFR calculation schemes: the MICRO SIGMA ZERO depletion model. Although this model is more rapid and less memory demanding, it overestimates by around 100 pcm ( $\sim 0.8\%$  of the overall reactivity loss) the final reactivity difference in a case where no leakage model is applied. If a leakage model is applied, this difference doubles.

In the last section, in order to reduce the calculation time and the memory storage required, a study on the number of burn-up tabulation points in cross section library is performed. The MICRO SIGMA EVOLVING model is applied using cross section libraries different from the ones created in the reference calculations. The high linearity of the phenomenon allows to use only two tabulated points in the libraries: the one at the beginning and the one at the end of the calculations. The small reactivity difference justifies the use of a burn-up parametrization against a SIGMA ZERO model: an higher accuracy is obtained without significantly affecting the calculation time and the memory storage, which are only doubled.

## CHAPTER 4 EVOLUTION OF A FISSILE-FERTILE CLUSTER GEOMETRY

The previous chapter has presented a certain number of elementary validations on the CFV cell case. The aim of these validations is to select the right parameters in order to perform depletion calculations where the reactivity difference is reduced to minimum, while calculation time and memory remain affordable for industrial applications. This part wants to confirm these choices on a more demanding geometry: a cluster composed by a fertile assembly surrounded by 6 fissile semi-assemblies. Due to the symmetries of the cluster, 1/12 of it is considered as a calculation motif (see figure 4.1). The fissile material is charged with MOX fuel, as in the cell case; the fertile one with depleted UOX (0.2% weight enrichment in U235). An hexagonal tube, composed of a steel alloy, surrounds each assembly.

The chapter is divided in two parts: the first dealing with lattice evolution; the second presenting the results of the core depleting models discussed in the previous chapter:

- MACRO
- MICRO SIGMA EVOLVING
- MICRO SIGMA ZERO

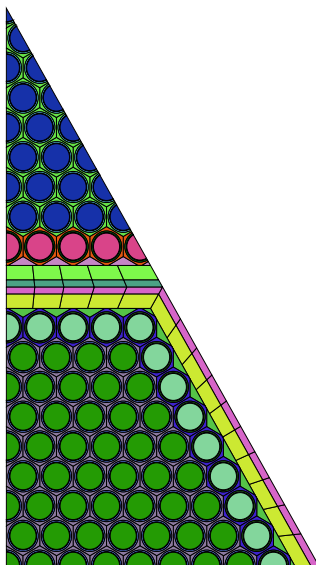


Figure 4.1 1/12 cluster fissile-fertile geometry

It is important to notice that all the depletion calculations are made with the parameters previously defined (see section 3.1.1):

- linear extrapolation/interpolation of the reaction rates
- multistep method for lattice depletion; monostep for core one
- reiteration of the Tone self-shielding method of the heavy nuclei
- 1 macro group of fission spectrum

Both lattice and core calculations are performed with specular reflective boundary conditions. It is worth reminding that, while lattice depletion is performed with two fission yield groups (a fast and a thermal group), core depletion is performed using the fast fission yield group only.

## 4.1 Lattice Depletion

Before comparing the results of the core depletion models, it is important to discuss the evolution geometry for lattice depletion. Concerning the self-shielding, for each assembly two calculation zones are distinguished: one zone including the outer ring, the other composed by all the inner rings. In figure 4.1, it is possible to identify the two zones by the different colours used. This calculation geometry has been validated for static calculations [41]. The purpose here is to validate the geometry for depletion calculations. In fact, during the evolution, asymmetries can arise due to concentration variations. Consequently, at first, a reference evolution geometry is introduced: each fuel pin is distinguished and separately evolved.

### 4.1.1 Reference Evolution Geometry

The infinite multiplication factor at time zero is equal to 1.28212. The energy integrated flux distribution is represented in figure 4.2. The flux is normalized to  $10^5$  neutron production. It is possible to observe that the flux is higher in the fissile region than in the fertile one; but, inside the assemblies, flux differences are limited. The flux distribution is more or less flat, explaining why only 2 self-shielding regions are required. Differences are located principally in the external ring. This distribution also explains why it's not necessary to self-shield at each time step for 1968 energy group calculations (see 3.1.1) and why, differently from PWR, only 1 region is used to self-shield the fuel (no rim-effect, see appendix A).

After 1440 days, the multiplication factor becomes 1.16629. The reactivity loss is equal to 7746 pcm. Its decomposition will be performed in the following paragraph. For the moment,

it is important to observe the energy-integrated flux distribution in figure 4.3. No major asymmetries arise in the flux distribution due to depletion. The maximum and the minimum values are located in the same cells, but the relative differences with respect to the average values have diminished. Flux distribution is further flatten. The assembly-averaged flux is smaller in the fertile region than in the fissile one, but also this difference is reduced with respect to time 0.

Concerning the isotope concentrations, during the evolution, actinides are produced and burnt both in fissile and fertile regions. At 1440 days, however, actinides have globally diminished in the fissile region and increased in the fertile one. Fission products are produced everywhere, even if mostly in the fissile region where the number of fissions is higher. In figure 4.4 and 4.5, it is possible to observe the concentration maps, at the end of the calculation, for Pu239 and Pd105. Pu239 is burnt more or less uniformly in the fissile. In the fertile, the production is more important on the external ring where the flux is higher. Focusing on Pd105, then, the same uniformity in the production is observed in the fissile region, while in the fertile one this is not completely true. In the external ring, Pd105 concentration is +2.63% higher than the average. However, no notably asymmetries are observed. In 4.1.3, it

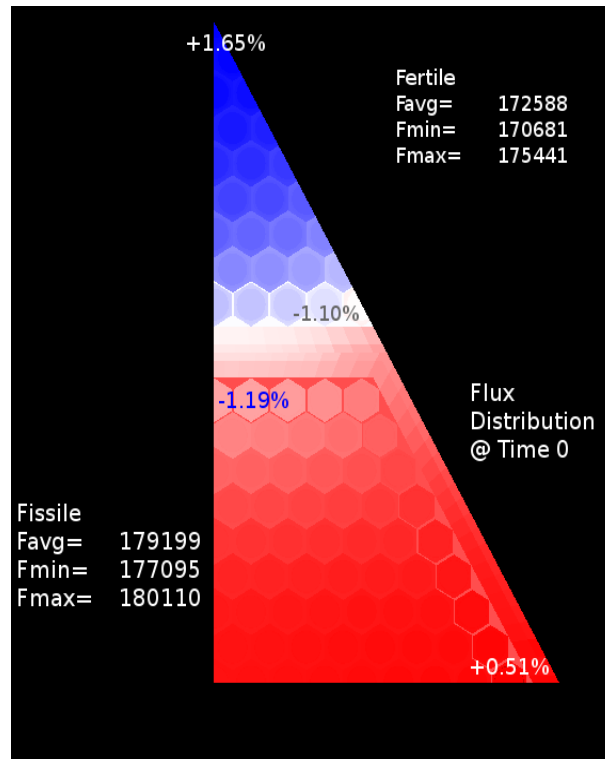


Figure 4.2 Reference Evolution Geometry - Flux distribution at  $t = 0$  days (normalized to  $10^5$  neutron production)

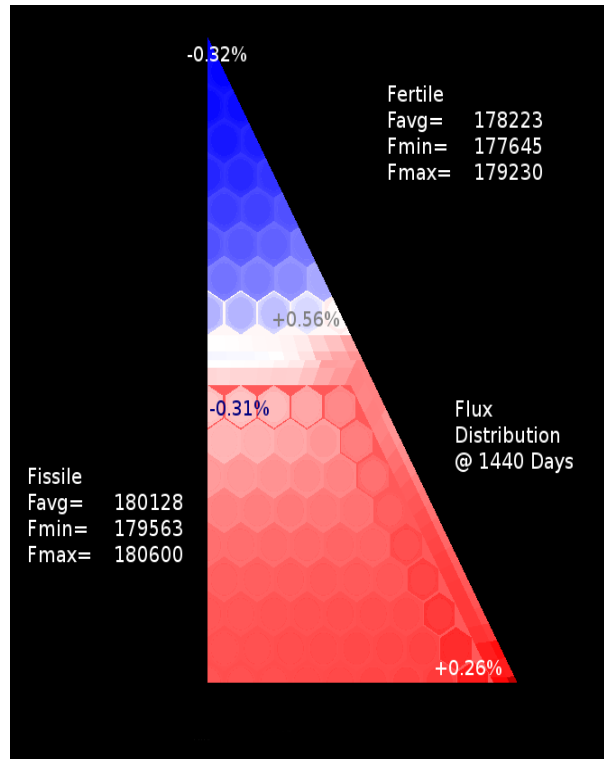


Figure 4.3 Reference Evolution Geometry - Flux distribution at  $t = 1440$  days (normalized to  $10^5$  neutron production)

will be possible to comment on the results stemming from the application of the self-shielding geometry for depletion calculations.

The flux distribution observed in figure 4.2 and 4.3 are integrated over the whole energy domain. Integrating the flux over the assembly, on the other hand, can highlight the presence of a flux shifting in the fissile or fertile region. In figure 4.6, it is possible to observe the flux differences normalized to the initial energy-integrated flux value. In the fertile region, an hardening of the flux is observed. The production of Pu239 and fission products, which are thermal absorbers, increases the average value of the flux energy. In the fissile region, a slight softening of the flux is observed. This softening is smaller than the one observed in the cell case.

Before treating the simplified evolution geometry, consisting of only two evolution regions actually used only for self-shielding, a reactivity study is accomplished in order to decompose the reactivity loss.

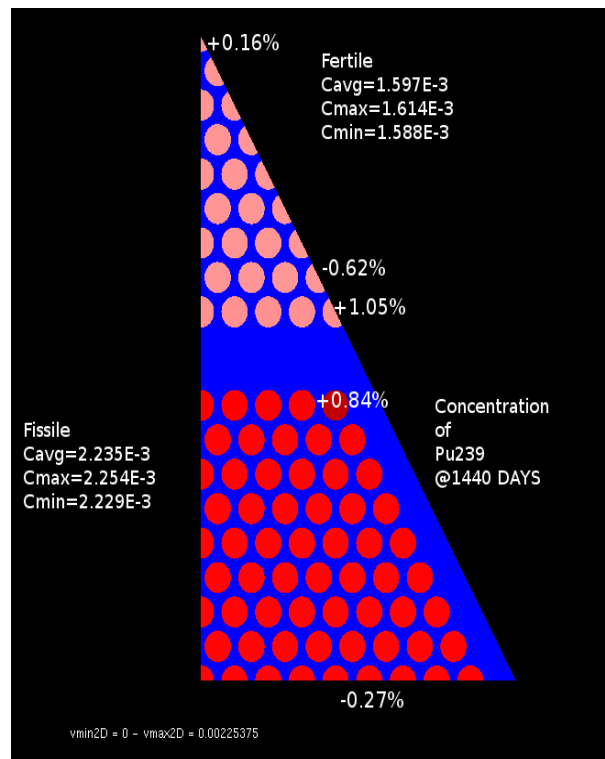


Figure 4.4 Reference Evolution Geometry - Pu239 distribution at  $t = 1440$  days

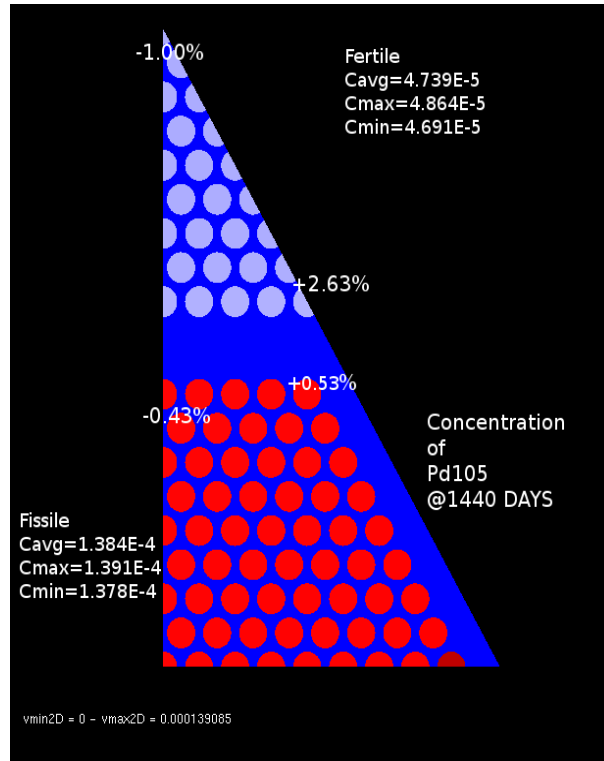


Figure 4.5 Reference Evolution Geometry - Pd105 distribution at  $t = 1440$  days

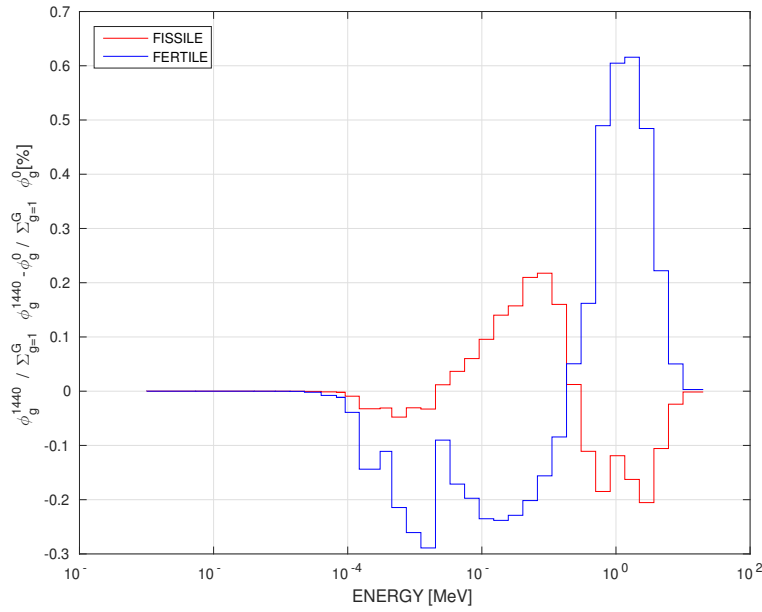


Figure 4.6 Reference Evolution Geometry - Relative flux difference between BOC and EOC

### 4.1.2 Reactivity Decomposition

The overall reactivity loss is equal to 7746 pcm. Formula 3.8 decomposes the loss, so that it can be related to certain reactions and isotopes. First of all, the reactivity loss due to absorption is equal to 7753 pcm, while the reactivity gain due to (n,Xn) reactions is equal to 7 pcm. Then, after decomposing the loss due to the absorption term, it is possible to observe the results in table 4.1. The total actinide contents decrease in the fissile region and increase in the fertile one. Nevertheless, at the end of the calculations, the fissile material contents globally diminish. Consequently also their contribution to the relative absorption diminishes, resulting in a reactivity gain of 127 pcm. The reactivity loss is principally due to the fission products: -6956 pcm (89.80%). The major part of this loss is related to the absorption in the fissile region (-6145 pcm, 88.34%). In figure 4.7 and 4.8, it is possible to observe the contribution of the most absorbing fission products to the reactivity loss, both for the fissile and fertile region. The hierarchy is similar to the one tabulated in 3.5.

Concerning the absorption due to structural materials, most of it is due to the softening of the flux in the fissile region (790 pcm, 85.5%). The importance of the structural materials in the neutron balance has already been discussed in section 3.1.3. The same considerations apply for this geometry.

Finally, in order to underline the importance of actinides production, the infinite multiplication factors of the fissile and fertile regions are presented. In this case, the adjective infinite is not particularly appropriate. An infinite lattice grid of the fissile and fertile assemblies is not considered. The neutron balance is just accomplished accounting the reactions in the two regions independently. For region  $x$ , the infinite multiplication factor is evaluated separately from the other regions:

$$k_{inf}^x = \frac{PROD_x}{ABS_x - NEXC_x} \quad (4.1)$$

where the superscript  $x$  underlines that only rates of isotopes in  $x$  are considered.

$k_{inf}^{fissile}$  is equal to 1.45610 at the beginning of the calculation. The depletion leads to a

Table 4.1 Reactivity loss decomposition at 1440 days

	$\Delta\rho[pcm]$	rel
ACTINIDES	+127	+1.64%
FP	-6956	-89.80%
STRUCTURES	-924	-11.93%
ABSORPTION LOSS	-7753	-100.09%
NEXCESS GAIN	-7	-0.09
OVERALL LOSS	-7746	-100%



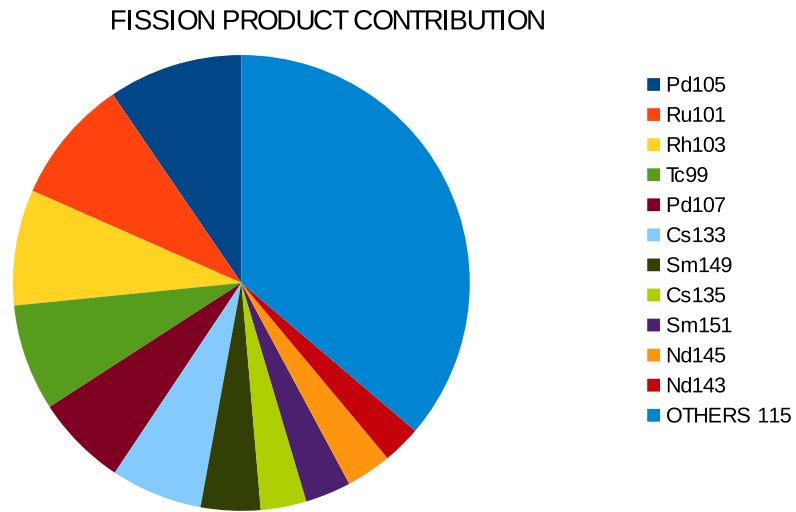


Figure 4.7 Reference Evolution Geometry - Reactivity loss due to fission products in fissile region

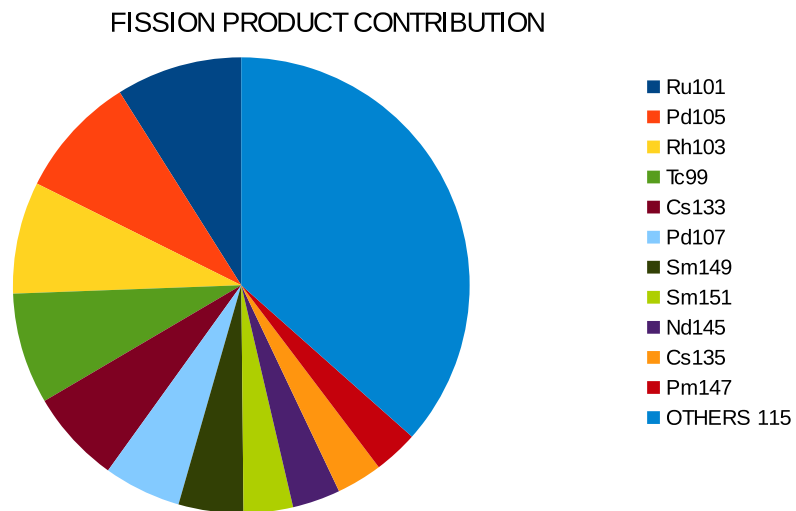


Figure 4.8 Reference Evolution Geometry - Reactivity loss due to fission products in fertile region

multiplication factor equal to 1.22244. As expected, the fissile region loses reactivity. The fertile one, on the other hand, gains some. At the beginning, the multiplication factor is equal to 0.22905; then, after 1440 days, it is equal to 0.95034.

### 4.1.3 Simplified Evolution Geometry

The evolution geometry used till now is replaced with the self-shielding one. For each assembly only 2 evolution zone are identified: one composed by the outer cell ring, the other by the internal rings. In section 4.1.1, it has been demonstrated that during the evolution no major asymmetries arise. This assumption is further supported by figure 4.9: the reactivity difference between the reference evolution geometry and the simplified one is smaller than 1 pcm during the evolution.

Comparing the assembly-averaged concentrations, the maximum difference is equal to -0.23% for Cm247 in the fissile region; equal to +0.22% for Ba135 in the fertile one.

At the end of the calculation, the isotope concentrations are well estimated and the reactivity difference is equal to 0.7 pcm, even if a major simplification of the evolution geometry has been done. The advantage of this simplification is the possibility of creating evolving cross section libraries reducing heavily the time calculations and without affecting the accuracy.

In the next part, in fact, core depletion will be discussed.

## 4.2 Core Depletion

The geometry that will be used in the following calculations is represented in figure 4.10. Fissile and fertile assemblies are homogenized and 2 zones are identified: the fissile one (in blue) and the fertile one (in red).

Calculations will be performed with 33 energy groups in order to compare the depletion models, as in the cell case. The simplified evolution geometry is used for the creation of the cross section libraries, both for the fissile region and the fertile one. Core calculations will be compared to the reference one. As it will be explained in 5.2, in the actual SFR ECCO/ERANOS core calculation scheme, fissile cross sections are not evaluated, at a lattice step, accounting for the surrounding materials (the presence of the fertile assembly in this case). An infinite lattice of fissile assemblies is considered to create the cross section libraries. In this part, the effect of this approximation won't be taken into account, but it will in section 5.4.

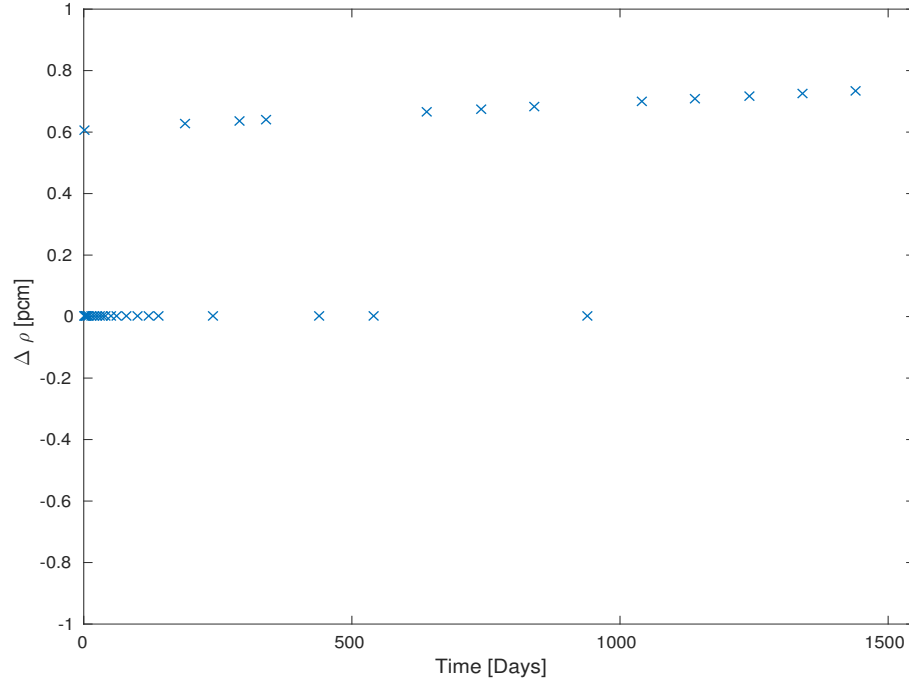


Figure 4.9 Fissile-Fertile Cluster  $k_{inf}$  comparison between the reference evolution geometry and the simplified one

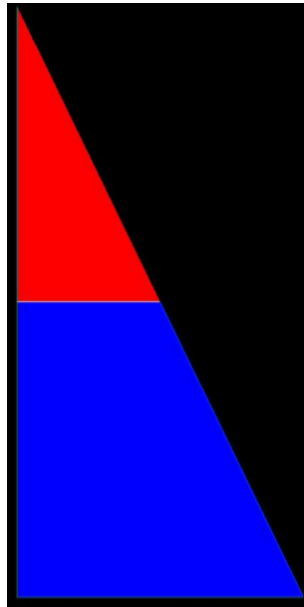


Figure 4.10 Homogenized core geometry representing 1/12 fissile-fertile cluster

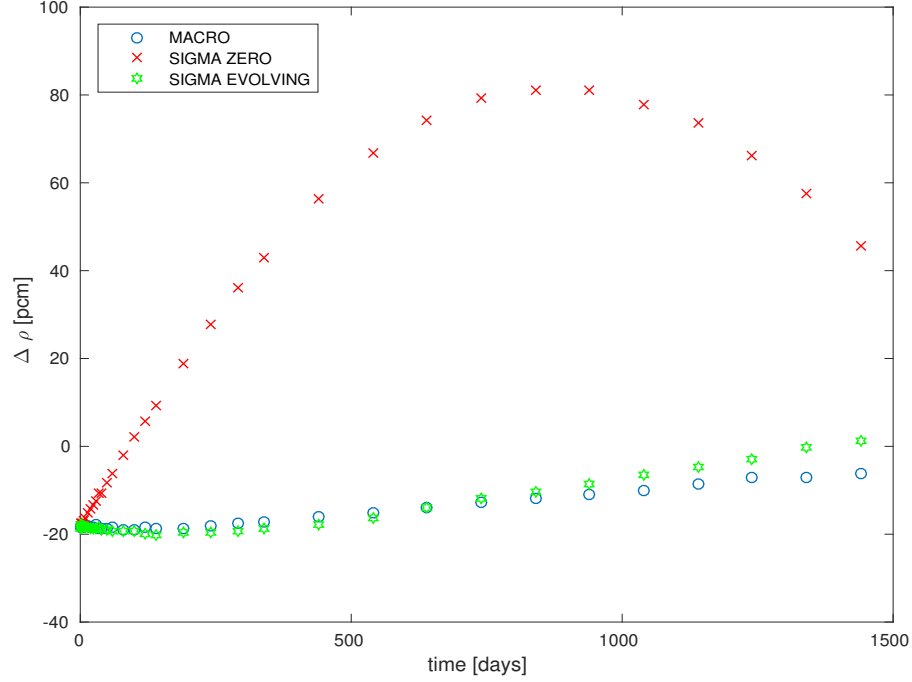


Figure 4.11 Fissile-Fertile Cluster  $k_{inf}$  comparison between MOC reference and core evolution models

#### 4.2.1 Comparison of the Depletion Models

In figure 4.11, it is possible to observe the reactivity difference between the core depletion models and the reference calculation. At time 0, the multiplication factor obtained with MINARET is equal to 1.28182. The reactivity difference compared with the reference is equal to -18 pcm.

In table 4.2, it is possible to see the decomposition of the difference. The values proposed are obtained with formula 3.7. The underestimation of 18 pcm is due to a slight overestimation of Pu239 and U238 absorption in the fissile region, not totally compensated by a corresponding absorption of these isotopes in the fertile region.

This fact is principally due to the homogenization/condensation. Following the evolution

Table 4.2 Fissile-Fertile Cluster: Time 0 Absorption Comparison: homogeneous MINARET at 33 groups/ heterogeneous reference TDT-MOC (in pcm)

NUCLEUS	FISSILE ASSEMBLY	FERTILE ASSEMBLY
U238	-11	+17
Pu239	-22	0
Pu241	-6	0

of the MACRO depletion model, it diminishes with time. At the end of the calculation, the absorption difference of Pu239 and U238 are limited and globally compensated, as it is possible to observe in table 4.3. The reactivity difference is equal to -6 pcm. Even in this case, a little overestimation of the absorption in the fissile region, which does not overcome -8 pcm for Pu239, is present. Differently from time 0, a compensation with the fertile region is observed. Nevertheless, these differences are smaller in this case. This can be explained by the fact that the flux flattens during the evolution (see section 4.1.1). The cross section homogenization, then, provides better results.

Concerning the micro depletion models, the concentration estimation is always affected by the 1 fission yield approximation. In the fissile region, Sb123 concentration difference is equal to -4.84%; Ho165 to -11.69%. Excluding the isotopes more sensitive to thermal fission production (discussed in 3.2.2), it is possible to see, in figure 4.12, that the difference is limited to 1.10% in MICRO SIGMA ZERO for Tc99. This is one of the most absorbing isotope (see figure 4.7).

In figure 4.12, it is also possible to notice that MICRO SIGMA ZERO concentrations are overestimated, in absolute value, with respect to MICRO SIGMA EVOLVING.

In the fertile region, concentration differences are higher, as it is possible to see in figure 4.13. In this case, MICRO SIGMA ZERO model tends to underestimate, in absolute value, the concentration difference with respect to MICRO SIGMA EVOLVING. The behaviour of these differences in the two models is not similar: while the absolute value of the concentration difference increases during the evolution for the fissile region, the fertile one shows a decrease. Concentrations are not correctly estimated at the initial steps. This is due to the fact that, while at time zero the fission product concentrations are initialized to zero, before solving the first time interval evolution, a trace of each isotope is assumed in order to avoid numerical instability. A concentration of the order of  $10^{+14} \frac{\text{nuclei}}{\text{cm}^3}$  is introduced. Because this number can differ in the core step and in the lattice one, a concentration difference can be observed in the initial step. Its relative importance is higher for those isotopes whose concentration is small. Tc99, for instance, presents a relative concentration difference after one day operation equal to 23% (absolute value at time zero:  $N_{Tc99}^{ref} = 6.88 \cdot 10^{+14} \frac{\text{nuclei}}{\text{cm}^3}$ ).

Table 4.3 Fissile-Fertile Cluster: Time 1440 Absorption Comparison: homogeneous MINARET at 33 groups/ heterogeneous reference TDT-MOC (in pcm)

NUCLEUS	FISSILE ASSEMBLY	FERTILE ASSEMBLY
U238	-5	+5
Pu239	-8	6
Pu241	-1	0

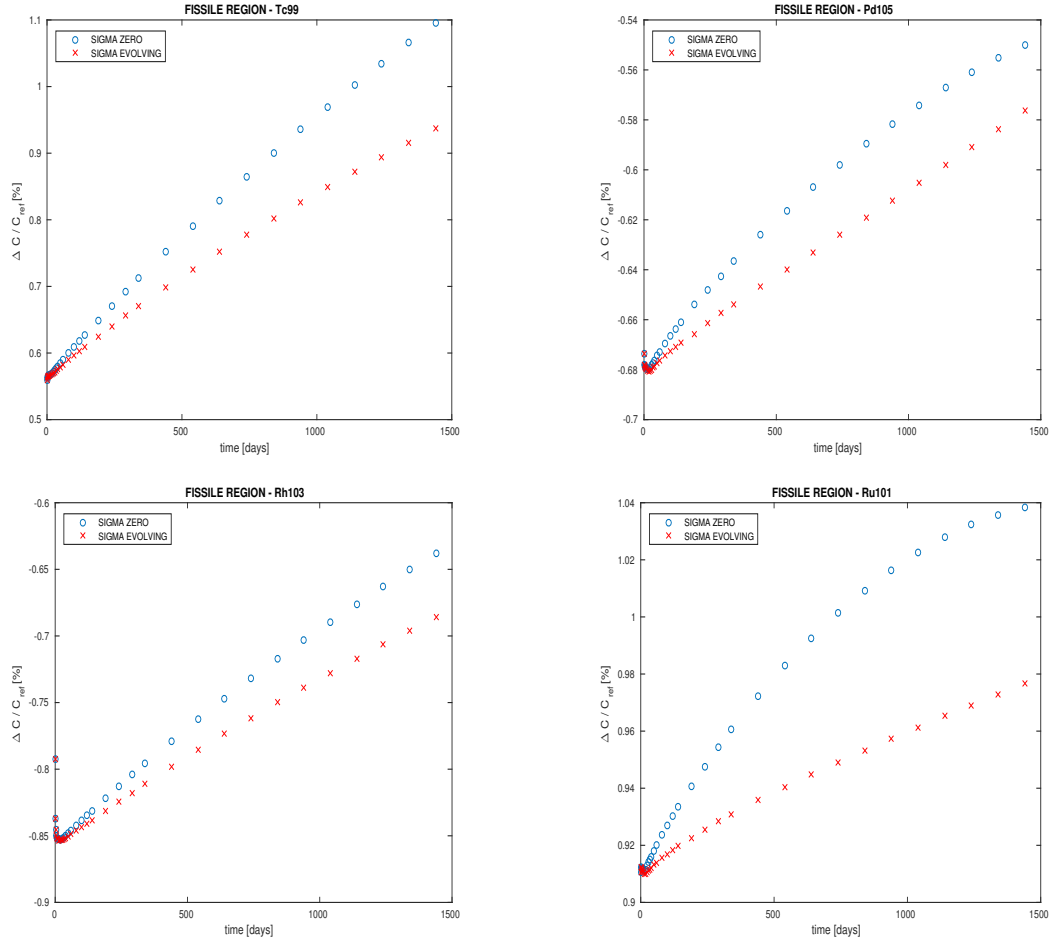


Figure 4.12 Fissile-Fertile Cluster: Relative difference of the fission product concentrations during the evolution in the fissile region

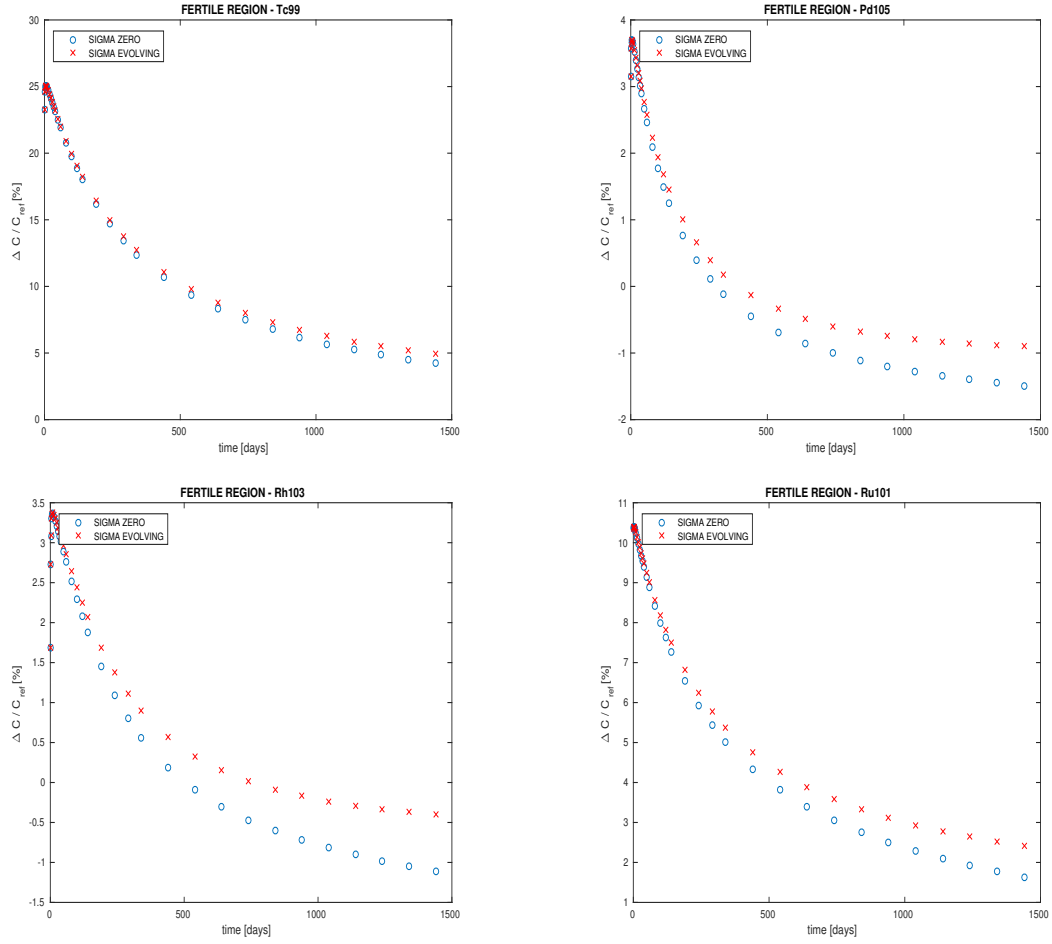


Figure 4.13 Fissile-Fertile Cluster: Relative difference of the fission product concentrations during the evolution in the fertile region

At the end of the calculation, the concentration difference for Tc99 is 4.93% for the MICRO SIGMA EVOLVING model and 4.22% for the MICRO SIGMA ZERO one (absolute value at 1440 days:  $N_{Tc99}^{ref} = 2.71 \cdot 10^{+19} \frac{nuclei}{cm^3}$ ).

Actinides are better estimated with the MICRO SIGMA EVOLVING model as well. At the end of the calculation, this model shows a concentration difference for Pu239 equal to -0.26% in the fertile region (see figure 4.14). The same isotope is evaluated with an error of -1.13% in the MICRO SIGMA ZERO model. For U238, the error is limited to +0.12% in the fertile region (+0.03% for MICRO SIGMA EVOLVING - see figure 4.15).

In table 4.4, it is possible to see the influence of these isotopes on the global reactivity. The decomposition has been made with the formula 3.7.

At the end of the calculation, the reactivity difference for the MICRO SIGMA ZERO model is equal to +46 pcm. The drift, the difference between the time 0 and time 1440 days  $k_{inf}$  is equal to +65 pcm. However, the drift is not monotonous and present a maximum of +100 pcm at 840 days.

For the MICRO SIGMA EVOLVING model, the reactivity difference at 1440 days is equal to +1 pcm, with a drift of +20 pcm. In this case the curve is monotonous and no peak is present.

In figure 4.16 and 4.17, the relative differences, normalized to the reference energy-integrated flux, between MOC reference and core depletion models are presented. In the fertile region, differences are higher. The MACRO and MICRO SIGMA EVOLVING depletion models behave in a similar way: they estimate an harder flux for the fertile and a softer one for the fissile. The difference in the fissile region is smaller than the one in the fertile. The SIGMA ZERO model tends to overestimate the flux around 1 keV and underestimate it around 1

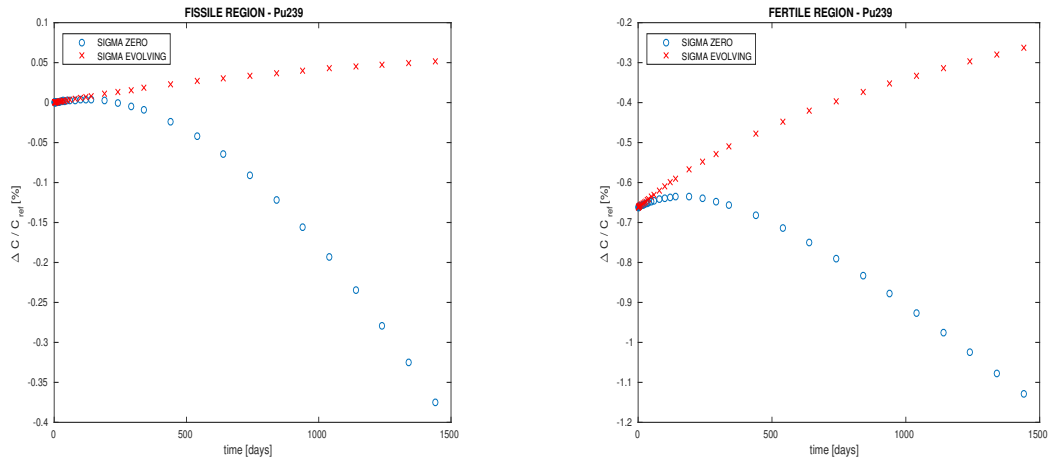


Figure 4.14 Fissile-Fertile Cluster: Relative difference of Pu239 concentration during the evolution



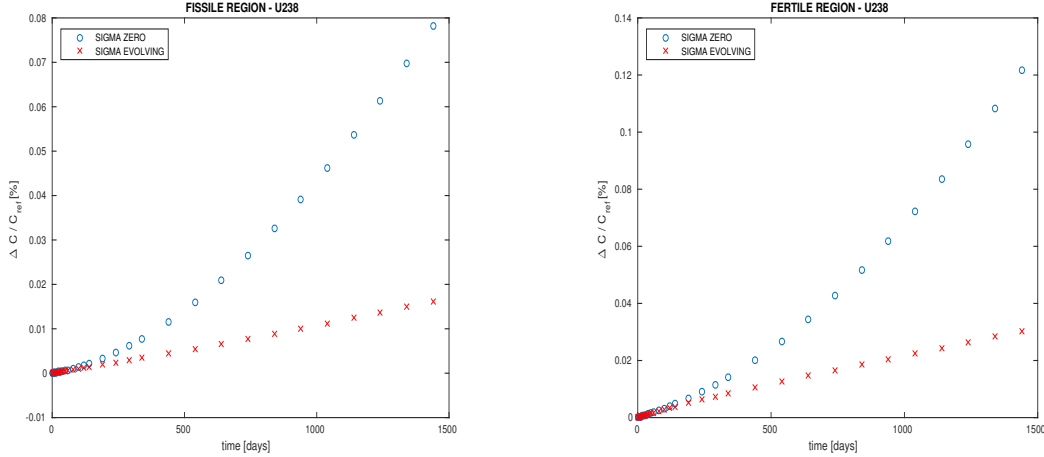


Figure 4.15 Fissile-Fertile Cluster: Relative difference of U238 concentration during the evolution

MeV.

Considering the reaction rates in table 4.4, the MICRO SIGMA EVOLVING model overestimates the importance of parasitic absorptions in the fissile region (a reactivity loss is observed) and underestimates it in the fertile (a reactivity gain is observed). This compensation, already discussed for the MACRO depletion model, is a little bit more important. The absolute difference of Pu239 is equal to +22 pcm, whereas it is limited to -8 pcm for the MACRO depletion.

This phenomenon is not observed in the MICRO SIGMA ZERO depletion model. Absorption reaction rate is considerably underestimated for U238 in both fissile and fertile regions. This gain in reactivity can be explained, as in the cell case, saying that the time zero cross sections are not adapted to follow the flux shifting.

In conclusion, comparing the three core evolution models for a fissile-fertile cluster geometry, a drift equal to +100 pcm (the same order of the one in the cell case) is observed with the MICRO SIGMA ZERO depletion model. This drift is equal to 1.3% of the reactivity loss and can be reduced to +20 pcm (0.26%) if evolving cross section libraries are used.

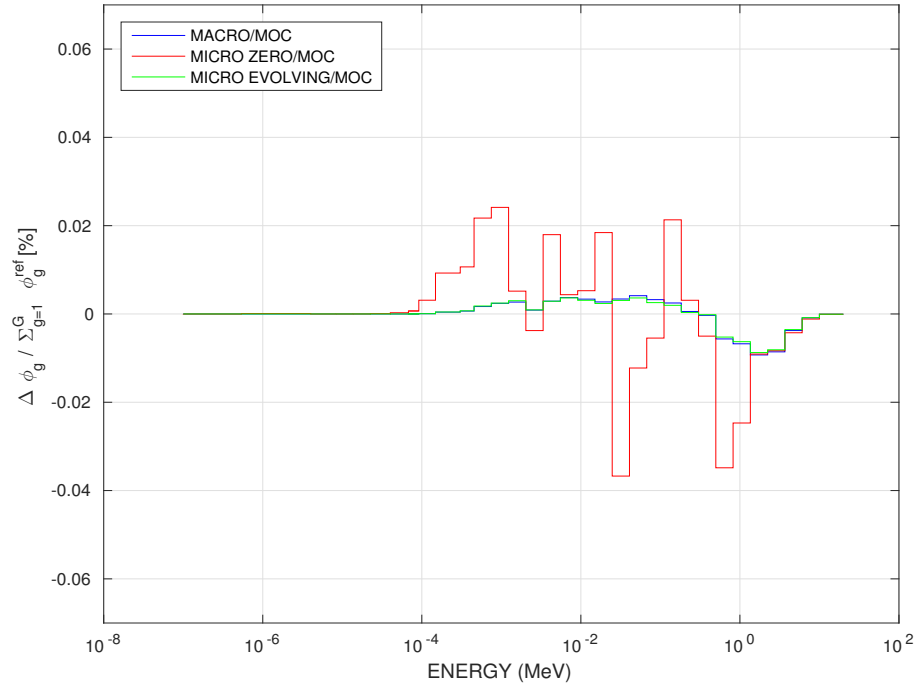


Figure 4.16 Fissile-Fertile Cluster: homogenized fissile flux comparison between MOC reference and core depletion models at 1440 days

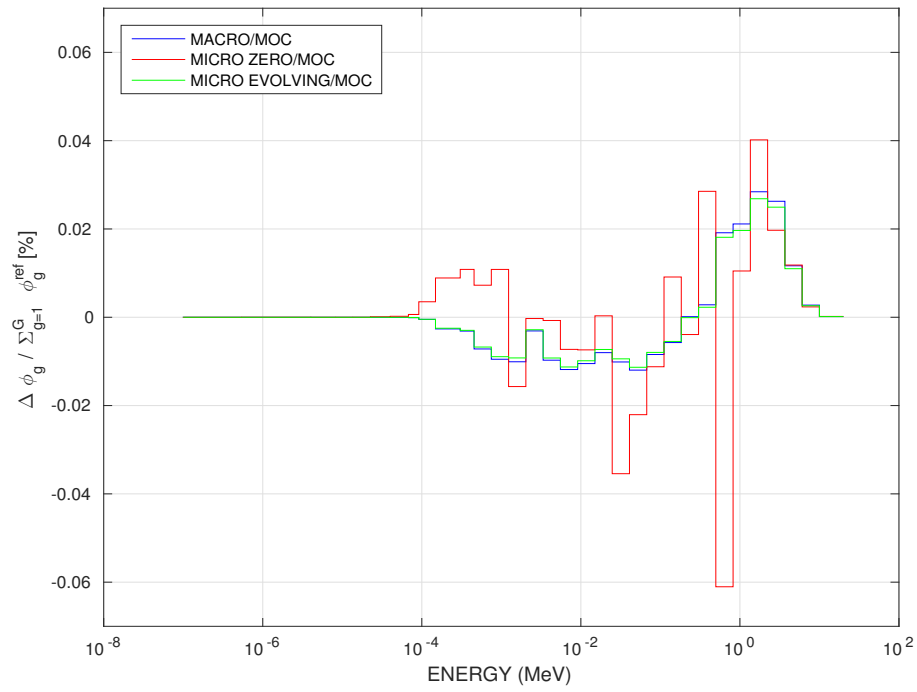


Figure 4.17 Fissile-Fertile Cluster: homogenized fertile flux comparison between MOC reference and core depletion models at 1440 days

Table 4.4 Fissile-Fertile Cluster: Absorption rate comparison at 1440 days

FISSILE REGION			
	MACRO [pcm]	MICRO SIGMA ZERO [pcm]	MICRO SIGMA EVOLVING [pcm]
U238	-5	+131	-8
Pu239	-8	-6	-19
Pu240	+1	-32	-4
Pu241	-1	-23	-4
Fe56	-1	+12	-1
Tc99	0	-9	-5
Ru101	0	-11	-6
Rh103	0	-2	+3
Pd105	0	-1	+3
FERTILE REGION			
	MACRO [pcm]	MICRO SIGMA ZERO [pcm]	MICRO SIGMA EVOLVING [pcm]
U238	+5	+94	+2
Pu239	+6	-3	+22
Pu240	0	-5	+3
Pu241	0	-2	+1
Fe56	+1	+5	+1
Tc99	0	-3	-3
Ru101	0	-2	-2
Rh103	0	0	0
Pd105	0	0	+1

### 4.2.2 Burn-up parametrization of the cross section libraries

In the previous chapter, a study on the effect of the burn-up tabulation points in the MICRO SIGMA EVOLVING model has been performed for a CFV cell geometry. Analogously, such a study will be performed for the fissile-fertile cluster geometry. The MICRO SIGMA EVOLVING model which uses the cross section libraries deriving from the reference calculations (34 burn-up tabulation points) is compared with the analogous model which uses the cross section libraries with only 2 burn-up tabulation points: one for the beginning and one for the end of the calculations. These libraries are created performing monostep lattice depletion with constant reaction rate integration scheme. Only one time interval covers the time span from 0 to 1440 days.

The results are shown in figure 4.18. The maximum difference between the 34 point SIGMA EVOLVING model and the 2 point one is equal to +4 pcm at 540 days. Otherwise, there's no significant difference between the two MICRO SIGMA EVOLVING models. This 2 point model, which reduces to 20 pcm the reactivity difference (in spite of 100 pcm for MICRO SIGMA ZERO), is accurate enough and it requires a reasonable amount of time to create the cross section libraries. The accuracy of the 2 point model underlines that the involved

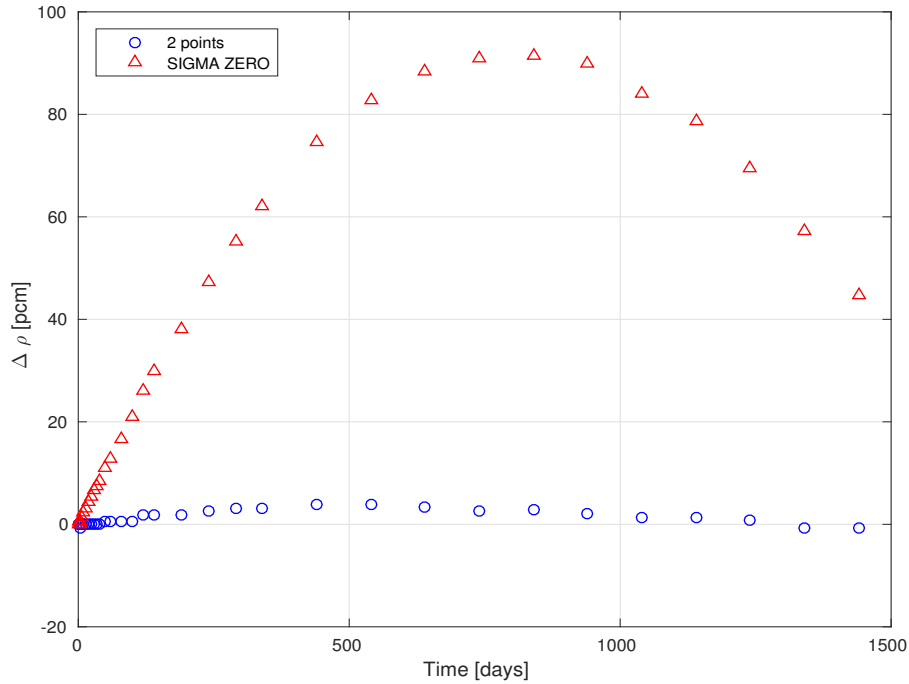


Figure 4.18 Fissile-Fertile Cluster:  $k_{inf}$  comparison between 34 point MICRO SIGMA EVOLVING and core evolution models with 2 burn-up tabulation points in the cross section libraries or only 1 (SIGMA ZERO)

phenomenon is mostly linear.

### 4.3 Conclusions

In this chapter, a fissile-fertile cluster geometry has been studied. One fertile assembly, charged with depleted UOX, is surrounded by 6 fissile assemblies, charged with MOX fuel. Each assembly is composed by elementary cells and it presents a proper flux distribution inside. This distribution, however, does not present great heterogeneities.

In the first section, it is shown that an evolution geometry, where only the external ring is distinguished, correctly represents the cluster during the evolution. This simplification of the evolution geometry, with respect to a cell-by-cell evolution, greatly reduces the calculation time.

In the second section, then, the depletion models have been compared on an assembly-homogenized geometry. No leakage model has been applied. The MICRO SIGMA ZERO model presents a drift equal to +100 pcm (1.3% of the overall reactivity loss), whereas the one of the MICRO SIGMA EVOLVING model is equal to +20 pcm (0.26%).

These results show the importance of a burn-up parametrization of the cross section libraries. The reference parametrization presents 34 tabulation points but, thanks to the great linearity of the phenomenon, only 2 burn-up tabulation points are required to correctly represent the cluster evolution.

Consequently, the 2 point MICRO SIGMA EVOLVING model is preferred to the MICRO SIGMA ZERO one, because an higher accuracy is reached only by doubling the calculation time and the memory storage.

## CHAPTER 5 EVOLUTION OF A 2D CORE PLANE GEOMETRY

The aim of this chapter is, first of all, to answer to the question: “How is the reactivity difference associated to the MICRO SIGMA ZERO model propagated throughout the core?” As it will be possible to explain later in this chapter, the numerical answer that will be given will be limited by certain assumptions: geometry used, boundary conditions and the absence of a leakage model, in lattice calculations, to condense the cross sections.

The second question this chapter would answer is: “Is it possible to simplify the calculation scheme adapting it to the currently used one?” The currently used calculation scheme will be briefly introduced in section 5.2, before validating its application during the evolution in section 5.4.

### 5.1 Geometry

A 2D geometry that aims to be representative of a CFV plane is now considered. The geometry in figure 5.1 is constituted by an hexagonal lattice: 13 rings, with reflective boundary conditions applied on the external one. As a consequence of this boundary conditions, a major hypothesis, which helps to simplify the calculations, is made: a perfect reflector is supposed to surround the core.

The hexagons represent homogenized assemblies, equal, concerning the geometry, to the ones observed in the previous chapter. Different kinds of assemblies are taken into account to simulate the different materials and the heterogeneities present in the CFV. In fact, two different fissile materials are used:

- C1 : MOX fuel with higher Plutonium weight fraction (21%)
- C2: MOX fuel with lower Plutonium weight fraction (7%)

A fertile material is also considered:

- FCAI : UOX fuel with depleted uranium (0.2%)

In figure 5.1, it is possible to observe the regions which occupies each materials:

- the 3 external rings contain FCAI.
- the following 3 rings contain C2. The outer ring, in contact with the fertile material, has been distinguished.

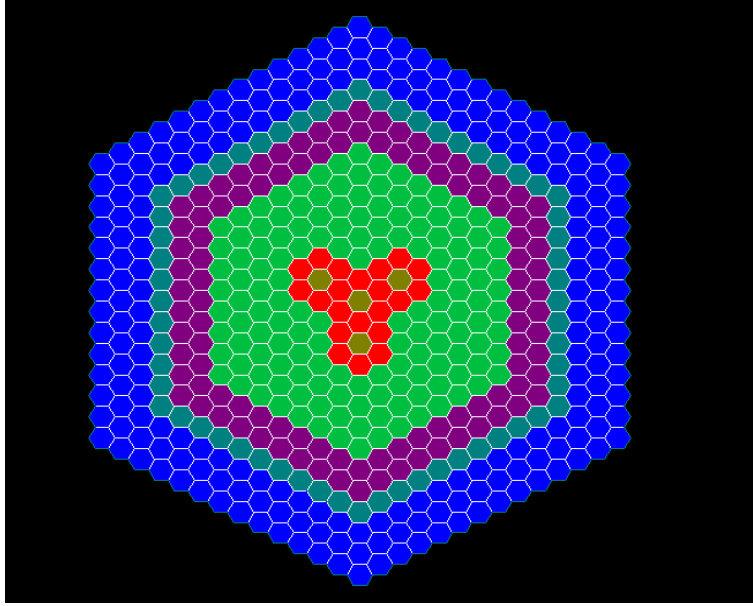


Figure 5.1 Core Plane Geometry

- the inner region contains C1.
- the central assembly and three of the second ring ( $30^\circ$ ,  $150^\circ$ ,  $270^\circ$ ) contain FCAI. The fissile region containing C1 in contact with these assemblies has been distinguished.

It is important to highlight the fact that this plane does not belong to the CFV design project (figure 1.3 and 1.4). This geometrical configuration has been designed for this particular application in order to have a simplified super-critical geometry. In fact, no CFV plane is super-critical. The third dimension, as already discussed in chapter 1, is of major importance to make the reactor critical and respect safety requirements. Consequently, neutron leakage is more important throughout the axial dimension than the radial one. This justifies the assumption of an external perfect reflector. The low neutron leakage throughout radial dimension justifies another major assumption: all lattice calculations used to condense the cross sections have been performed without applying a leakage model. This last assumption is related to a technical problem encountered by the author at the moment of the calculations: the leakage models coded in APOLLO3 had not been optimized yet to allow depletion calculations with a large number of isotopes in a reasonable time.

Once described the geometry and presented all the assumptions, it is time to describe the depletion geometry. Before this, however, the spatial mesh used to perform MINARET calculations is worth being illustrated. After a convergence analysis, it has been decided to divide each hexagon in 6. The reactivity difference with a case where 12 triangles have been

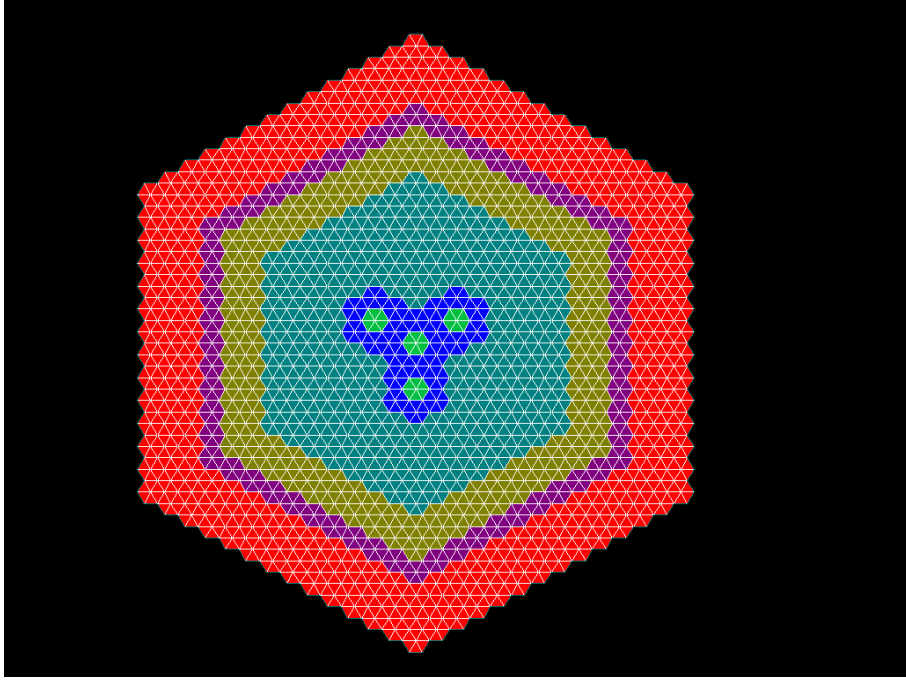


Figure 5.2 Spatial Mesh and Depletion geometry

used is limited to 0.4 pcm. This spatial mesh, depicted in figure 5.2, has also been used as depletion geometry. 547 hexagonal assemblies are presented with 3282 depletion regions.

## 5.2 Cross Sections

Before starting to present the results, few words must be written concerning the condensed cross sections used in these core calculations. In section 5.3, 6 materials will be used:

- FCAI\_C2 : contained in the outer fertile region.
- C2 : contained in the C2 fissile region in contact with the fertile one. Lattice calculations for energy condensation are similar to the ones presented in the chapter which deals with the fissile-fertile cluster.
- C2\_ABS: contained in the inner C2 fissile region. An infinite lattice of this kind of assembly alone has been considered for energy condensation.
- C1\_ABS: contained in the outer C1 fissile region. Lattice calculations analogous to C2\_ABS.
- C1: contained in the inner C1 fissile region. Lattice calculations analogous to C2.



- FCAI\_C1: contained in the central fertile region.

However, this 6 materials calculation scheme appears to be more refined than the industrial one used to simulate sodium reactors. The actual calculation scheme implies at lattice step:

- infinite lattice calculations for fissile materials (similar to the ones used to condense the cross sections for C1\_ABS and C2\_ABS).
- external source calculations for the fertile ones.

The external source is chosen in order to represent the energy integrated neutron flux obtained from the infinite lattice calculations. In the considered case, however, fertile materials have been evaluated, at lattice step, close to a fissile region in order to have a sustain flux. For the time being, in fact, APOLLO3 does not solve external source problems. Section 5.4 is the occasion to analyze the validity of such calculation scheme during the evolution. Consequently, 4 materials will be used:

- FCAI\_C2 : contained in the outer fertile region.
- C2\_ABS: contained in the C2 fissile region.
- C1\_ABS: contained in the C1 fissile region.
- FCAI\_C1: contained in the inner fertile region.

The results will be compared to the MICRO SIGMA EVOLVING model with 6 materials, that will be considered the reference calculation for the next sections.

### 5.3 Results: 6 Materials

The multiplication factor at time zero is equal to 1.40728 . The flux distribution is presented in figure 5.3. The outer C1 fissile region presents the flux peak, whereas the lowest value of the flux is, obviously, in the external ring of the lattice. The peak is 340 higher than the lowest value. A depression of the flux is present in the inner fertile region. The flux is normalized to a total power of 10 MW/cm and after 1440 days a reactivity loss equal to 6567 pcm is observed. The ratio between the flux peak and its lowest value is reduced to 197. It is possible to observe the flux distribution at the final time step in figure 5.4.

Of course, a change in isotope concentrations occurs. While the fertile regions gain reactivity due to the production of actinides, the fissile region loses reactivity due to the creation of

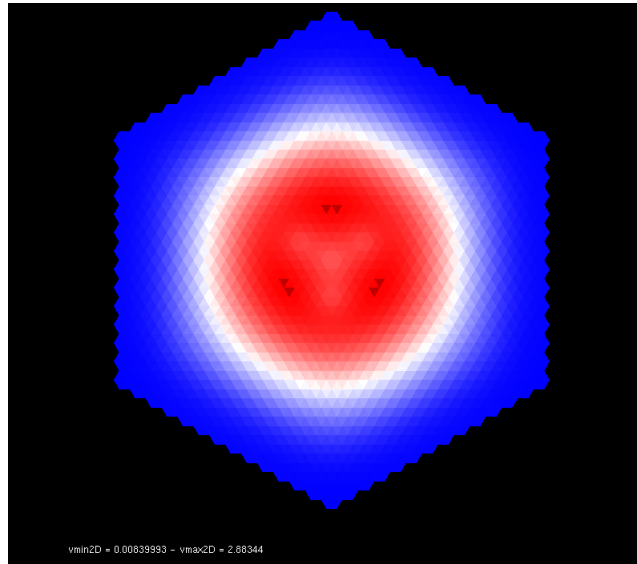


Figure 5.3 Intial time flux distribution

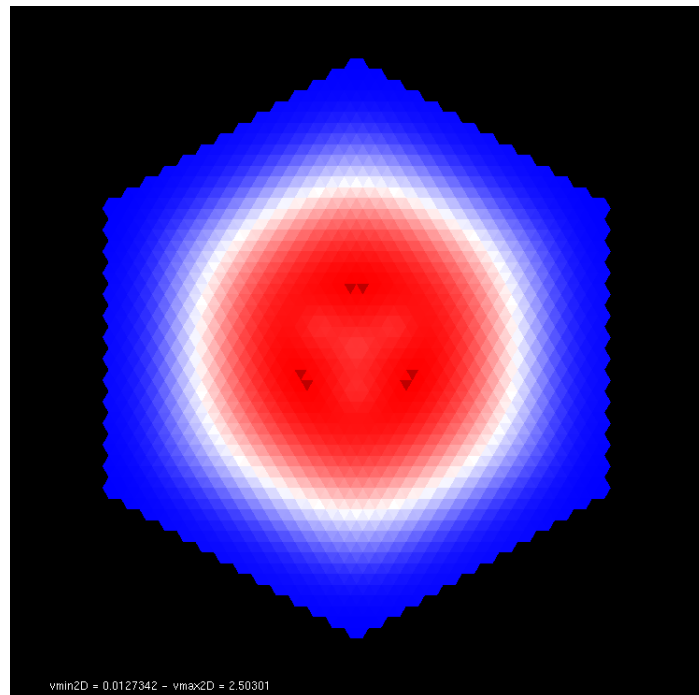


Figure 5.4 Flux distribution at 1440 days

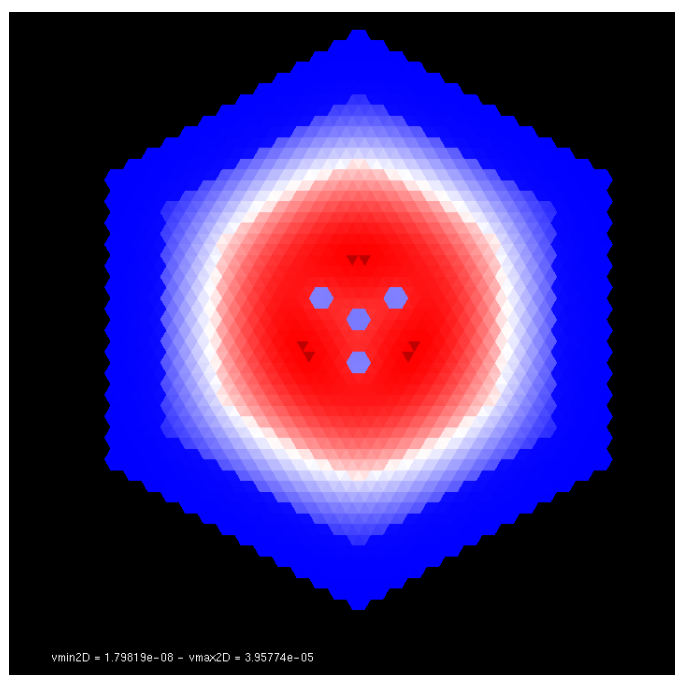


Figure 5.5 Tc99 concentration map at 1440 days

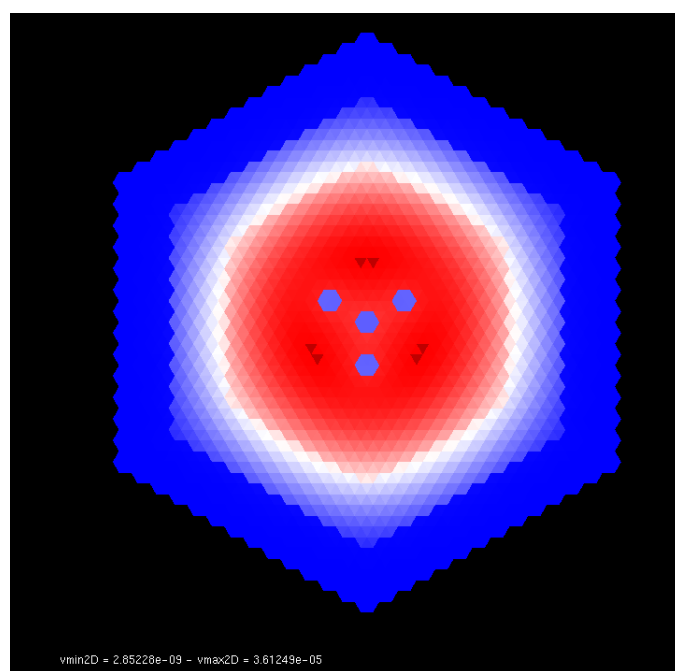


Figure 5.6 Pd105 concentration map at 1440 days

fission products and to the consumption of fissile materials. This creation follows the flux distribution as it is possible to see in figure 5.5 and 5.6 for Tc99 and Pd105.

At 1440 days, for Tc99, the ratio between the highest concentration and the lowest one is equal to 2201 and the average concentration of the inner fertile region is equal to 0.25 the maximum value. For Pd105, the ratio between the highest concentration value and the lowest one is equal to 12665 and the average concentration of the inner fertile region is equal to 0.20 the maximum value. In table 5.1 other analogous data are presented. The last line of this table shows that the three models are able to predict the flux distribution and its gradient after 1440 days. The macro depletion model, however, does not seem accurate to estimate the fission product distribution. Fission products are highly underestimated in the outer fertile region (-83.54% for Tc99). This shows that the macro depletion model is not capable to follow the core evolution. At the same time, it is possible to note that U235 and U238 are correctly interpolated (with a 3% maximum difference), revealing a major coding effort to optimize the interpolation rule that describes the variations of these two isotopes. This optimization seems to lack for the fission products and for the Pu239, which is underestimated in the outer fertile region by almost 90%. In the fertile external ring, fission products are underestimated, as well as Pu239 conversion. This leads to a flux distribution that is higher in the inner regions and lower in the outer ones, whose importance in the neutron balance is smaller. As a consequence, this particular flux distribution results in a less important reactivity loss (+516 pcm with respect to the reference case). Comparing the MACRO multiplication factor with the reference, the reactivity difference linearly increases (figure 5.7).

On the contrary, the MICRO SIGMA ZERO depletion model seems accurate to predict not only the flux distribution but also the concentrations. For the isotopes treated in table 5.1 the concentration difference does not exceed 0.3%. Observing the average concentration of

Table 5.1 6 Materials: Comparisons of isotope concentrations and flux at 1440 days

	Peak/Lowest Value Ratio			Peak/Inner Fertile Averaged Value		
	EVOLVING	ZERO	MACRO	EVOLVING	ZERO	MACRO
U238	1.405	1.405	1.406	1.071	1.071	1.071
U235	2.191	2.192	2.224	1.734	1.739	1.734
Pu239	225	225	2177	2.645	2.651	2.679
Pd105	12665	12699	16608	5.238	5.246	5.290
Tc99	2201	2207	13166	4.032	4.043	4.351
Ru101	4540	4553	3450	4.449	4.462	4.589
Rh103	8699	8722	157136	4.766	4.778	5.025
Flux	197	197	199	1.088	1.087	1.090

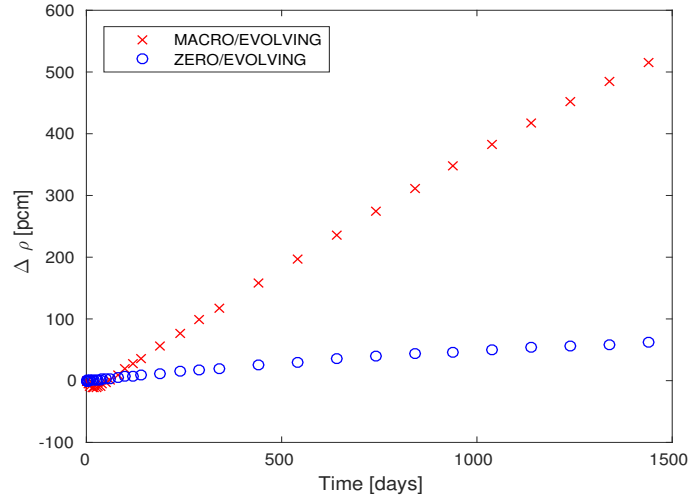


Figure 5.7 Comparison of the MACRO and MICRO SIGMA ZERO evolution calculation with respect to the MICRO SIGMA EVOLVING one.

all the isotopes in the 6 macro-regions containing the 6 materials used, it is possible to note a maximum difference of +3% for Pu241 in FCAI\_C1 and +2% for Nd142 in C1. These absolute concentration values, however, are small:  $4.30 \cdot 10^{17} \frac{\text{atoms}}{\text{cm}^3}$  for Nd142 and  $1.05 \cdot 10^{18} \frac{\text{atoms}}{\text{cm}^3}$  for Pu241. To sum up, the overall reactivity difference, at 1440 days, is equal to +61 pcm. Because no major concentration differences are observed, and the flux is correctly evaluated, this difference must be related to the fact that cross sections at time zero does not exactly estimate reaction rates when a flux shifting occurs. This is the phenomenon already observed for cell and fissile-fertile cluster geometry.

It is important to note here that this phenomenon, which introduces an error, does not propagate, or reach an higher value, in a core 2D geometry. The reactivity difference remains smaller than 1% of the overall reactivity loss.

### 5.3.1 Burn-up parametrization of the cross section libraries

It has been shown that a reactivity difference equal to +61 pcm arises if time zero cross section libraries are used. The reference calculation, in this case, is a MICRO SIGMA EVOLVING model which uses cross section libraries with 34 burn-up tabulation points. It is interesting to observe if this burn-up parametrization can be reduced, as already done in the cell and cluster geometry cases. Lattice calculations are performed in order to create 2 point cross section libraries. A time interval covering from 0 to 1440 days is used. A constant integration scheme for the reaction rates is applied in order to avoid negative values and the convergence

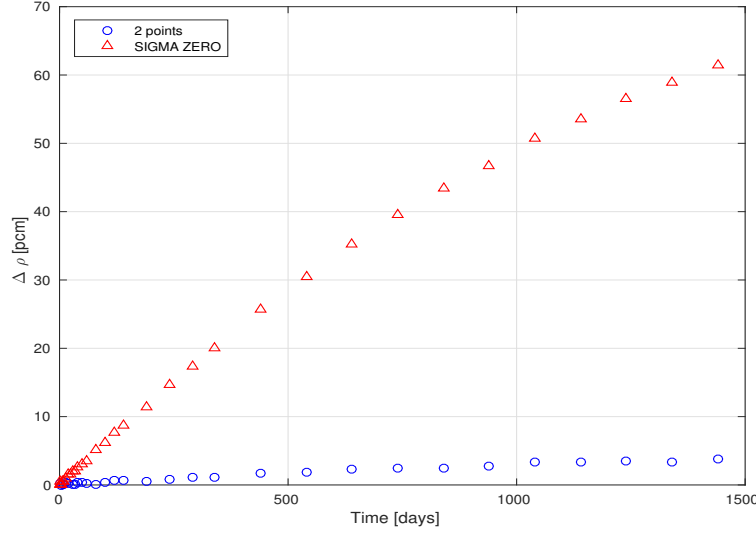


Figure 5.8 2D core plane  $k_{inf}$  comparison between 34 point MICRO SIGMA EVOLVING calculation and core evolution models with 2 burn-up tabulation points in the cross section libraries or only 1 (SIGMA ZERO)

test is not accomplished so that the time interval is not divided by 2.

The results are shown in figure 5.8. The difference between the 2 point model and the reference one is limited to +4 pcm at the end of the calculation. It is a remarkable result which justifies doubling the calculation time and memory storage.

#### 5.4 Results: 4 Materials

The multiplication factor at time zero is equal to 1.40694 and this value is 17 pcm smaller than the one presented in the previous section. It is obtained using the same condensed cross sections for the couple of materials C1 , C1\_ABS and C2 , C2\_ABS. These cross sections come from the condensation of an infinite fissile assembly lattice calculation. Whereas in the previous section the cross sections have been condensed for the fissile regions closer to the fertile ones accounting for the presence of the latter, in this section all the cross sections for the fissile regions are condensed without taking into account the nearby assemblies. This approximation, of course, introduces an error. In this case, this error is equal to 17 pcm and it is acceptable. But how does it change during the evolution? Does it increase? Does it diminish?

In figure 5.9, it is possible to observe that, applying the MICRO SIGMA EVOLVING depletion model (using cross section libraries with 34 burn-up points), this error diminishes. At 1440 days, it is equal to -11 pcm. This decrease is easily explained by the fact that,

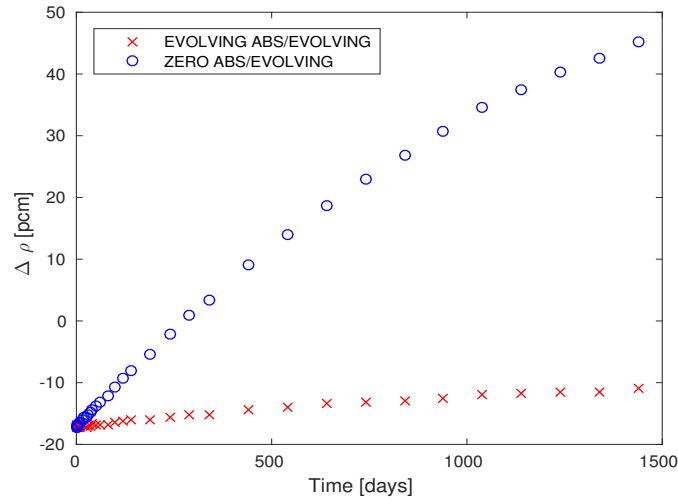


Figure 5.9 Comparison of the MICRO SIGMA ZERO and MICRO SIGMA EVOLVING calculation performed with 4 materials with respect to the MICRO SIGMA EVOLVING one performed with 6 materials.

during the evolution, the flux distribution tends to flatten, reducing the heterogeneities. If this occurs, the fissile assemblies are less influenced by the surrounding ones.

Concerning the MICRO SIGMA ZERO depletion model, at 1440 days, the reactivity difference is equal to +45 pcm. In figure 5.9, it is possible to observe the drift that the reactivity difference undergoes from the initial to final step: 62 pcm, almost the same value observed in the previous section. This shows that, even in this case, the same phenomenon presented before occurs. It also propagates in the same way throughout the 2D core geometry. At 290 days, a compensation occurs almost eliminating the reactivity difference.

In table 5.2, it is possible to see that no major error is introduced by the depletion models

Table 5.2 4 Materials: Comparisons of isotope concentrations and flux at 1440 days

	Peak/Lowest Value Ratio			Peak/Inner Fertile Averaged Value		
	EVOLVING	ZERO ABS	EVOLVING ABS	EVOLVING	ZERO ABS	EVOLVING ABS
U238	1.405	1.405	1.405	1.071	1.071	1.071
U235	2.191	2.192	2.190	1.734	1.735	1.731
Pu239	225	225	225	2.645	2.656	2.649
Pd105	12665	12698	12673	5.238	5.272	5.258
Tc99	2201	2206	2202	4.032	4.062	4.047
Ru101	4540	4552	4542	4.449	4.482	4.465
Rh103	8699	8721	8703	4.766	4.801	4.784

in the estimation of the concentration ratio. Focusing, now, on the average concentrations for the 6 macro-regions defined for the reference model, for the MICRO SIGMA ZERO the maximum concentration difference is -2.58% for Np237 in the inner fertile region (absolute value:  $1.68 \cdot 10^{18} \frac{\text{atoms}}{\text{cm}^3}$ ). It is possible to observe that this is 3 order of magnitude smaller than the one for the U238 concentration.

Concerning the MICRO SIGMA EVOLVING depletion model, the maximum concentration difference is observed, even in this case, in the inner fertile region: Pu241 presents a difference equal to -1.06% (absolute value:  $1.05 \cdot 10^{18} \frac{\text{atoms}}{\text{cm}^3}$ ).

## 5.5 Conclusions

In this chapter, a 2D core plane geometry has been investigated. Approximation and hypothesis have been introduced in order to have an idea of the behaviour of the MICRO SIGMA ZERO model in a core configuration.

In section 5.3, it has been shown that this model leads to a reactivity difference equal to +61 pcm. This value is coherent with the ones observed in the previous chapters. A correct parametrization of the burn-up tabulation points in the cross section libraries can reduce the difference to +4 pcm, only by doubling the calculation time with respect to the MICRO SIGMA ZERO model. This remarkable result justifies the use of burn-up parameterized cross section libraries in core calculations.

Another result that is worth discussing is the drift in the reactivity difference shown by the MACRO depletion model. This model is not accurate enough for core calculations where major heterogeneities are present.

In addition, in section 5.4, the importance of the surrounding materials in the fissile cross section condensation has been studied. Four cross section libraries have been used instead of six. Fissile assemblies have been considered in an infinite lattice and the presence of surrounding fertile materials have been neglected in the condensation. This leads to a maximum reactivity difference of -20 pcm for the 34 point MICRO SIGMA EVOLVING model. The drift of the MICRO SIGMA ZERO is equal to +62 pcm. This value is coherent with the one previously observed.

A study on the burn-up parametrization has not been performed in this case. It can be concluded, nevertheless, that the cross section condensation of the fissile materials is not strongly affected by the surrounding assemblies. This assumption can, theoretically, reduce the number of cross section libraries used in full core calculations, even if more representative 3D geometry must be investigated.



## CHAPTER 6 CONCLUSION

The aim of this project was the validation of a depletion model. This validation has been performed on three different 2D geometries: an elementary cell, a fissile-fertile cluster and a core plane.

The model to validate is the one usually used by the ECCO/ERANOS SFR calculation scheme. In this work, it has been called MICRO SIGMA ZERO. Core depletion calculations are performed using time zero microscopic cross sections. It has been shown that this model presents a reactivity difference that is of the order of 100 pcm if no leakage model is applied. The presence of leakage can double the difference, as shown for the elementary cell. However, the reactivity difference is maintained below 2% of the overall reactivity loss.

This model makes the assumption that microscopic cross sections do not vary during the evolution and fissile material change. This assumption is re-discussed in this occasion. This depletion model is, in fact, compared with two depletion models currently used in APOLLO2/CRONOS2 thermal reactor calculations: the macroscopic depletion model (here called MACRO) and the micro-depletion model which uses “evolving” microscopic cross section libraries (here called MICRO SIGMA EVOLVING). The former uses macroscopic cross section libraries which are burn-up parametrized. Bateman equations are not solved in core calculations and proper values of the cross sections are interpolated from the libraries. The latter uses microscopic cross section libraries which are burn-up parametrized as well. Bateman equations are solved in core calculations. This model is the more refined, because it is able to take into account flux distribution heterogeneities in more complex geometries, where the macro depletion model fails (see chapter 5). Unfortunately, the MICRO SIGMA EVOLVING model requires burn-up parametrized microscopic cross section libraries, that require lattice depletion calculation to be created and memory to be stored.

The reactivity difference observed in the MICRO SIGMA ZERO model is principally due to a flux shifting towards lower energy for the fissile materials and to higher energy for the fertile ones. This change modifies the weighting function used for the microscopic cross section condensation and introduces a time dependence for 33 energy group core calculations. Fortunately, this phenomenon has a minor impact and it can be linearly approximated. The MICRO SIGMA EVOLVING model, then, can be applied using microscopic cross section libraries parametrized in burn-up with only 2 tabulation points: one at the beginning and

one at the end of the calculation. Microscopic cross sections are linearly interpolated between the two points and the results do not differ more than a few pcm in comparison to the case where 34 points have been used to create the libraries.

In conclusion, the MICRO SIGMA ZERO model has not been validated. Instead, a MICRO SIGMA EVOLVING model with two burn-up tabulation points in the microscopic cross section libraries is preferred. An higher accuracy of the results is reached only by doubling the calculation time at lattice step and the memory storage. Of course, these conclusions are limited to the cases considered here. Future work must be done to validate the model in presence of leakage and for 3D geometries. A study of the whole CFV configuration is thus suggested.

## REFERENCES

- [1] J. E. Kelly. "Generation IV International Forum: A decade of progress through international cooperation". *Progress in Nuclear Energy*, vol. 77, pp. 240-246, 2014.
- [2] J. Lamarsh. *Introduction to Nuclear Reactor Theory*. American Nuclear Society, 2002.
- [3] Commissariat à l'énergie atomique et aux énergies alternatives. "Quatrième génération : vers un nucléaire durable", March 2010.
- [4] CEA Monographie DEN. *Les réacteurs nucléaires à caloporteur sodium*. Le Moniteur, 2014.
- [5] Commissariat à l'énergie atomique et aux énergies alternatives. "Les Réacteurs à Neutrons Rapides de 4e Génération à Caloporteur Sodium, le Démonstrateur Technologique ASTRID", December 2012.
- [6] F. Varaine, P. Marsault, M-S. Chenaud, A. Bernardin, B. Conti, P. Sciora, C. Venard, B. Fontaine, N. Devictor, and L. Martin. "Pre-conceptual design study of ASTRID core". In *ICAPP. Chicago, USA*, 2012.
- [7] C. De Saint Jean, B. Habert, O. Litaize, and C. Noguere, G. Suteau. "Status of CONRAD, a nuclear reaction analysis tool". In *International Conference on Nuclear Data for Science and Technology. Nice, France*, 2007.
- [8] M. Coste-Delclaux. "GALILEE : A nuclear data processing system for transport, depletion and shielding codes". In *Workshop On Nuclear Data Evaluation for Reactor applications. Saint-Paul-Lez-Durance, France*, 2009.
- [9] C.M. Diop, O. Petit, E. Dumonteil, F.X. Hugot, Y.K. Lee, A. Mazzolo, and J.C. Trama. "TRIPOLI-4: A 3D CONTINUOUS-ENERGY MONTE CARLO TRANSPORT CODE". In *PHYTRA1: First International Conference on Physics and Technology of Reactors and Applications. Marrakech, Morocco*, 2007.
- [10] J.M. Ruggieri, J. Tommasi, J.F. Lebrat, C. Suteau, D. Plisson-Rieunier, C. De Saint Jean, G. Rimpault, and J.C. Sublet. "ERANOS 2.1 : International Code System for GEN IV Fast Reactor Analysis". In *ICAPP. Reno, USA*, 2006.
- [11] A. Tsilanizara, C.M. Diop, B. Nimal, M. Detoc, L. Lunéville, M. Chiron, T.D. Huynh, I. Brésard, M. Eid, J.C. Klein, B. Roque, P. Marimbeau, C. Garzenne, Parize J.M., and

- C. Vergne. "DARWIN: An Evolution Code System for a Large Range of Applications". *Journal of Nuclear Science and Technology*, Supplement 1, pp. 845-849, 2000.
- [12] S. Lahaye, P. Bellier, H. Mao, and A. Tsilanizara. "First Verification and Validation Steps of MENDEL Release 1.0 Cycle Code System". In *PHYSOR. Kyoto, Japan*, 2014.
- [13] B. Roque, P. Archier, P. Bourdot, C. De-Saint-Jean, F. Gabriel, J.-M. Palau, V. Pascal, D. Schneider, G. Rimpault, and J.-F. Vidal. "APOLLO3: Roadmap for a new generation of simulation tools devoted to the neutronic core calculation of the ASTRID integrated technology demonstrator". In *Fast Reactors and Related Fuel Cycles: Safe Technologies and Sustainable Scenarios (FR13). Paris, France*, 2013.
- [14] H. Golfier, R. Lenain, C. Calvin, J.-J. Lautard, A.-M. Baudron, Ph. Fougeras, Ph Magat, E. Martinolli, and Y. Dutheillet. "APOLLO3: a common project of CEA, AREVA and EDF for the development of a new deterministic multi-purpose code for core physics analysis". In *International Conference on Mathematics, Computational Methods & Reactor Physics. Saratoga Springs, USA*, 2009.
- [15] Open Cascade. *Salome : The open source integration platform for numerical simulation*. <http://www.salome-platform.org>, 2005.
- [16] A. Hébert. *Applied Reactor Physics*. Presses Internationales Polytechnique, 2009.
- [17] R.J.J. Stammler and M. J. Abbate. *Methods of Steady-State Reactor Physics in Nuclear Design*. Academic Press Inc, 1983.
- [18] J.-F Vidal, G. Noguere, Y. Pénéliou, and A. Santamarina. "Qualification of JEFF3.1.1 library for high conversion reactor calculations using the ERASME/R experiment". In *PHYSOR. Knoxville, USA*, 2012.
- [19] J.-C. Sublet and P. Ribon. "A probability table based cross section processing system: CALENDF - 2001". *Journal of Nuclear Science and Technology*, Supplement 2, pp. 856-859, 2002.
- [20] CEA Monographie DEN. *La Neutronique*. Le Moniteur, 2013.
- [21] R. Sanchez, C. Hewko, and S. Santandrea. "Numerical Computation of Doppler-Broadening in the Resonance Domain". In *International Conference on Mathematics and Computational Methods Applied to Nuclear Science and Engineering (M & C). Sun Valley, USA*, 2013.

- [22] R. Sanchez. "A New Derivation of the Doppler-Broadened Kernel for Elastic Scattering and Application to Upscattering Analysis in the Resonance Region of U238". In *Joint International Conference on Mathematics and Computation (M & C), Supercomputing in Nuclear Applications (SNA) and the Monte Carlo (MC) Method. Nashville, USA*, 2015.
- [23] C. Mounier and B. Normand. "Fission Source Calculations and its Influence in Criticality Applications". In *International Conference on the Physics of Reactors "Nuclear Power: A Sustainable Resource". Interlaken, Switzerland*, 2008.
- [24] P. Mosca, C. Mounier, P. Bellier, and I. Zmijarevic. "Improvements in Transport Calculations by the Optimized Multigroup Libraries for Fast Neutron Systems". In *PHYSOR. Knoxville, USA*, 2012.
- [25] G. Rimpault, M.-J. Grimstone, and J.-D. Tullet. "Accurate Treatments of Fast Reactor Fuel Assembly Heterogeneity in the ECCO Cell Code". In *PHYSOR. Marseille, France*, 1990.
- [26] F. Simon. "Validation de la Méthode SPM pour l'Autoprotection des Résonances". Master's thesis, Polytechnique de Montréal, 2011.
- [27] T. Tone. "A Numerical Study of Heterogeneity Effects in Fast Reactor Critical Assemblies". *Journal of Nuclear Science and Technology*, vol. 12[8], pp. 467-481, 1975.
- [28] R. Roy. "Reactor Core Methods". In *Nuclear Computational Science: A Century in Review*, 1st ed., Azmy, Y. and Sartori, E., Ed. Netherlands: Springer, 2010, pp. 167-215.
- [29] D. Schneider, F. Dolci, F. Gabriel, J.-M. Palau, M. Guillo, B. Pothet, P. Archier, K. Ammar, F. Auffret, R. Baron, A.-M. Baudron, P. Bellier, L. Bourhrara, L. Buiron, M. Coste-Delclaux, C. De Saint Jean, J.-M. Do, B. Espinosa, E. Jamelot, V. Jouault, J.-J. Lautard, R. Lenain, J.-C. Le Pallec, L. Lei Mao, E. Masiello, S. Mengelle, F. Moreau, P. Mosca, M. Muniglia, N. Odry, V. Pascal, S. Pastoris, B. Roque, A. Targa, C. Patricot, S. Santandrea, D. Sciannandrone, A. Tsilanizara, J.-F. Vidal, and I. Zmijarevic. "APOLLO3: CEA/DEN Deterministic Multi-purpose Code for Reactor Physics Analysis". In *PHYSOR. Sun Valley, USA*, 2016.
- [30] R. Le Tellier. *Développement de la Méthode des Caractéristiques pour le Calcul de Réseau*. PhD thesis, Polytechnique de Montréal, 2006.
- [31] S. Santandrea and R. Sanchez. "Acceleration techniques for the characteristic method in unstructured meshes". *Annals of Nuclear Energy*, vol. 29, pp. 323-352, 2002.

- [32] S. Santandrea. "An Integral Multidomain DPN Operator as Acceleration Tool for the Method of Characteristics in Unstructured Meshes". *Nuclear Science and Engineering*, vol. 155, pp. 223-235, 2007.
- [33] J.-Y. Moller and J.-J. Lautard. "MINARET, a Deterministic Neutron Transport Solver for Nuclear Core Calculations". In *International Conference on Mathematics and Computational Methods Applied to Nuclear Science and Engineering (M & C)*. Rio de Janeiro, Brazil, 2011.
- [34] A.-M. Baudron and J.-J. Lautard. "Simplified Pn Transport Core Calculations in the APOLLO3 SYSTEM". In *International Conference on Mathematics and Computational Methods Applied to Nuclear Science and Engineering (M & C)*. Rio de Janeiro, Brazil, 2011.
- [35] N. Odry, J.-F. Vidal, and G. Rimpault. "A domain decomposition method in APOLLO3 solver, MINARET". In *Joint International Conference on Mathematics and Computation (M & C), Supercomputing in Nuclear Applications (SNA) and the Monte Carlo (MC) Method*. Nashville, USA, 2015.
- [36] B. Faure. "Simulation des fuites neutroniques à l'aide d'un modèle B1 hétérogène pour des réacteurs à neutrons rapides et à eau légère". Master's thesis, Polytechnique de Montréal, 2016.
- [37] J. Spanier. "Monte Carlo Methods". In *Nuclear Computational Science: A Century in Review*, 1st ed., Azmy, Y. and Sartori, E., Ed. Netherlands: Springer, 2010, pp. 117-165.
- [38] P. Archier, S. Domanico, J.-M. Palau, and G. Truchet. "Validation of a Multi-Purpose Depletion Chain for Burnup Calculations through TRIPOLI-4 CALCULATIONS and IFP Perturbation Method". In *PHYSOR*. Sun Valley, USA, 2016.
- [39] W. H. Press, B. P. Flannery, S. A. Teukolsky, and W. T. Vetterling. *Numerical Recipes in FORTRAN*. Cambridge University Press, 1992.
- [40] E. Brun, E. Dumonteil, and F. Malvagi. "Systematic Uncertainty Due to Statistics in Monte Carlo Burnup Codes: Application to a Simple Benchmark with TRIPOLI-4-D". *Progress in Nuclear Science and Technology*, vol. 2, pp. 879-885, 2011.
- [41] S. Berche. "Validation de schémas de calcul APOLLO3 pour assemblages de type RNR". Master's thesis, Polytechnique de Montréal, 2015.

- [42] G. Rimpault, J.-F. Vidal, and W.F.G. Van Rooijen. "Neutron Leakage Treatment in Reactor Physics: Consequences for Predicting Core Characteristics". In *PHYSOR. Kyoto, Japan*, 2014.
- [43] J.-F. Vidal, P. Archier, B. Faure, V. Jouault, J.-M. Palau, V. Pascal, G. Rimpault, F. Auffret, L. Graziano, E. Masiello, and S. Santandrea. "APOLLO3 Homogenization Techniques for Transport Core Calculations - Application to ASTRID CFV Core". In *International Conference on Mathematics and Computational Methods Applied to Nuclear Science and Engineering (M & C). Jeju, Korea*, 2017.

## APPENDIX A Rim Effect

Time zero calculation of a CFV cell (figure 3.1) is performed subdividing the fuel zone in 4 regions. Fuel regions are numbered so that the external is the number 1 and the internal the number 4. The percentage of the surface of fuel zone covered by each region is 10%, 10%, 30% and 50% for region 1 to 4. This is the actual fuel zone subdivision used to perform self-shielding calculations in thermal reactors. Region-averaged fluxes  $\phi_r$  are compared with the cell-averaged flux  $\bar{\phi}$ , using the following formula:

$$\hat{\phi}_r = \frac{\phi_r - \bar{\phi}}{\bar{\phi}} \quad (\text{A.1})$$

In table A.1, it is possible to see that the flux distribution is flat. However, because the flux integrated over the whole energy region is considered, this does not mean that subdividing the fuel zone in 4 regions does not affect the neutron balance. Flux gradients, in fact, can be relevant in those energy regions where resonances are present. But this is not the case. In table A.2, it is possible to observe the behaviour of the flux  $\phi_r^g$  integrated over the energy region 1.2-2 keV. This region is representative, because it contains an important resonance of the U238. The relative differences  $\hat{\phi}_r^g$  are shown in the table. It is possible to observe that the gradient is limited.

Table A.1 Relative differences in integrated flux distribution at time zero

ZONE	REGION	$\hat{\phi}_r \cdot 10^4$
SODIUM	-	+1.09
CLADDING	-	+0.17
VOID	-	-2.3
FUEL	1	-0.16
	2	+0.08
	3	+0.12
	4	-0.90



Table A.2 Relative differences in flux distribution in the energy group 1.2-2 keV at time zero

ZONE	REGION	$\hat{\phi}_r^g$
SODIUM	-	+1.26%
CLADDING	-	+0.66%
VOID	-	+0.35%
FUEL	1	+0.01%
	2	-0.24%
	3	-0.65%
	4	-1.40%

## APPENDIX B Homogeneous $B_1$ Leakage Model

In order to account for a finite dimension of the lattice grid that contains the reference geometry the fundamental mode approximation is assumed:

$$\phi^g(\vec{r}, \vec{\Omega}) = \varphi^g(\vec{r}, \vec{\Omega}) e^{i\vec{B} \cdot \vec{r}} \quad (\text{B.1})$$

The flux  $\phi^g$  is decomposed into two terms: the fundamental flux  $\varphi^g(\vec{r}, \vec{\Omega})$ , which represents the flux distribution inside the reference geometry composing the grid, and the macroscopic distribution  $e^{i\vec{B} \cdot \vec{r}}$ . This distribution contains the buckling, which is a real number, and it is defined as  $B^2 = \vec{B} \cdot \vec{B}$ . The buckling adjusts the curvature of the flux distribution  $\varphi^g(\vec{r}, \vec{\Omega})$  throughout the lattice grid so that  $k_{eff} = 1$ .

The transport equation to solve becomes:

$$(\vec{\Omega} \cdot \vec{\nabla} + \Sigma^g(\vec{r}) + i\vec{\Omega} \cdot \vec{B}) \varphi^g(\vec{r}, \vec{\Omega}) = Q^g(\vec{r}, \vec{\Omega}) \quad (\text{B.2})$$

The leakage model that will be presented is called homogeneous  $B_1$ , because the buckling term  $B^2$  is introduced and equation B.2 is solved on an homogeneous geometry with an order  $L = 1$  of the Legendre polynomial expansion (linearly anisotropic scattering source).

Supposing only one fissile isotope and one secondary neutron fission spectrum to simplify the notation, for an homogeneous geometry (a geometry where  $\vec{r}$  dependency is lost), equation B.2 becomes:

$$(\Sigma^g + i\vec{\Omega} \cdot \vec{B}) \varphi^g(\vec{\Omega}) = \frac{1}{4\pi} \sum_{g'} \hat{\Sigma}_0^{g' \rightarrow g} \varphi^{g'} + \frac{3}{4\pi} \sum_{g'} \Sigma_{s,1}^{g' \rightarrow g} \vec{j}^{g'} \cdot \vec{\Omega} \quad (\text{B.3})$$

where the homogeneous current  $\vec{j}^g$  is defined as

$$\vec{j}^g = \int_{4\pi} d^2\Omega \varphi^g(\vec{\Omega}) \vec{\Omega} \quad (\text{B.4})$$

and

$$\hat{\Sigma}_0^{g' \rightarrow g} = \Sigma_{s,0}^{g' \rightarrow g} + \frac{\chi^g}{k_{eff}} \nu \Sigma_f^{g'} \quad (\text{B.5})$$

The leakage model is composed of two equations. The first is obtained by integrating B.3 over  $4\pi$ , while the second is obtained by multiplying equation B.3 by a weight function  $w(\vec{\Omega}) = (\Sigma^g + i\vec{B} \cdot \vec{\Omega})^{-1}$  before integrating it over  $4\pi$ . The weight function aims to eliminate the directional dependence of the homogeneous current  $\vec{j}^g$ .

The first equation becomes:

$$\Sigma^g \varphi^g + i \vec{j}^g \cdot \vec{B} = \sum_{g'} \hat{\Sigma}_0^{g' \rightarrow g} \varphi^{g'} \quad (\text{B.6})$$

while the second:

$$\varphi^g = \alpha[B, \Sigma^g] \sum_{g'} \hat{\Sigma}_0^{g' \rightarrow g} \varphi^{g'} - 3i \sum_{g'} \Sigma_{s,1}^{g' \rightarrow g} \vec{j}^{g'} \cdot \bar{\bar{\beta}}[B, \Sigma^g] \cdot \vec{B} \quad (\text{B.7})$$

where  $\alpha[B, \Sigma^g]$  is defined as

$$\alpha[B, \Sigma^g] = \begin{cases} \frac{1}{B} \tan^{-1} \left( \frac{B}{\Sigma^g} \right) & \text{if } B^2 > 0 \\ \frac{1}{\Sigma^g} - \frac{B^2}{3(\Sigma^g)^3} + \frac{B^4}{5(\Sigma^g)^5} - \frac{B^6}{7(\Sigma^g)^7} + \dots & \text{if } B^2 \cong 0 \\ \frac{1}{2\text{Im}\{B\}} \ln \left( \frac{\Sigma^g + \text{Im}\{B\}}{\Sigma^g - \text{Im}\{B\}} \right) & \text{if } B^2 < 0 \end{cases} \quad (\text{B.8})$$

and

$$\bar{\bar{\beta}}[B, \Sigma^g] = \frac{1}{B^2} (1 - \alpha[B, \Sigma^g] \Sigma^g) \bar{\bar{I}} \quad (\text{B.9})$$

$\bar{\bar{I}}$  is the identity matrix and  $\text{Im}\{B\}$  is the imaginary component of B in the case a subcritical medium is considered.

The directional dependence of the homogeneous current is removed introducing:

$$j^g = \frac{\vec{j}^g \cdot \vec{B}}{B} \quad (\text{B.10})$$

The leakage coefficient is then defined as:

$$D_B^g = \frac{i}{B} \frac{j^g}{\varphi^g} \quad (\text{B.11})$$

Introducing the quantities previously defined, the new set of  $B_1$  equations becomes:

$$\begin{cases} [\Sigma^g + D_B^g B^2] \varphi^g = \sum_{g'} \hat{\Sigma}_0^{g' \rightarrow g} \varphi^{g'} \\ D_B^g = \frac{1}{3\gamma[B, \Sigma^g]} \left[ 1 + 3 \sum_{g'} \Sigma_{s,1}^{g' \rightarrow g} D_B^{g'} \frac{\varphi^{g'}}{\varphi^g} \right] \end{cases} \quad (\text{B.12})$$

with

$$\gamma[B, \Sigma^g] = \frac{B^2}{3\Sigma^g} \frac{\alpha[B, \Sigma^g]}{(1 - \alpha[B, \Sigma^g] \Sigma^g)} \quad (\text{B.13})$$

The leakage rate  $L^g$  is naturally defined as:

$$L^g = D_B^g B^2 \varphi^g \quad (\text{B.14})$$

This term is then added to the heterogeneous transport equation:

$$\left( \vec{\Omega} \cdot \vec{\nabla} + \Sigma^g(\vec{r}) + D_B^g B^2 \right) \varphi^g(\vec{r}, \vec{\Omega}) = Q^g(\vec{r}, \vec{\Omega}) \quad (\text{B.15})$$

To sum up, when the critical buckling is searched (i.e.  $B_1$  is adjusted so that  $k_{eff} = 1$ ), the homogeneous  $B_1$  leakage model works in this way:

1. A first transport calculation in heterogeneous geometry and without leakage is performed in order to evaluate a flux distribution that will be used to homogenize the quantities of interest  $(\varphi^g, \Sigma^g, \dots)$
2. The set of  $B_1$  equations (B.12) is solved imposing  $k_{eff} = 1$  to find the leakage rate  $L^g$
3.  $L^g$  is considered in equation B.15. A new flux distribution and a new multiplication factor are evaluated.
4. If  $k_{eff} \neq 1$ , the new flux distribution is used for the homogenization of the quantities of interest and the procedure restarts from point 2.

Concerning the solution of the equation B.15, the leakage term is treated in three different ways:

- $D_B^g B^2$  is added to the macroscopic total cross section  $\Sigma^g$
- $D_B^g B^2$  is subtracted from the within-group scattering cross section  $\Sigma_{s,0}^{g \rightarrow g}$
- $Q^g(\vec{r}, \vec{\Omega})$  is multiplied by a non-leakage probability

$$P_{NL}^g = 1 - \frac{D_B^g B^2}{\Sigma^g + D_B^g B^2} \quad (\text{B.16})$$

Currently, the homogeneous  $B_1$  leakage model is extensively used to account for leakage, even if the homogenization procedure eliminates the heterogeneities inside the geometry. An overall leakage term is evaluated and no preferential leakage direction is considered. These assumptions seem reasonable for PWR in nominal conditions but, if a loss of coolant accident (LOCA) or a SFR are considered, streaming effects occur in the regions where the moderator is absent or where the sodium is present. These effects require an heterogeneous

representation of the leakage.

In this work, heterogeneous leakage and streaming effect have not been considered. If it is necessary to consider them, the heterogeneous  $B_1$  leakage model can be applied. If simplifying approximations are made, the streaming effect can be considered isotropic [25]. However, in APOLLO3, anisotropic streaming effects can be modelled since the TDT-MOC solver implements a rigorous technique to solve the transport equation in fundamental mode approximation and in the case of geometries with central symmetry [42]. The angular flux evaluated with this technique has been proved a satisfying weighting function for the partial, total and transfer cross section condensation [43].

# APPENDIX C    CFV Cell Infinite Multiplication Factor

TRIPOLI4			APOLLO3				ECCO	
Time [days]			1 SPECTRUM		4 SPECTRA			
	$k_{inf}^{T4}$	$\sigma$	$k_{inf}^{AP3/1}$	$\Delta\rho$ [pcm]	$k_{inf}^{AP3/4}$	$\Delta\rho$ [pcm]	$k_{inf}^{ECCO}$	$\Delta\rho$ [pcm]
0	1.54648	29	1.54580	-28	1.54678	12	1.54643	-2
1	1.54584	26	1.54540	-19	1.54637	22	1.54603	8
2	1.54611	29	1.54505	-44	1.54602	-4	1.54568	-18
3	1.54500	28	1.54474	-11	1.54572	30	1.54537	15
5	1.54507	29	1.54421	-36	1.54519	5	1.54484	-9
7	1.54417	29	1.54375	-18	1.54473	23	1.54438	9
10	1.54358	29	1.54313	-19	1.54411	22	1.54376	8
15	1.54308	30	1.54217	-38	1.54315	3	1.54280	-12
20	1.54153	29	1.54124	-12	1.54222	29	1.54186	14
25	1.54126	29	1.54031	-40	1.54129	1	1.54093	-14
30	1.53992	27	1.53938	-22	1.54036	19	1.54000	4
35	1.53892	28	1.53846	-20	1.53943	22	1.53907	6
40	1.53817	26	1.53753	-27	1.53851	14	1.53814	-1
50	1.53652	29	1.53568	-36	1.53665	6	1.53628	-10
60	1.53437	29	1.53383	-23	1.53480	18	1.53442	2
80	1.53051	26	1.53014	-16	1.53111	26	1.53072	9
100	1.52705	27	1.52646	-25	1.52743	16	1.52703	-1
120	1.52356	29	1.52280	-33	1.52377	9	1.52336	-9
140	1.51984	28	1.51915	-30	1.52012	12	1.51970	-6
190	1.51077	28	1.51010	-29	1.51106	13	1.51063	-6
240	1.50137	26	1.50114	-10	1.50210	33	1.50166	13
290	1.49299	27	1.49228	-32	1.49324	11	1.49279	-9
340	1.48429	26	1.48352	-35	1.48449	9	1.48402	-12
440	1.46692	25	1.46633	-28	1.46728	17	1.46685	-3
540	1.45061	25	1.44954	-51	1.45049	-6	1.45007	-26
640	1.43386	26	1.43316	-34	1.43410	12	1.43370	-8
740	1.41762	25	1.41719	-21	1.41812	25	1.41772	5
840	1.40245	25	1.40161	-42	1.40254	5	1.40214	-16
940	1.38753	25	1.38643	-57	1.38734	-10	1.38694	-31
1040	1.37203	25	1.37162	-22	1.37253	27	1.37212	5
1140	1.35814	26	1.35719	-51	1.35808	-3	1.35767	-25
1240	1.34389	22	1.34312	-43	1.34400	6	1.34357	-17
1340	1.33014	22	1.32939	-42	1.33027	7	1.32982	-18
1440	1.31741	25	1.31600	-81	1.31687	-31	1.31641	-58

# APPENDIX D CFV Cell Isotope Concentrations

TRIPOLI4			APOLLO3				ECCO	
			1 SPECTRUM		4 SPECTRA			
	$C_{1440}^{T4}$	$\sigma$	$C_{1440}^{AP3/1}$	[%]	$C_{1440}^{AP3/4}$	[%]	$C_{1440}^{ECCO}$	[%]
ACTINIDES								
U238	1.44E-002	0.05%	1.44E-002	0.02%	1.44E-02	0.02%	1.44E-002	0.02%
PU240	1.34E-003	0.10%	1.34E-003	-0.10%	1.34E-03	-0.12%	1.34E-003	-0.16%
PU239	2.30E-003	0.10%	2.30E-003	0.00%	2.30E-03	0.00%	2.30E-003	-0.06%
AM243	4.70E-005	0.37%	4.72E-005	0.34%	4.71E-05	0.25%	4.72E-005	0.29%
AM241	6.66E-005	0.11%	6.66E-005	0.05%	6.66E-05	0.09%	6.64E-005	-0.21%
PU242	3.54E-004	0.07%	3.54E-004	-0.13%	3.54E-04	-0.14%	3.54E-004	-0.18%
CM244	1.22E-005	0.79%	1.24E-005	1.91%	1.24E-05	1.72%	1.22E-005	0.12%
NP237	8.36E-006	3.92%	8.20E-006	-1.91%	8.46E-06	1.14%	8.19E-006	-2.10%
AM242M	3.21E-006	0.23%	3.17E-006	-1.11%	3.17E-06	-1.14%	3.68E-006	14.86%
NP239	3.83E-006	0.96%	3.85E-006	0.66%	3.85E-06	0.56%	3.82E-006	-0.13%
CM242	5.22E-006	0.43%	5.22E-006	-0.01%	5.22E-06	-0.07%	5.13E-006	-1.63%
CM245	1.02E-006	1.17%	1.04E-006	1.73%	1.03E-06	1.45%	1.02E-006	-0.05%
U234	2.89E-006	0.22%	2.88E-006	-0.11%	2.89E-06	-0.06%	2.88E-006	-0.17%
U236	4.34E-006	0.28%	4.34E-006	-0.01%	4.33E-06	-0.08%	4.34E-006	-0.03%
CM243	4.01E-007	0.69%	4.01E-007	-0.03%	4.00E-07	-0.18%	3.94E-007	-1.75%
U235	1.39E-005	0.36%	1.39E-005	0.12%	1.39E-05	0.19%	1.39E-005	0.11%
PU238	8.98E-005	0.17%	8.97E-005	-0.20%	8.97E-05	-0.11%	8.94E-005	-0.46%
PU241	2.33E-004	0.17%	2.33E-004	-0.04%	2.33E-04	-0.05%	2.33E-004	-0.03%
FISSION PRODUCTS								
PD105	1.21E-004	0.31%	1.21E-004	-0.06%	1.21E-04	-0.06%	1.21E-004	-0.26%
RU101	1.52E-004	0.32%	1.51E-004	-0.07%	1.51E-04	-0.06%	1.52E-004	0.43%
RH103	1.47E-004	0.33%	1.46E-004	-0.11%	1.46E-04	-0.11%	1.46E-004	-0.35%
TC99	1.32E-004	0.32%	1.32E-004	-0.08%	1.32E-04	-0.06%	1.32E-004	-0.52%
PD107	7.39E-005	0.30%	7.38E-005	-0.08%	7.38E-05	-0.09%	7.39E-005	0.03%
CS133	1.66E-004	0.33%	1.66E-004	-0.12%	1.66E-04	-0.11%	1.66E-004	-0.01%
SM149	2.65E-005	0.33%	2.65E-005	-0.17%	2.65E-05	-0.13%	2.66E-005	0.15%
MO97	1.24E-004	0.33%	1.24E-004	-0.09%	1.24E-04	-0.07%	1.24E-004	-0.22%
SM151	1.39E-005	0.32%	1.39E-005	-0.03%	1.39E-05	0.01%	1.39E-005	0.42%
ND145	7.62E-005	0.33%	7.61E-005	-0.13%	7.61E-05	-0.11%	7.63E-005	0.08%
CS135	1.85E-004	0.34%	1.85E-004	-0.12%	1.85E-04	-0.12%	1.85E-004	0.10%
MO95	1.02E-004	0.36%	1.02E-004	-0.10%	1.02E-04	-0.08%	1.02E-004	-0.26%

TRIPOLI4			APOLLO3				ECCO	
			1 SPECTRUM		4 SPECTRA			
	$C_{1440}^{T4}$	$\sigma$	$C_{1440}^{AP3/1}$	[%]	$C_{1440}^{AP3/4}$	[%]	$C_{1440}^{ECCO}$	[%]
ACTINIDES								
PM147	2.91E-005	0.21%	2.91E-005	-0.01%	2.91E-05	0.02%	2.91E-005	-0.18%
RU102	1.83E-004	0.37%	1.83E-004	-0.09%	1.83E-04	-0.10%	1.84E-004	0.47%
ND143	1.07E-004	0.34%	1.07E-004	-0.07%	1.07E-04	-0.06%	1.07E-004	-0.10%
AG109	3.38E-005	0.32%	3.38E-005	-0.04%	3.38E-05	-0.07%	3.36E-005	-0.53%
RU104	1.63E-004	0.34%	1.63E-004	-0.10%	1.63E-04	-0.11%	1.64E-004	0.45%
XE131	8.87E-005	0.34%	8.86E-005	-0.08%	8.86E-05	-0.08%	9.36E-005	5.53%
EU153	8.32E-006	0.31%	8.30E-006	-0.26%	8.30E-06	-0.24%	8.34E-006	0.24%
SM147	1.58E-005	0.51%	1.58E-005	-0.10%	1.58E-05	-0.06%	1.58E-005	-0.03%
PD106	8.86E-005	0.52%	8.86E-005	-0.07%	8.86E-05	-0.10%	8.89E-005	0.28%
MO100	1.66E-004	0.34%	1.66E-004	-0.11%	1.66E-04	-0.10%	1.66E-004	-0.08%
MO98	1.47E-004	0.36%	1.47E-004	-0.10%	1.47E-04	-0.09%	1.46E-004	-0.21%
PR141	1.24E-004	0.35%	1.24E-004	-0.11%	1.24E-04	-0.10%	1.23E-004	-0.25%
PD108	6.75E-005	0.42%	6.75E-005	-0.03%	6.74E-05	-0.08%	6.73E-005	-0.20%
ZR93	1.01E-004	0.34%	1.01E-004	-0.14%	1.01E-04	-0.12%	1.03E-004	1.76%
I129	3.13E-005	0.33%	3.12E-005	-0.09%	3.12E-05	-0.11%	3.12E-005	-0.09%
XE132	1.31E-004	0.35%	1.31E-004	-0.09%	1.31E-04	-0.10%	1.31E-004	0.02%
SM152	2.21E-005	0.43%	2.20E-005	-0.13%	2.20E-05	-0.15%	2.21E-005	-0.01%
XE134	1.89E-004	0.34%	1.89E-004	-0.09%	1.89E-04	-0.09%	1.90E-004	0.41%
CD111	9.71E-006	0.32%	9.70E-006	-0.04%	9.70E-06	-0.07%	9.88E-006	1.82%
ND146	7.40E-005	0.37%	7.39E-005	-0.09%	7.39E-05	-0.08%	7.41E-005	0.10%
EU154	2.37E-006	0.65%	2.37E-006	0.27%	2.37E-06	0.21%	2.37E-006	0.14%
ND148	4.53E-005	0.34%	4.52E-005	-0.12%	4.52E-05	-0.10%	4.54E-005	0.17%
I127	1.02E-005	0.32%	1.02E-005	-0.04%	1.02E-05	-0.06%	1.12E-005	9.76%
CE142	1.26E-004	0.34%	1.26E-004	-0.10%	1.26E-04	-0.09%	1.26E-004	-0.18%
ND144	7.48E-005	0.46%	7.47E-005	-0.16%	7.47E-05	-0.15%	7.46E-005	-0.25%
EU155	3.68E-006	0.39%	3.68E-006	-0.03%	3.67E-06	-0.06%	3.69E-006	0.49%
ZR91	6.77E-005	0.35%	6.76E-005	-0.12%	6.76E-05	-0.09%	6.78E-005	0.26%
LA139	1.45E-004	0.35%	1.45E-004	-0.10%	1.45E-04	-0.10%	1.45E-004	-0.32%
CS134	8.40E-006	0.81%	8.42E-006	0.24%	8.41E-06	0.15%	8.41E-006	0.12%
CS137	1.55E-004	0.33%	1.55E-004	-0.09%	1.55E-04	-0.09%	1.55E-004	0.31%
ND150	2.66E-005	0.34%	2.66E-005	-0.10%	2.66E-05	-0.08%	2.67E-005	0.23%
ZR92	8.09E-005	0.35%	8.08E-005	-0.12%	8.08E-05	-0.10%	8.10E-005	0.12%



TRIPOLI4			APOLLO3				ECCO	
			1 SPECTRUM		4 SPECTRA			
	$C_{1440}^{T4}$	$\sigma$	$C_{1440}^{AP3/1}$	[%]	$C_{1440}^{AP3/4}$	[%]	$C_{1440}^{ECCO}$	[%]
SM150	9.12E-006	0.86%	9.13E-006	0.07%	9.12E-06	0.01%	9.10E-006	-0.22%
GD157	2.17E-006	0.36%	2.17E-006	0.00%	2.17E-06	-0.01%	2.19E-006	0.62%
RU106	3.73E-005	0.10%	3.73E-005	-0.07%	3.73E-05	-0.09%	3.69E-005	-1.04%
RU103	6.86E-006	0.11%	6.87E-006	0.06%	6.87E-06	0.05%	6.85E-006	-0.21%
ZR94	1.09E-004	0.35%	1.09E-004	-0.08%	1.09E-04	-0.07%	1.07E-004	-1.64%
RU100	1.56E-005	0.76%	1.56E-005	-0.01%	1.56E-05	-0.09%	1.55E-005	-0.64%
PD104	1.63E-005	0.82%	1.63E-005	0.08%	1.63E-05	-0.01%	1.62E-005	-0.49%
SM148	8.13E-006	0.81%	8.12E-006	-0.17%	8.11E-06	-0.23%	8.09E-006	-0.44%
RB85	1.21E-005	0.35%	1.21E-005	-0.07%	1.21E-05	-0.04%	1.26E-005	4.04%
ZR96	1.27E-004	0.35%	1.27E-004	-0.11%	1.27E-04	-0.10%	1.27E-004	-0.04%
CE140	1.40E-004	0.35%	1.39E-004	-0.09%	1.39E-04	-0.08%	1.39E-004	-0.07%
GD155	8.39E-007	0.56%	8.38E-007	-0.17%	8.38E-07	-0.15%	8.27E-007	-1.44%
GD156	3.93E-006	0.47%	3.92E-006	-0.12%	3.92E-06	-0.14%	3.94E-006	0.21%
KR83	7.39E-006	0.33%	7.38E-006	-0.09%	7.38E-06	-0.09%	7.44E-006	0.74%
PD110	1.88E-005	0.34%	1.88E-005	-0.06%	1.88E-05	-0.10%	1.90E-005	1.34%
CD113	3.28E-006	0.36%	3.28E-006	-0.05%	3.28E-06	-0.07%	3.36E-006	2.39%
SM154	6.86E-006	0.34%	6.86E-006	-0.05%	6.86E-06	-0.05%	6.85E-006	-0.15%
NB95	4.17E-006	0.07%	4.17E-006	-0.10%	4.17E-06	-0.10%	4.16E-006	-0.40%
CD112	5.76E-006	0.42%	5.75E-006	-0.04%	5.75E-06	-0.09%	5.86E-006	1.82%
CE144	2.67E-005	0.08%	2.66E-005	-0.10%	2.66E-05	-0.09%	2.66E-005	-0.31%
BR81	2.85E-006	0.33%	2.85E-006	-0.08%	2.85E-06	-0.08%	3.00E-006	5.28%
TE130	6.70E-005	0.35%	6.70E-005	-0.08%	6.70E-05	-0.10%	6.71E-005	0.17%
CE141	4.22E-006	0.09%	4.23E-006	0.08%	4.23E-06	0.09%	4.22E-006	-0.06%
IN115	1.61E-006	0.33%	1.60E-006	-0.05%	1.60E-06	-0.06%	1.82E-006	13.28%
TB159	6.25E-007	0.32%	6.24E-007	-0.06%	6.24E-07	-0.07%	6.16E-007	-1.37%
CD110	4.38E-006	0.77%	4.38E-006	-0.13%	4.37E-06	-0.26%	4.33E-006	-1.14%
Y89	4.71E-005	0.35%	4.70E-005	-0.13%	4.70E-05	-0.09%	4.73E-005	0.51%
BA134	3.89E-006	1.00%	3.90E-006	0.19%	3.89E-06	0.11%	3.90E-006	0.20%
BA138	1.53E-004	0.35%	1.53E-004	-0.09%	1.53E-04	-0.09%	1.53E-004	-0.24%
SR90	5.14E-005	0.33%	5.13E-005	-0.12%	5.13E-05	-0.09%	5.15E-005	0.29%

## APPENDIX E Flux Spectrum Shifting

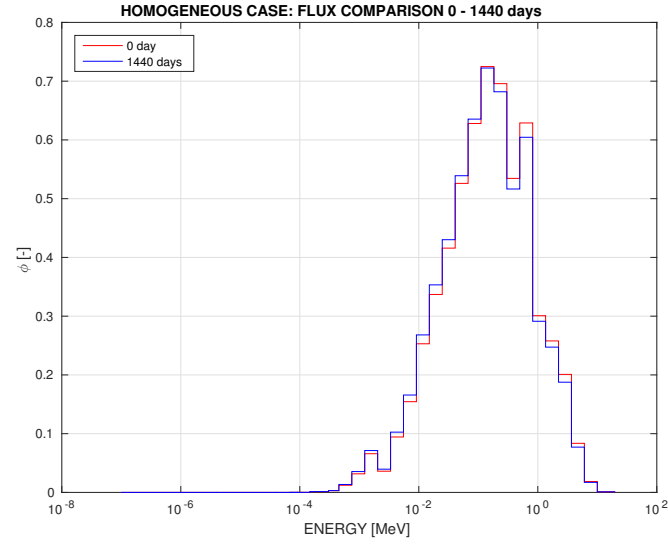


Figure E.1 Homogenised lattice flux spectrum comparison between BOC and EOC

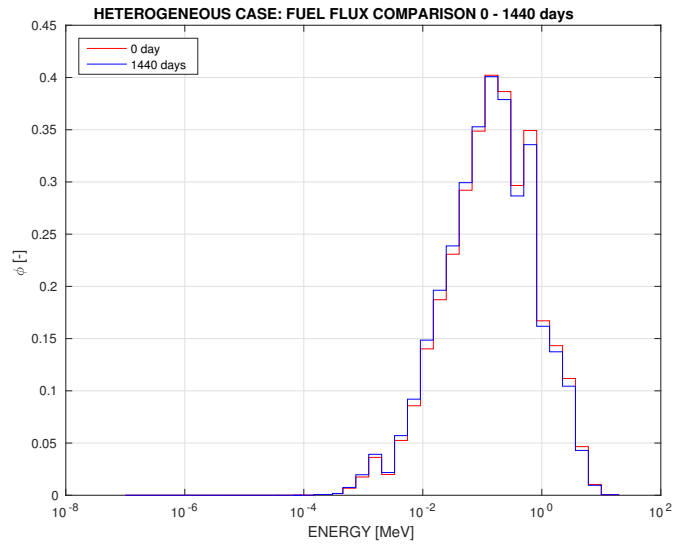


Figure E.2 Fuel lattice flux spectrum comparison between BOC and EOC

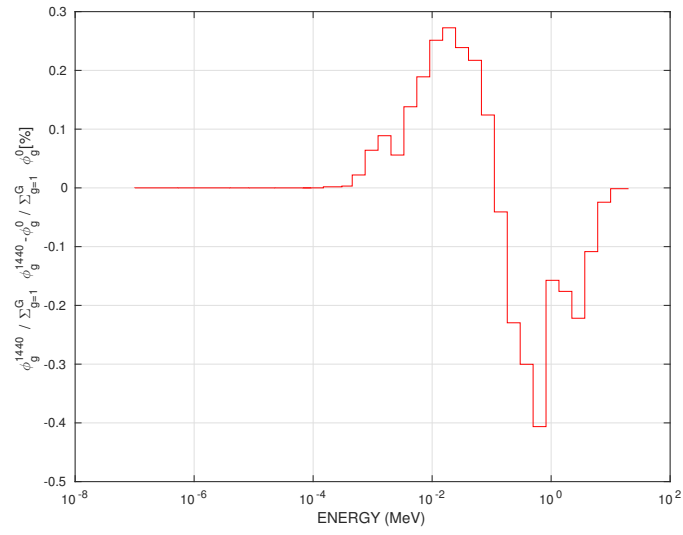


Figure E.3 Relative flux difference between BOC and EOC

# APPENDIX F    33 group energy mesh

Energy Mesh [MeV]		
19.6403	-	1.00E+001
1.00E+001	-	6.07E+000
6.07E+000	-	3.68E+000
3.68E+000	-	2.23E+000
2.23E+000	-	1.35E+000
1.35E+000	-	8.21E-001
8.21E-001	-	4.98E-001
4.98E-001	-	3.02E-001
3.02E-001	-	1.83E-001
1.83E-001	-	1.11E-001
1.11E-001	-	6.74E-002
6.74E-002	-	4.09E-002
4.09E-002	-	2.48E-002
2.48E-002	-	1.50E-002
1.50E-002	-	9.12E-003
9.12E-003	-	5.53E-003
5.53E-003	-	3.35E-003
3.35E-003	-	2.03E-003
2.03E-003	-	1.23E-003
1.23E-003	-	7.49E-004
7.49E-004	-	4.54E-004
4.54E-004	-	3.04E-004
3.04E-004	-	1.49E-004
1.49E-004	-	9.17E-005
9.17E-005	-	6.79E-005
6.79E-005	-	4.02E-005
4.02E-005	-	2.26E-005
2.26E-005	-	1.37E-005
1.37E-005	-	8.32E-006
8.32E-006	-	4.00E-006
4.00E-006	-	5.40E-007
5.40E-007	-	1.00E-007
1.00E-007	-	1.00E-011